11

Monte Carlo Simulation of SEM and SAM Images

Y.G. Li, S.F. Mao and Z.J. Ding
Hefei National Laboratory for Physical Sciences at Microscale and Department of Physics, University of Science and Technology of China, Hefei, Anhui 230026, P. R. China

1. Introduction

Monte Carlo method and its applications to electron microscopic and spectroscopic techniques

1.1 Electron microscopic and spectroscopic techniques

The electron microscopic and spectroscopic techniques are conveniently and widely used for surface and bulk analysis of materials. These analysis tools use the various types of electron signals that emitted from the specimen irradiated by a beam of mono-energetic primary electrons or X-rays for imaging of surface, and for structural and chemical characterization. Different signals in relevant techniques are secondary electrons (SEs) and backscattered electrons (BSEs) for scanning electron microscopy (SEM), Auger electrons (AEs) for Auger electron spectroscopy (AES) and scanning Auger microscopy (SAM), photoelectrons for X-ray photoelectron spectroscopy (XPS) and X-ray photo-emission electron microscopy (XPEEM), elastic scattered electrons for elastic peak electron spectroscopy (EPES), inelastic scattered electrons for electron energy loss spectroscopy (EELS) and reflection electron energy loss spectroscopy (REELS), characteristic X-ray and bremsstrahlung for electron probe microanalysis (EPMA) and analytical electron microscopy (AEM) (Reimer, 1998).

Particularly, SEM is more frequently used for a quick sample characterization. Imaging of microstructure of materials with SEs and BSEs plays a very important role in many scientific and technological fields. SE images, formed by SEs of very low energies (<50 eV) emitted from the surface region, provide mainly topographic information of the specimen surface with nanometer resolution with a modern SEM. BSE images can provide more information about the matrix composition for the signal electrons are transported from the sample interior within interaction volume of primary electrons of several keV energy. SAM is a technique that combines AES with SEM and is commercially available as an ultra-high vacuum instrument for chemical investigation of clean surfaces. With SAM it is possible to observe the surface elemental distribution and to obtain chemical state information by detecting AEs that carry characteristic energies representing the specific energy levels of surface atoms ionized by an incident electron beam.

The principle of these techniques relies on electron-solid interaction. Therefore, the study of electron transport is very important to these techniques for a detailed understanding of a

variety of physical processes involved in the electron–solid interaction. These physical processes comprise elastic and inelastic scattering in bulk and at surface. Such processes can occur repeatedly (multiple scattering), so that a combination of scattering effects that are responsible for some important features is observed in experimental spectra or images.

1.2 Monte Carlo method

The Monte Carlo (MC) method was initiated in the 1940s by Ulam and von Neumann who were working on Manhatten project in Los Alamos; they considered to design a novel numerical method with the use of random numbers to solve the problem of neutron tranposrt (Metropolis, 1987). Nowadays, MC methods are widely used in many fields to solve complex physical and mathematical problems (James, 1980; Rubinstein, 1981; Kalos & Whitlock, 1986), particularly those involving multiple independent variables where other numerical methods would demand formidable amounts of memory and computing time.

MC electron trajectory simulation method has been used since 1950's to electron probe microanalysis, electron spectroscopy and electron microscopy, for obtaining quantitative information on different signals recorded by these instruments. Various MC physical models have been proposed and used for specific purposes. The main advantages of MC simulation are the easy implementation of different scattering channels with their cross sections into a simulation model and the ability to describe radiation transport through material structures with complex geometry boundaries.

In a MC simulation of electron transport, an electron trajectory is tracked as a random sequence of flights that end with a scattering event where the electron changes its direction of movement and/or loses energy, and produces secondary signals in an inelastic event. For a given experimental condition numerical random trajectory histories of electrons have to be simulated to present statistically meaningful calculation result. To such a simulation a MC physical model is essential, which considers how to treat electron scattering with corresponding formulation, e.g. a set of differential cross sections (DCS), for the relevant interaction mechanism. The DCSs determine the probability distribution functions (PDF) of the random variables that represent physical quantities for tracing an electron track, e.g. free path between successive events, type of interaction taking place, energy loss and/or angular deflection in a particular scattering event. Once these PDFs are known, random sampling can be made so that a trajectory history is formed. When a large number of trajectory histories are generated, quantitative information on the signal transport process may be obtained by a statistical averaging over the simulated histories (Salvat et al., 2006).

A MC simulation yields the similar information as the solution of Boltzmann transport equation, with the same interaction model, but is easier to be implemented (Berger, 1963). In particular, the MC simulation of radiation transport in a sample with complex geometry is straightforward, while even the simplest finite geometries are very difficult to be dealt by transport equation method. The drawback of the MC method lies in its random nature, that is, the calculation results suffers statistical uncertainties, which can be reduced at the expense of increasing sampling population, and, hence, the computation time.

1.3 Physical processes

The present status of the MC calculation, particularly related to SEM/SAM, is outlined. For the treatment of electron elastic scattering, both the screened Rutherford formula and the Mott differential cross section have been available. Since it was been found (Ichimura & Shimizu,

1981; Reimer & Krefting, 1976) that the use of the Mott cross section is more satisfactory than the Rutherford cross section, particularly for heavier elements and at lower energies, the employment of the Mott cross sections in the keV and sub-keV energy region is now popular.
Regarding the approach to electron inelastic scattering, the Bethe stopping power equation in the continuous slowing-down approximation (CSDA) has been widely used with considerable success. To include fast secondary electron generation, some modifications have also been made to the CSDA: the hybrid of the CSDA with the individual energy loss processes due to inner-shell ionization (Ichimura & Shimizu, 1981), the utilization of the discrete inelastic scattering cross section of Moller (Moller, 1931; Murata et al., 1981), and the use of generalized oscillator strength in a hydrogenic approximation for inner shells (Desalvo & Rosa, 1987), each of which permits the simulation of the fast knock-on electrons. However, any characteristic energy loss process specific to a sample is omitted under the CSDA. Considering that Bethe's equation is valid only at sufficiently high electron energies, Rao-Sahib & Wittry (Rao-Sahib & Wittry, 1974) have empirically extrapolated Bethe stopping powers to the low energy region by assuming a parabolic function, $-dE/ds \propto E^{-1/2}$, which has been extensively used in the simulation of the slowing down process of slow electrons (Joy, 1987; Kotera, 1989; Luo et al., 1987; Newbury et al., 1990). But this formulation gives energy dependence opposite of that predicated by the Lindhard theory for free electron gas (Lindhard, 1954; Ritchie et al., 1969) and overestimates significantly the energy loss of low-energy electrons. Concerning secondary electron generation, both models of the secondary electron excitation assumed from the stopping power formula (Joy, 1987; Matsukawa & Shimizu, 1974; Murata et al., 1987) or from the Streitwolf (1959) equation (Koshikawa & Shimizu, 1973; Kotera, 1989; Kotera et al., 1990; Luo et al., 1987) have required fitting parameters in order to get the correct secondary electron yield.
Furthermore, the secondary emission process was simply described by an exponential decay law (Joy, 1985) or was hybridized with a cascade model of secondary production (Luo & Joy, 1990) and with emission processes (Koshikawa & Shimizu, 1973). Another unsatisfactory situation is that one usually divides the energy region for fast secondary electrons and the low secondaries to adopt different approaches for each (Ding & Shimizu, 1988a; Ding & Shimizu, 1989a; Kotera, 1989) because the available models of electron scattering and secondary generation were limited in certain energy range.
Therefore, a unified treatment of electron inelastic scattering and secondary electron generation is quite necessary. Perhaps the best approach should be based on a dielectric function which characterizes the specific excitation processes of a sample (Pines, 1964). A dielectric function $\varepsilon(\mathbf{q},\omega)$ can provide us with detailed knowledge of energy loss cross section and scattering angular distribution for electron inelastic scattering. This has been achieved (Cailler & Ganachaud, 1990; Ganachaud & Cailler, 1979a; Ganachaud & Cailler, 1979b) for free electron metal, Al, using the well-known Lindhard dielectric function describing the plasmon excitation and electron-hole pair production. Unfortunately, the ideal Lindhard dielectric function of free electron gas in the random phase approximation (Fetter & Walecka, 1971) is valid only for limited materials, that is, so-called free electron metals, and is hardly applicable to other materials such as transition and noble metals, for which the optical dielectric data have shown complexities due to interband transitions (Rather, 1980). Some modified analytical dielectric functions in the plasmon-pole approximation with damping (Brandt & Reinheimer, 1970) were also limited to materials, for which the damping plasmon dominates the energy loss processes of electrons, such as carbon and silicon (Desalvo et al., 1984). Furthermore, the theoretical calculation of $\mathbf{q}$-

dependent dielectric function, $\varepsilon(\mathbf{q},\omega)$, is difficult and has been numerically evaluated (Nizzoli, 1978; Singhal, 1975; Sramek & Cohen, 1972; Walter & Cohen 1972) only for selected $\mathbf{q}$s and the first few reciprocal lattice vectors using realistic band structure data for some simple metals and semiconductors (Sturm, 1982). In fact, the comprehensive first principle theoretical calculations for metals have been limited to $\varepsilon(\omega)=\varepsilon(\mathbf{q}=0,\omega)$ (Maksimov et al., 1988). It is thus impractical to use $\varepsilon(\mathbf{q},\omega)$ derived from a band structure calculation for a MC simulation, hence we have to use the optical dielectric data which are available experimentally from optical method and electron energy loss spectroscopy (Egerton, 1986). Systematic data of the dielectric constants have been provided and compiled for a number of materials for practical use (Hagemann et al., 1975; Palik, 1985; Palik, 1991) with advance in use of synchrotron radiation facilities.

Our first attempt (Ding & Shimizu, 1988a) had used the approach given by Powell (Powell, 1985). The $\mathbf{q}$-integrated excitation function for electron energy loss and production of secondary electrons is related to $\varepsilon(\omega)$ and a parameter, which was determined by fitting the calculated electron mean free path with experimental data. Reasonable accuracy has been achieved in the calculation of the energy distribution of backscattered electrons (Ding et al., 1988b). However, the angular information in electron inelastic scattering was accumulated by the integration over $\mathbf{q}$, and the parameter-involved approach is not favorable for general use. Particularly, this parameter does not allow describing the Bethe stopping powers at high energies, so that we had to use this simple dielectric model only for slow electrons.

According to Penn's work (Penn, 1987), the $\mathbf{q}$-dependent electron energy loss function may be derived from optical dielectric constants. This algorithm enables us to calculate energy loss cross section and scattering angular distribution required for a MC simulation of discrete electron inelastic scattering processes (Ashley, 1991; Ding & Shimizu, 1989b). It has been shown that the method yields the Bethe stopping powers at high energies (Ashley, 1988; Ding & Shimizu, 1989b), and the calculated electron mean free paths fit the experimental data in a wide energy region for many elements and compounds. This fact indicates that the dielectric function modeling is very useful for MC simulation of electron inelastic scattering. We have used it in the calculation of x-ray depth profiles (Ding & Wu, 1993) and background in Auger electron spectroscopy (Ding et al., 1994), and Tokesi et al. (Tokesi et al., 1996) have calculated the reflected electron energy loss spectrum. Jensen & Walker (Jensen & Walker, 1993) have also employed it to study the backscattering yield of positrons and electrons of high energies, but they failed to get good agreement with experimental data for electrons, partly because of the neglect of the secondary production. We shall demonstrate, by including cascade secondary electron generation that the backscattering yields as well as the angular energy distribution describe the precise experimental curve down to low energies very well. This modeling describes the inelastic scattering reasonably well, covering the wide energy range from several eV above the Fermi energy to several tens keV. Furthermore, the simulation of cascade production of secondary electrons included with discrete electron inelastic collisions can be directly made in a simple way.

Furthermore, great efforts have also been made for the structures simulation with complex geometries near term years. Some studies using a MC electron-trajectory simulation technique have been carried out for several kinds of simpler geometrical specimens (Gauvin, 1995; Hovington et al., 1997a; Hovington et al., 1997b; Drouin et al., 1997; Ly et al., 1995; Radzimski & Russ, 1995; Howell, 1996; Lowney, 1995; Lowney, 1996; Postek et al., 2002; Seeger et al., 2003; Yan & El Gomati, 1998). Gauvin (Gauvin, 1995) performed

simulations of X-ray images and BSE images for a spherical inclusion of homogeneous composition embedded in a matrix, based on use of Mott elastic-scattering cross sections and a modified continuous slowing-down approximation. Their CASINO program is a single-scattering MC simulation of electron trajectories in a solid, specially designed for the interactions of low-energy electrons in bulk solids and thin foils, and can be used to generate the usual recorded signals in a SEM (X-rays, SEs, and BSEs) either for point analysis, line-scans, or images (Hovington et al., 1997a; Hovington et al., 1997b; Drouin et al., 1997). Ly et al. simulated SEM images of spheres of different materials on a substrate surface and at various depths beneath the flat surface (Ly et al., 1995). Radzimski and Russ performed simulations of BSE images of three-dimensional (3D) multilayer and multi-element structures, on the basis of a single-scattering procedure, to study electron beam and detector characteristics (Radzimski & Russ, 1995). Their simulation procedure also took into account the effects of the electrical and angular characteristics of a solid-state detector and the effect of the electron beam size on image quality and certain artifacts. Howell et al. developed a program to illustrate macro topographies on electron backscattering (Howell, 1996). This program can simulate a target constructed with a choice of a flat surface, a circular filament, or a rough surface simulated by a sine wave. Another MC simulation program, MONSEL, has been used to model the interaction of an electron beam with one or two lines lithographically produced on a multilayer substrate (Lowney, 1995; Lowney, 1996). The simulated signals include transmitted, backscattered and secondary electrons. Another application of this program was concerned with the simulation of two-dimensional (2D) SE and BSE images of a simple notch (Postek et al., 2002). Recently, the MONSEL program has been extended by Seeger et al. to simulate SE and BSE images of a complex structure consisting of many triangles to create a complex specimen surface (Seeger et al., 2003). Certain programming techniques enabled faster calculations. Yan and Gomati developed a 3D MC code to simulate images of BSEs and AEs for a more complex specimen (Yan & El Gomati, 1998). Their code required the 3D geometric structure to be described in analytic form.

Because of the difficulty of simulating secondary electron generation and emission processes for specimens with complex structures, most previous studies emphasized simulation of BSE images with very simple structures, and only a few were capable of simulating SE images for specimens with complex structures. Also, inhomogeneous distribution of chemical composition inside a sample has not been considered generally. For this, the constructive solid geometry (CSG) modeling (Ding & Li, 2005; Li & Ding, 2005; Yue et al., 2005) and finite element triangle mesh modeling (Ding & Wang, unpublished; Li et al., 2008) have been developed to construct arbitrary geometric structure. Also, the inhomogeneous distribution of chemical composition inside a complex structure has been used in the subsequent researches (Yue et al., 2005; Li et al., 2009).

In this respect, the MC model (Li et al., 2008) used here for SEM/SAM image simulation has been improved in three aspects with respect to our previous simulation models (Ding & Shimizu, 1996; Ding & Li, 2005; Li & Ding, 2005; Shimizu & Ding, 1992; Yue et al., 2005): First, the full Penn dielectric function (Mao et al., 2008) is employed for the treatment of electron inelastic scattering to replace single-pole approximated (SPA) dielectric function. Second, we combine the constructive solid geometry modeling (Ding & Li, 2005; Li & Ding, 2005; Yue et al., 2005) and finite element triangle mesh modeling (Ding & Wang, unpublished; Li et al., 2008) to construct an arbitrary geometric structure. Third, we use a ray-tracing technique (Ding & Li, 2005; Li & Ding, 2005; Yue et al., 2005) for an

inhomogeneous specimen with a complex geometric structure and introduce the space subdivision method to accelerate the calculation (Ding & Wang, unpublished; Li et al., 2008). Additionally, a rough surface geometry model is introduced to construct the sample surface, together with using of a ray-tracing technique (Li & Ding, 2005) in the calculation procedure of electron step length. Appropriate boundary correction (Yue et al., 2005) had also been considered in order to treat the reflection/refraction of low energy secondary electrons when they pass through an interface separating different materials. The present MC simulation model, therefore, is probably most useful for application to SEM/SAM. In Sec. 2, detailed physical/mathematical model of electron transportation, MC simulation method and complex construction algorithms will be introduced. And then the applications for simulation of CD-SEM images for critical dimension (CD) nanometrology and simulation study of SAM images will be demonstrated in Sec. 3 and 4, respectively.

2. Monte Carlo modeling

Programming a simulation code for a study of electron-solid interaction relies on knowledge about two aspects: first, the theoretical description of electron scattering in the solid and cascade process; second, the reasonable description of the sample geometry boundary with corretion to the MC procedure. A basic MC model for simulation on a semi-infinite sample with flat surface can be established based on well understanding of the first aspect; the MC procedure deal with the essential processes of the interaction between incident electrons and solid. To implement the MC simulation for a sample with complex geometry, the modeling of complex sample geometry becomes indispensable.

2.1 Physical modeling of electron transport

The interaction between the electron and solid consists of three elemental physical processes: elastic scattering, inelastic scattering and cascade electron generation. The electron elastic and inelastic scattering dominate the deflection and energy loss of electrons, respectively. Following electron inelastic scattering events, the energy transferred from an electron to a solid may induce the generation of cascading electrons (excitation of solid electrons) and this process will lead to the generation of signal electrons, especially SE signals. In a MC model for a semi-infinite sample with flat surface, the reasonable description of these three elemental processes is demanded. A detailed theoretical algorithm to deal with interaction processes is described below and a description of the MC procedure is also given.

2.1.1 Elastic scattering

When a moving electron meets the positively-charged nucleus, it may be deflected without energy loss (ignored the recoil energy) due to the electric interaction. This phenomenon is called elastic scattering, which could be described by elastic scattering cross section in unit of area. Rutherford equation is the classical formulation of differential elastic scattering cross section with scattering angle,

$$\frac{d\sigma_e}{d\Omega} = \frac{Z^2 e^4}{4E^2\left(1-\cos\theta+2\beta\right)^2}, \tag{1}$$

where Z, e, E and θ are the atomic number, electron charge, kinetic energy of the moving electron and scattering angle, respectively. β is a screening parameter used to include the

influence of the atomic electron cloud. Rutherford elastic scattering cross section has been widely used in the MC simulation in past year because of its simplicity. However, the Rutherford elastic cross section shows its limitation when it applies for slow electron and/or heavy element (Walker, 1971). Furthermore, considering the wave properties of electrons, more precise elastic scattering cross section should be derived in the quantum picture instead of classical picture (Ding & Shimizu, 2003).

According to Mott (Mott, 1929), by solving Dirac equation a relativistic representation of the differential elastic scattering cross section is given by,

$$\frac{d\sigma_e}{d\Omega} = |f(\theta)|^2 + |g(\theta)|^2, \tag{2}$$

where the scattering amplitudes is derived by a partial wave expansion method (Mott & Massey, 1965):

$$\begin{aligned} f(\theta) &= \frac{1}{2ik}\sum_{l=0}^{\infty}\left[(l+1)\left(e^{i2\delta_l^+}-1\right)+l\left(e^{i2\delta_l^-}-1\right)\right]P_l(\cos\theta), \\ g(\theta) &= \frac{1}{2ik}\sum_{l=1}^{\infty}\left(-e^{i2\delta_l^+}+e^{i2\delta_l^-}\right)P_l^1(\cos\theta), \end{aligned} \tag{3}$$

where $\hbar k$ is the electron momentum, $P_l(\cos\theta)$ and $P_l^1(\cos\theta)$ are Legendre and the first order associated Legendre functions, δ_l^+ and δ_l^- are the phase shifts of the l th partial wave for spin up and spin down electrons, respectively. A detailed numerical technique for calculation the phase shift could be found in Yamazaki's work (Yamazaki, 1977) which follows that of Bunyan & Schonfelder (Bunyan & Schonfelder, 1965). There are some published databases (Fink & Yates, 1970; Fink & Ingram, 1972; Gregory & Fink, 1974; Mayol & Salvat, 1997) in which the phase shifts and differential elastic scattering cross section have been tabulated. The most recent database is released by National Institute of Standards and Technology (NIST) (http://www.nist.gov/srd/nist64.htm) for providing differential and total elastic electron scattering cross sections, phase shifts and transport cross sections.

A comparison between Mott and Rutherford elastic scattering cross sections for Au at electron energy of 400 eV is shown in Fig. 1. Some obvious structures appear at lager scattering angles, which have been verified through a comparison with experimental measurements performed on Au vapor (Ding, 1990). They may be smoothed at high energies because a large number of partial waves are involved. According to a systematic comparison between these two cross sections (Ichimura, 1980; Shimizu & Ichimura, 1981), Mott elastic cross section is shown more accurate for heavy atoms and for slow electrons because spin-orbit interactions, which is dealt with more reasonably in Eq. (2), are important.

The total elastic cross section σ_e can be obtained by integrating the differential elastic scattering cross section over whole solid angles,

$$\sigma_e = \int \frac{d\sigma_e}{d\Omega} d\Omega = 2\pi \int_0^{\pi} \sin\theta \left\{ |f(\theta)|^2 + |g(\theta)|^2 \right\} d\theta, \tag{4}$$

which is related to elastic scattering mean free path in solid via

$$\lambda_e = \left(N\sigma_e\right)^{-1}, \tag{5}$$

where $N = N_A\rho/A$ is the density of atoms, N_A is Avogadro's number, ρ is the density and A is the atomic weight. The elastic scattering mean free path is the average distance between two successive elastic collisions between a moving electron and solid atoms, which is the basic information requested in the MC simulation for electron transport in solids.

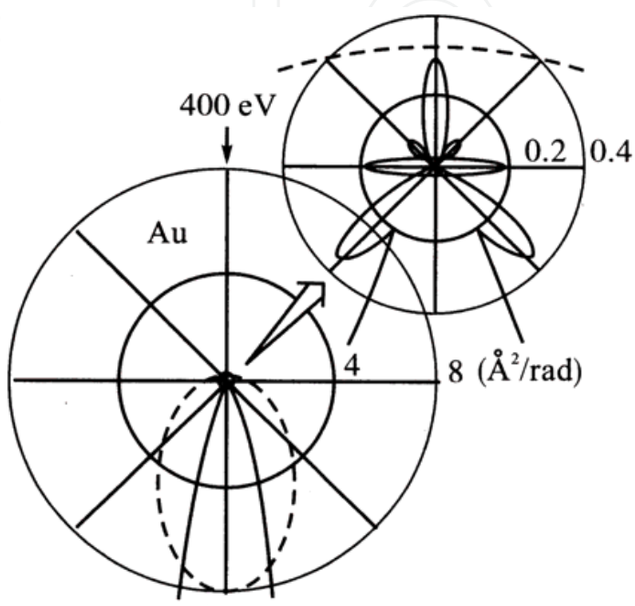

Fig. 1. Polar plot of differential electron elastic scattering cross sections for Au atom at electron energy of 400 eV. Mott and Rutherford cross sections are shown by solid and dashed lines, respectively.

2.1.2 Inelastic scattering

The moving electron can also encounter collisions with the solid electrons, accompanied by energy loss and excitation of solid electrons. This type of collisions involving energy transfer is called inelastic scattering, and can be described by the differential inverse inelastic mean free path (Ding, 1990),

$$\frac{d^2\lambda_{in}^{-1}}{dqd\omega} = \frac{\hbar}{\pi a_0 E}\mathrm{Im}\left\{\frac{-1}{\varepsilon(q,\omega)}\right\}\frac{1}{q}, \tag{6}$$

where λ_{in} denotes inelastic mean free path (IMFP), $\hbar q$ and $\hbar\omega$ are momentum transfer and energy loss, respectively; a_0 is Bohr radius and $\hbar$ is Planck constant. $\mathrm{Im}\left\{-1/\varepsilon(q,\omega)\right\}$ is the energy loss function and $\varepsilon(q,\omega)$ is the dielectric function. In Eq. (6), the energy loss function is the only unknown quantity. Once the energy loss function is determined, the electron IMFP can be theoretically evaluated by the integration

$$\lambda_{in}^{-1} = \int_0^{E-E_F} d\omega \int_{q_-}^{q_+} dq \frac{d^2\lambda_{in}^{-1}}{dqd\omega}, \tag{7}$$

where the integration limits, $\hbar q_{\pm} = \sqrt{2m}\left(\sqrt{E} \pm \sqrt{E-\hbar\omega}\right)$, are the largest and the smallest momentum transfers kinematically allowed for given E and ω. The restriction to $\hbar\omega \le E - E_F$ is due to the Pauli exclusion principle that an electron can not fall into the Fermi sea which is already occupied by electrons in the solid.

It is difficult to give a theoretical calculation for the energy loss function because of its complexity. The energy loss function includes the contributions of plasmon excitation, valance electron excitation, inner-shell electron excitation and so on. However, considering the fact that the optical energy loss function $\mathrm{Im}\{-1/\varepsilon(\omega)\}$ is the limit of energy loss function as $q \to 0$, an alternative way, by extrapolating optical energy loss function to (q, ω)-plane, can be applied to theoretically evaluate energy loss function. The advantage of this method is that abundant optical data for $\varepsilon(\omega)$ in the loss energy range of $10^0 - 10^4$ eV are available and are compiled in a database (Palik, 1985; Palik, 1991); use of these data derived from experiments allows a more accurate description of electronic excitation in real materials. Assuming the statistical approximation by neglecting the vertex correction, self-consistency, exchange and correlation and considering that the charge distribution in the Wigner-Seitz cell is spherically symmetric, Penn (Penn, 1987) has proposed an extrapolation method by expanding the energy loss function in terms of the Lindhard energy loss function without using any fitting parameters:

$$\mathrm{Im}\left\{\frac{-1}{\varepsilon(q,\omega)}\right\} = \int_0^\infty d\omega_p g(\omega_p)\,\mathrm{Im}\left\{\frac{-1}{\varepsilon_L(q,\omega;\omega_p)}\right\}, \tag{8}$$

where the expansion coefficient $g(\omega)$ is related to the optical energy loss function by

$$g(\omega) = \frac{2}{\pi\omega}\mathrm{Im}\left\{\frac{-1}{\varepsilon(\omega)}\right\} \tag{9}$$

and $\varepsilon_L(q,\omega;\omega_p)$ is the Lindhard dielectric function (Lindhard, 1954) of the free electron gas with plasmon energy $\hbar\omega_p$ in the long-wave limit,

$$\varepsilon_L^r = 1 + \frac{2}{\pi a_0 q}\frac{1}{Z}\left[\frac{1}{2} + \frac{1}{8Z}F\left(Z - \frac{X}{4Z}\right) + \frac{1}{8Z}F\left(Z + \frac{X}{4Z}\right)\right], \tag{10}$$

$$\varepsilon_L^i = \begin{cases} \dfrac{1}{8a_0 k_F}\dfrac{X}{Z^3} & , 0 \le X \le 4Z(1-Z); \\ \dfrac{1}{8a_0 k_F}\dfrac{1}{Z^3}\left[1 - \left(Z - \dfrac{X}{4Z}\right)^2\right] & , \left|4Z(1-Z)\right| \le X \le 4Z(1+Z); \\ 0 & , \text{otherwise}, \end{cases} \tag{11}$$

where $F(x) = (1-x^2)\ln\left|(x+1)/(x-1)\right|$, $X = \hbar\omega/E_F$, $Z = q/2k_F$. $E_F = \hbar^2 k_F^2/2m$ is the Fermi energy and k_F is the Fermi wave vector. They are related to the plasmon energy through the electron density. ε_L^r and ε_L^i denote the real and the imaginary parts of the Lindhard dielectric function, respectively.

The above extrapolation method is called the full Penn algorithm (FPA) here. In the same paper Penn has further introduced the well-known single-pole approximation (SPA) to simplify the calculation. The approximation was indeed useful for the initial guide to find the trend of the energy dependence of IMFP, so that many other calculations followed the same route (Ding & Shimizu, 1988; Tanuma et al., 1988; Tanuma et al., 2005). The detail implementation of the FPA and SPA is given below, together with a comparison between them, which indicates the validity of SPA.

The implementation of FPA is carried out as follows. For a free electron gas with a certain electron density or plasmon frequency, ω_p, only the area in the (q,ω)-plane along the plasmon dispersion line, where $\varepsilon_L^r = 0$ and $\varepsilon_L^i = 0$, can have a contribution to the integration in Eq. (8); the Lindhard energy loss function along this plasmon dispersion line is divergent; while for $\varepsilon_L^i \neq 0$, only the single electron excitation is allowed. Then we need to divide the calculation into two parts, i.e. single electron excitation and plasmon excitation in the area $\varepsilon_L^i \neq 0$ and $\varepsilon_L^i = 0$, respectively (Jensen & Walker, 1993).

The single electron excitation part of the calculation is performed directly with Eqs. (8)-(11),

$$\mathrm{Im}\left\{\frac{-1}{\varepsilon(q,\omega)}\right\}_e = \int_0^\infty d\omega_p g(\omega_p)\,\mathrm{Im}\left\{\frac{-1}{\varepsilon_L(q,\omega;\omega_p)}\right\}\Theta\left[q^+(\omega;\omega_p)-q\right]\Theta\left[q-q^-(\omega;\omega_p)\right]. \quad (12)$$

Here $\mathrm{Im}\{-1/\varepsilon(q,\omega)\}_e$ represents the energy loss function of the single electron excitation part, and q^- and q^+ are the left and right boundaries of the area for $\varepsilon_L^i \neq 0$, respectively,

$$\begin{cases} q^-(\omega;\omega_p) = -k_F(\omega_p) + \sqrt{k_F^2(\omega_p) + 2m\omega/\hbar} \\ q^+(\omega;\omega_p) = k_F(\omega_p) + \sqrt{k_F^2(\omega_p) + 2m\omega/\hbar} \end{cases}. \quad (13)$$

Note that in Eq. (12) the plasmon frequency ω_p is used as a variable which scans over the loss energy range of the available optical data. For the plasmon excitation part, because of the existence of the positive infinity, the integration of ω_p can be removed to give the energy loss function of plasmon excitation,

$$\mathrm{Im}\left\{\frac{-1}{\varepsilon(\omega,q)}\right\}_{pl} = g(\omega_0)\frac{\pi}{\left|d\varepsilon_L^r(q,\omega;\omega_0)/d\omega_0\right|}\Bigg|_{\varepsilon_L^r=0}\Theta\left[q^-(\omega;\omega_0)-q\right], \quad (14)$$

where the single-valued ω_0 satisfies $\varepsilon_L^r(q,\omega;\omega_0) = 0$; it is a numerical solution of the plasmon frequency at $q = 0$ for the plasmon dispersion line that passes through the given (q,ω)-point. The slope of the real part of the Lindhard dielectric function is

$$\begin{aligned} d\varepsilon_L^r(q,\omega;\omega_p)/d\omega_p\big|_{\varepsilon_L^r=0} = -\frac{2}{3\omega_p}\Bigg\{2 + \frac{1}{\pi a_0 q}\frac{1}{Z} + \frac{1}{2\pi a_0 q}\frac{1}{Z} \\ \times\left[2 - C_1\ln\left|\frac{C_1+1}{C_1-1}\right| - C_2\ln\left|\frac{C_2+1}{C_2-1}\right| + \frac{X}{4Z^2}\left(C_1\ln\left|\frac{C_1+1}{C_1-1}\right| - C_2\ln\left|\frac{C_2+1}{C_2-1}\right|\right)\right]\Bigg\}, \end{aligned} \quad (15)$$

where $C_1 = Z - X/4Z$ and $C_2 = Z + X/4Z$. The condition $\Theta\left[q^-(\omega;\omega_0)-q\right]$ requires the plasmon dispersion line for $\varepsilon_L^r(q,\omega;\omega_0) = 0$ to be terminated at the left boundary of the area

for single electron excitation. For Al, the dominant intensity of $\mathrm{Im}\left\{-1/\varepsilon(q,\omega)\right\}_{pl}$ is around the bulk plasmon frequency, so $\omega_0 \approx 15$ eV with certain expansion for the peak width. The total energy loss function is the summation of these two parts,

$$\mathrm{Im}\left\{\frac{-1}{\varepsilon(q,\omega)}\right\} = \mathrm{Im}\left\{\frac{-1}{\varepsilon(q,\omega)}\right\}_e + \mathrm{Im}\left\{\frac{-1}{\varepsilon(q,\omega)}\right\}_{pl}. \tag{16}$$

On the other hand, by SPA the Lindhard energy loss function is simply given by

$$\mathrm{Im}\left\{\frac{-1}{\varepsilon_L(q,\omega;\omega_p)}\right\} \approx \frac{\pi}{2}\frac{\omega_p^2}{\omega_q}\delta(\omega-\omega_q), \tag{17}$$

where the equation

$$\omega_q^2(\omega_p) = \omega_p^2 + \frac{1}{3}v_F^2(\omega_p)q^2 + \left(\hbar q^2/2m\right)^2 \tag{18}$$

defines the plasmon dispersion ω_q, and $v_F(\omega_p)$ is the Fermi velocity of an electron gas with the plasmon frequency ω_p. The energy loss function then becomes

$$\mathrm{Im}\left\{\frac{-1}{\varepsilon(q,\omega)}\right\} \approx \frac{\omega_0}{\omega_q}\mathrm{Im}\left\{\frac{-1}{\varepsilon(\omega_0)}\right\}, \tag{19}$$

where ω_0 is the solution of equation $\omega_q(q,\omega_0) = \omega$. Basically, ω_0 is similarly obtained as in FPA except that now the dispersion equation is given explicitly. SPA is a good approximation for materials, such as transition and noble metals, that have broad optical energy loss functions in the loss energy region of 10^0-10^2 eV, but not for free-electron-like materials for which a sharp plasmon peak dominates the optical energy loss function.

Fig. 2 shows a perspective view of the energy loss function obtained by FPA and SPA for Al and Cu. The optical data for Al and Cu are taken from (Shiles et al., 1980) and (Hagemann et al., 1974), respectively. The difference between the two methods is mostly significant at the low loss-energy and low momentum-transfer area (Fig. 2); for energy loss and momentum transfer higher than shown in Fig. 2, the energy loss function forms the Bethe ridge without apparent difference between FPA and SPA. For Al, the FPA energy loss function still has a limited but nonzero intensity for single particle excitation even for $\hbar\omega < \hbar\omega_p$. This is an important source for the creation of low energy secondary electrons in a MC simulation; the plasmon excitation intensity decays quickly when the dispersion enters into the single particle excitation region (Fig. 2(a)). SPA on the other hand completely ignores the single electron excitation. This missing contribution is compensated to the intensity of plasmon excitation whose dispersion line extends up to large q values while the ridge height decays very slowly (Fig. 2(b)). Therefore, there is no any energy loss when $E < \hbar\omega_p$. This becomes a serious problem for low energy electron inelastic scattering. For Cu, the differences still exist (Figs. 2(c)-(d)), but owing to the rather smooth and broad shape of the optical energy loss function the inelastic scattering probability obtained by the two methods for low losses and at low energies should be comparable.

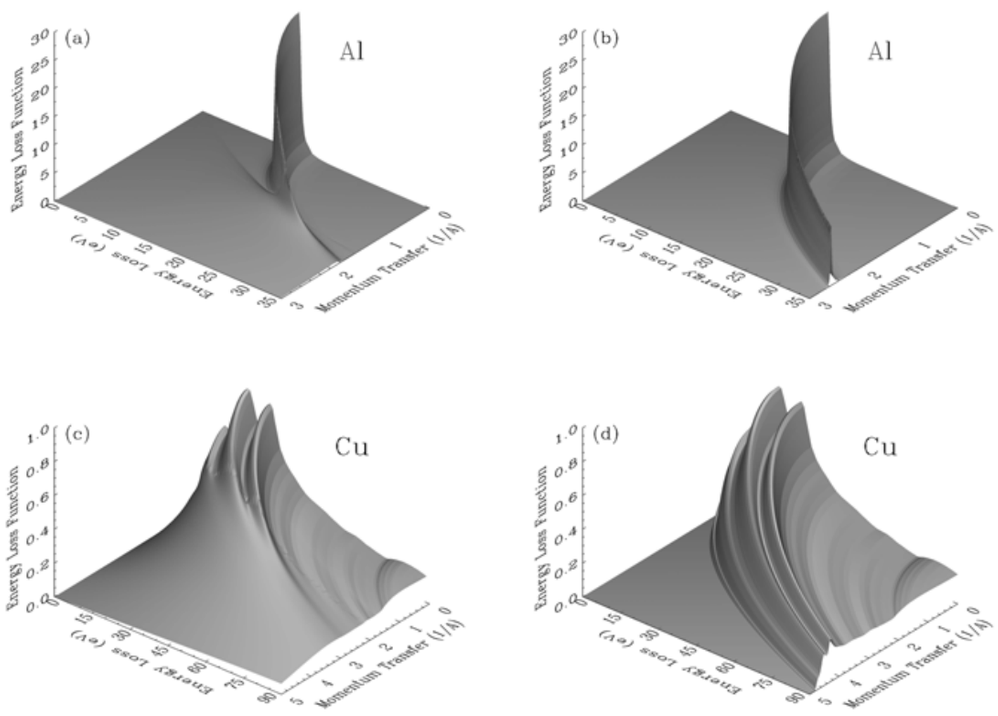

Fig. 2. Perspective plot of the energy loss function as a function of momentum transfer and energy loss, calculated by the full Penn algorithm (FPA) and single-pole approximation (SPA) for Al and Cu: (a) Al, FPA; (b) Al, SPA; (c) Cu; FPA; (d) Cu, SPA.

2.1.3 Electron cascading

MC simulation is a powerful technique for simulation of secondary electron emission phenomena and calculation of the related energy spectra and yields of secondary electrons (Shimizu & Ding, 1992; Ding & Shimizu, 1996; Ding et al., 2001; Ding et al., 2004a). As described above, the generation of SEs is a cascade process due to multiple inelastic scattering. The differential inverse inelastic mean free path given by Eq. (6) is used to describe the energy loss of moving electrons, as well as the cascade secondary electron generation.

The SPA was used in our previous simulation of SEs (Ding et al., 2001). After sampling the energy loss, ΔE, for an inelastic scattering event, a SE is assumed to be excited from the Fermi sea by adding the loss energy ΔE of the moving electron to the initial kinetic energy of the SE, with the excitation probability being proportional to a joint density of states of free electrons, i.e. $p(E', \Delta E) \propto \sqrt{E'(E' + \Delta E)}$, where $E' < E_F$ is the energy of the Fermi sea electrons. This assumption follows Chung's work (Chung & Everhart, 1977) on plasmon damping. Under this procedure, with the differential energy loss cross section or the secondary electron excitation function determined using SPA, all SEs were assumed to be excited in the same way as through plasmon damping.

However, the treatment of secondary electron generation by FPA needs to consider two individual mechanisms as in the calculation of differential inverse inelastic mean free paths, i.e. single electron excitation and plasmon damping. After the momentum transfer $\hbar\mathbf{q}$ and the energy transfer $\hbar\omega$ are determined by a MC sampling procedure, we specify that single

electron excitation occurs if $q^{-}\left(\omega;\omega_p\right) < q < q^{+}\left(\omega;\omega_p\right)$, and plasmon excitation occurs if $q < q^{-}\left(\omega;\omega_p\right)$, where the value of $\hbar\omega_p$ is determined from the Fermi energy E_F through the relation with electron density.

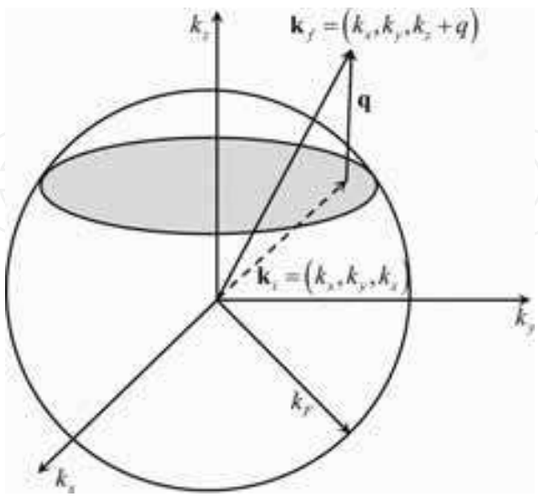

Fig. 3. Illustration of the condition for single electron excitation. The k_z axis is along the direction of $\mathbf{q}$. The shaded disk is the area that contains allowed momenta of excited electrons. An electron in the Fermi sphere at initial state of $\mathbf{k}_i = \left(k_x, k_y, k_z\right)$ gains the loss energy $\hbar\omega$ and momentum transfer $\hbar\mathbf{q}$ from a scattering electron and transits to the final state of $\mathbf{k}_f = \left(k_x, k_y, k_z + q\right)$ by energy and momentum conservations. Notice that if an electron excited from the interior of the allowed disk does not satisfy the condition that $\left|\mathbf{k}_f\right| > k_F$, the allowed disk becomes an annulus.

The secondary electron generation via plasmon damping can be treated exactly the same as in the previous model. For a single electron excitation, the probability distribution for exciting an electron of the momentum $\mathbf{k}_i$ from the Fermi sea is given by (Ganachaud & Cailler, 1979a; Ganachaud & Cailler, 1979b),

$$p(|\mathbf{k}_i| < k_F; \mathbf{q}, \omega) = \int d\mathbf{k}_i \delta\left[\hbar\omega - \frac{\hbar^2}{2m}(2\mathbf{k}_i \cdot \mathbf{q} + q^2)\right] \Theta(k_F - |\mathbf{k}_i|)\Theta(|\mathbf{k}_f| - k_F), \tag{20}$$

where $\mathbf{k}_f = \mathbf{k}_i + \mathbf{q}$ is the momentum of the excited SE after the inelastic collision. As shown in Fig. 3, let the *z*-direction of the wave vector of the electron in the Fermi sea be the direction of the momentum transfer; by the energy and momentum conservations we have

$$\begin{cases} \dfrac{\hbar^2\mathbf{k}_i^2}{2m} = \dfrac{\hbar^2}{2m}\left(k_x^2 + k_y^2 + k_z^2\right) = E \\ \dfrac{\hbar^2\mathbf{k}_f^2}{2m} = \dfrac{\hbar^2}{2m}\left[k_x^2 + k_y^2 + \left(k_z + q\right)^2\right] = E + \hbar\omega \end{cases}, \tag{21}$$

or, equivalently, the components of $\mathbf{k}_i = \left(k_x, k_y, k_z\right)$ have to satisfy two conditions: (1) $k_x^2 + k_y^2 + k_z^2 < 2mE_F/\hbar^2$; (2) $k_x^2 + k_y^2 + \left(k_z + q\right)^2 > 2mE_F/\hbar^2$. The electrons that can be excited therefore lie in a disk of Fermi sphere defined by

$$k_z = \left(2m\omega - \hbar q^2\right)\Big/ 2\hbar q \,. \tag{22}$$

The momentum $\mathbf{k}_i$ of the electron to be excited can be selected from the disk with two random numbers. This determines the momentum $\mathbf{k}_f$ and the kinetic energy $\hbar^2\mathbf{k}_f^2/2m$ of the secondary electron after excitation.

2.1.4 General Monte Carlo simulation procedure

Base on the knowledge of electron elastic and inelastic scattering and electron cascading described above, a general MC simulation procedure is given below (Ding, 1990; Ding & Shimizu, 1996).

The present MC simulation of electron trajectories penetrating a sample is based on a description of individual electron scattering processes, as schematically shown in Fig. 4. The problem is, then, reduced to the determination of values of physical quantities such as step length, scattering angle, energy loss, and so forth, in a particular scattering event. The MC technique basically chooses these values by random numbers according to respective cross sections. Given a probability distribution function $P(x)$ for a variable x, we can derive a normalized accumulation function $A(x)$,

$$A(x) = \int_{x_{\min}}^{x} P(x')dx' \Big/ \int_{x_{\min}}^{x_{\max}} P(x')dx' \,, \tag{23}$$

and determine a specific value of x from $A(x) = R$ for a given value of uniform random number $R \in [0,1]$.

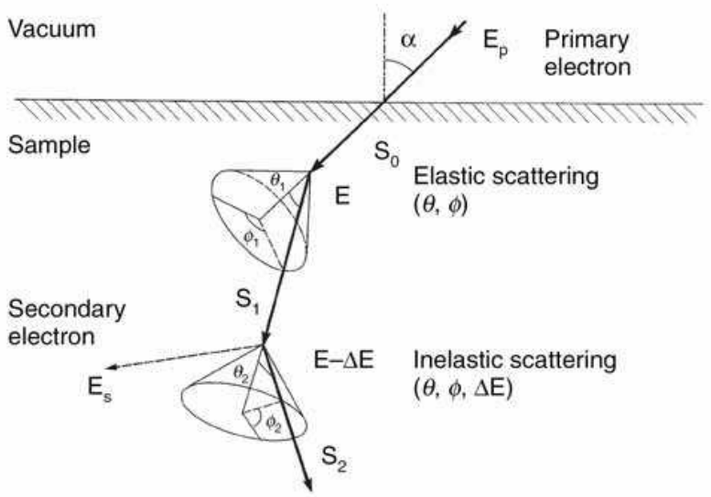

Fig. 4. Scheme showing the discrete model for Monte Carlo simulation of electron scattering.

Suppose that the step length, s, of a scattering electron between two successive collision events obeys the Possion stochastic process with the probability distribution

$$P(s) = \lambda_m^{-1} e^{-s/\lambda_m} \,, \tag{24}$$

where λ_m is the total mean free path related to the corresponding elastic mean free path and the inelastic mean free path through

$$\lambda_m^{-1} = \lambda_e^{-1} + \lambda_{in}^{-1} . \tag{25}$$

An electron will then suffer a scattering event when it passes s selected by a random number R_1 via

$$s = -\lambda_m \ln R_1 . \tag{26}$$

Another random number, R_2, determines the type of individual scattering event followed after passing s: If

$$R_2 < \lambda_e^{-1} \Big/ \lambda_m^{-1} , \tag{27}$$

it is elastic, otherwise it is inelastic.
For elastic scattering, it is attributed to an atom of *i* th element if

$$\frac{\sum_{j=1}^{i-1} C_j^a \Big/ \lambda_e^j}{1/\lambda_e} < R_3 < \frac{\sum_{j=1}^{i} C_j^a \Big/ \lambda_e^j}{1/\lambda_e} , \tag{28}$$

where $\left(\lambda_e^0\right)^{-1} = 0$, holds. The angle of scattering is calculated by

$$R_4 = \int_0^{\theta} \left(\frac{d\sigma_e}{d\Omega}\right)_{\text{Mott}} \sin\theta' d\theta' \Bigg/ \int_0^{\pi} \left(\frac{d\sigma_e}{d\Omega}\right)_{\text{Mott}} \sin\theta' d\theta' , \tag{29}$$

with the differential cross section for ith element, and the azimuthal angle is assumed to be isotropic,

$$\phi = 2\pi R_5 . \tag{30}$$

Regarding inelastic scattering, the equation similar to Eq. (28) can be applied by replacing λ_e with λ_{in}, and λ_e^j with λ_{in}^j, for an alloy-like sample described by the sets of dielectric functions for each component, in the sense that it is not an atom but the constitutive electrons themselves that contribute to inelastic collision. For a compound-like sample, the dielectric function is given such as to treat the material as a whole, and it is therefore not necessary to specify a particular element. In the next step we determine the amount of energy loss ΔE by the equation

$$R_6 = \int_0^{\Delta E} \frac{d\lambda_{in}^{-1}}{d(\Delta E')} d(\Delta E') \Bigg/ \int_0^{E-E_F} \frac{d\lambda_{in}^{-1}}{d(\Delta E')} d(\Delta E') , \tag{31}$$

It should be noted that the zero level of kinetic energy of electrons has been taken as the bottom of the valence band. The inelastic scattering angle is calculated by

$$R_7 = \int_0^{\theta} \frac{d^2\lambda_{in}^{-1}}{d\Omega d(\Delta E)} \sin\theta' d\theta' \Bigg/ \int_0^{\pi} \frac{d^2\lambda_{in}^{-1}}{d\Omega d(\Delta E)} \sin\theta' d\theta' , \tag{32}$$

once the energy loss ΔE is determined in a preceding stage by Eq. (31), where the double differential cross section with respect to energy loss and solid angle can be obtained from

Eq. (6) by transforming variable q to θ. The energy and the momentum conservation give the relation

$$(\hbar q)^2 / 2m = 2E - \Delta E - 2\sqrt{E(E-\Delta E)}\cos\theta , \tag{33}$$

with which the change of variable can be made. Hence, we have

$$\frac{d^2\lambda_{in}^{-1}}{d\Omega d(\Delta E)} = \frac{1}{(\pi a_0 e)^2 E}\mathrm{Im}\left\{\frac{-1}{\varepsilon(q,\omega)}\right\}\frac{1}{q^2}\sqrt{E(E-\Delta E)} . \tag{34}$$

It can be shown that the angular distribution is proportional to θ^{-2} for small θ and the forward scattering is strongly preferred. The azimuthal angle in inelastic scattering is also determined by Eq. (30).

Followed by an electron inelastic scattering event, in which the energy loss ΔE, momentum transfer $\hbar q$ and coordinates (the position where inelastic scattering happens) are suitably determined, a SE would be generated; its initial energy E_2 (the kinetic energy equals to $E_2 + \Delta E$ after excitation) is determined from

$$R_8 = \frac{\int_0^{E_2}\sqrt{E'(E'+\Delta E)}dE'}{\int_0^{E_F}\sqrt{E'(E'+\Delta E)}dE'} , \tag{35}$$

in SPA, or, for plasmon excitation in FPA. The polar and azimuthal angles of the cascade electron are decided from momentum conservation as

$$\sin\theta_2 = \cos\theta, \quad \phi_2 = \pi + \phi . \tag{36}$$

For single electron excitation in FPA, by sampling a point in a disk/ annulus (Eq. (22)), the energy and direction of the SE can be also easily decided by Eq. (21). The coordinates of the SE is set as that at the scattering point. As the energy, direction and coordinates of the SE are determined, they are stored in memories of a computer. After finishing the tracing of the primary electron all the information of the cascade electron stored are recalled and the trajectory is simulated in a same way as for a primary electron.

The scattering angle in Eq. (29) and Eq. (32) and the azimuthal angle in Eq. (30) are given in a coordinate system moving with the tracing electron (Fig. 4). When these angles are transformed into a coordinate system fixed in the sample, the position at the next scattering point can be determined. Repeating above procedures, we get a trajectory of the penetrating electron which either terminates in the sample when its kinetic energy falls below a cut-off energy E_c or escapes from the surface.

It should be noted that in the simulation, the reference energies (bottom of valence band or vacuum level) depends on electron location. For a primary electron penetrating into the surface from vacuum the energy of the electron before first inelastic collision is given by

$$E = E_P + U_0 , \tag{37}$$

where the primary energy, E_P is measured from the vacuum level and E from the bottom of valence band. The inner potential, U_0, is approximated by the sum of Fermi energy and work function,

$$U_0 = E_F + W_F \,. \tag{38}$$

In the case of electron ejection into the vacuum from the sample, the energy measured from the vacuum level is

$$E = E' - U_0 \,, \tag{39}$$

and the ejection angle, ϑ, measured from the surface normal, is found by the momentum conservation parallel to surface (like the light deflection at the interface of media),

$$\sqrt{E}\sin\vartheta = \sqrt{E'}\sin\vartheta' \,, \tag{40}$$

where the superscript denotes the corresponding quantities inside the sample. It should be noted that the surface barrier inhibits an electron from escaping from the surface into vacuum with an angle $\vartheta' > \vartheta_c$, where

$$\vartheta_c = \sin^{-1}\sqrt{1 - \frac{U_0}{E'}} = \cos\sqrt{\frac{U_0}{E'}} \,. \tag{41}$$

The quantum mechanical representation of the transmission coefficient is given by (Cohen-Tannoudji et al., 1977)

$$T_q(E', \vartheta') = \begin{cases} \dfrac{4\sqrt{1 - U_0/E'\cos^2\vartheta'}}{\left[1 + \sqrt{1 - U_0/E'\cos^2\vartheta'}\right]^2}, & \text{if } E'\cos^2\vartheta' > U_0; \\ 0, & \text{otherwise.} \end{cases} \tag{42}$$

By using another random number R_8, whether the electron could emit or not can be decided as

$$\begin{cases} \textit{emitted}, & \text{if } R_9 < T_q(E', \vartheta'); \\ \textit{absorbed}, & \text{otherwise.} \end{cases} \tag{43}$$

2.2 Geometry modeling of complex structure

The request of simulation for inhomogeneous sample with complex geometry structure demands an efficient structure modeling to be included in a MC simulation. There are two questions to be settled, i.e., how to construct a complex geometry and how to correct the flight path between two successive collisions.

To solve the first question, the CGS modeling (Ding & Li, 2005; Li & Ding, 2005) and finite element triangle mesh modeling (Ding & Wang, unpublished; Wang, 2006; Li et al., 2008; Li, 2009) have been bring forward. The detail will be introduced below.

To the second question, considering an inhomogeneous sample formed of many different spatial zones, each of which is, however, homogeneous in atomic composition so that the total cross section $\sigma = \lambda_m^{-1}$ is only a constant for an electron traveling within a specific zone. Therefore, the case of continuous change of atomic composition will not be considered here. A problem in sampling by Eq. (26) occurs when an electron crossing the interface of zones with different σ values. Let T_i denote the segment of electron step length s within the i-th

zone of scattering cross section σ_i, the Eq. (26) can then be simplified to a sum of a discrete sequence, $\sigma_i T_i$, as

$$\sum_i \sigma_i T_i = -\ln R \text{ and } s = \sum_i T_i . \tag{44}$$

This differs from the conventional sampling that the step length is only associated with the scattering cross section at starting location of the flight step. This correction to the step length is expected to be important for specimen containing nanoscale structures so that the electron scattering mean free path, that is, the inverse of scattering cross section, is comparable with or even larger than the structure feature size. Then the question reduces to obtaining the partial distance T_i for an electron flying over the different specimen zone and the corresponding sequential points intersecting at the zone surfaces. The detail of the sampling process is performed by using a ray-tracing technique (Ding & Li, 2005), which will be shown below. Besides the path length sampling, an electron would be refracted at the boundary interface. A treatment of the refraction will also be explained.

2.2.1 CSG modeling

The geometric structure of the specimen should be specified at first before the simulation. By CSG modeling, a complex geometric structure can be constructed with some simple and basic shapes which can be analytically described with a few parameters (Ding & Li, 2005; Li & Ding, 2005). The blocks enclosed by these shapes contain either the different materials or even simply empty ($\sigma = 0$), as illustrated by Fig. 5. For each electron trajectory step, one has to compute the intersecting points with every possible shape. Because a MC simulation requires tracking a large number of electron trajectories, the computation for judging intersecting points is the most time consuming in a simulation. Therefore, the structure construction technique needs to be efficient for the calculation. Here we choose a half-infinite space with flat top surface as the specimen basis on which a complex structure is constructed with some basic shapes. The basic shapes include sphere, ellipsoid, cylinder, cone, cube, tetrahedron, polyhedron, and so forth, which can be easily and analytically defined. Each kind of basic shape may be implemented into a subroutine to allow for the calculation of intersecting points efficiently.

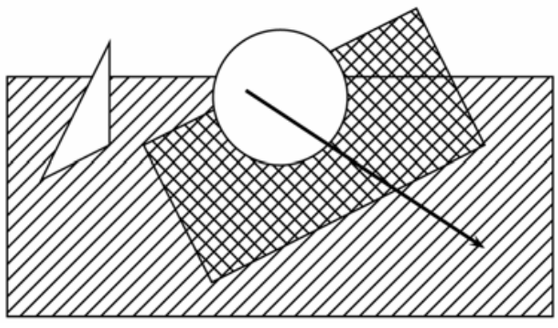

Fig. 5. The sketch of constructing specimen geometric structure by CSG modeling.

It is obvious that, with the limited number of parameters, one cannot in practice build an arbitrary complex structure shape. Fortunately, most of the geometric structures observed with SEM can be modeled by the present algorithm. In particular, the use of empty blocks

enclosed by the basic shapes allows for some special structures to be constructed, for example, porous material. Generally, for each shape used in the construction one has to transform the orientation of the basic shape in a coordinate system fixed with the sample to another one fixed with the shape so that the standard method for solving the simple form is applicable. More detail description of this procedure is given by Li & Ding's work (Li & Ding, 2005).

a. Judging intersecting and sorting

A series of subroutines for determining the intersecting points of a ray with the basic shapes were developed. Because an arbitrary specimen structure is made up of some basic shapes which can be spatially located in any position, we have to judge intersecting points of one electron trajectory step, viewed as a ray, with every basic shapes specified. In this way all the distance T'' pairs can be obtained, where T'' denotes the distance between the starting point and a particular intersecting point, for an electron trajectory intersecting with each shape (one T'' for incoming and another for outgoing) along the electron moving direction of the electron motion. A series of subroutines is used to calculate the T'' pairs for each kind of shape so that the program could be modularized; its advantage is obviously that it is easy to expand of the program when including other newly added basic shape types (Li & Ding, 2005).

Having obtained all the intersecting points and the T'' pairs, we have to calculate the distance T for an electron moving within a particular material block. To obtain the distance between the adjacent intersecting points along the electron path, the right T''-sequence should first be derived. A simple sort subroutine based on Shell-sort (which, as one of the oldest sorting algorithms, is fast and easily implemented) can do this well (Knuth, 1998). A 2-D array is then used to save the Tsequence and the index for the material to label the corresponding scattering cross sections. The correct σ_i is thus determined for the material between the $(i-1)$-th and i-th intersecting points. This procedure is illustrated by Fig. 6.

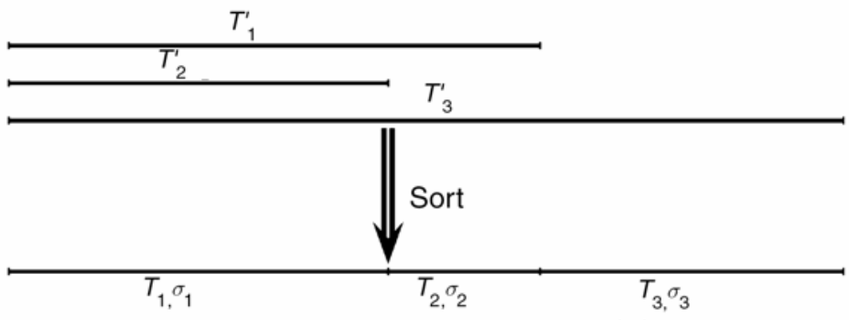

Fig. 6. Schematic diagram for sorting the intersection distances and the corresponding cross sections.

Regarding the efficiency of the above procedure, it is fast for the small number of shapes considered. Of course, one wishes to minimize judging the procedure steps when lots of shapes are involved in the structure building. Ideally, if we could know the order of rays intersecting with the basic shapes, we would only need to obtain the intersecting points in sequence until Eq. (44) was satisfied, so that only several related but not all shapes would be considered in the calculation. However, before obtaining the step length we cannot know the order. The above-mentioned method is one solution to this self-consistent problem.

For a large number of building shapes there are two ways of minimizing the necessary number of shapes involved in each step of the judging procedure. The first method is to construct a tree-shaped structure with which all the neighbors of a particular shape are specified. Then only the neighbors of the shape where an electron step is crossing are considered, from among which one correct shape is chosen and the intersecting points as well as the distance T are calculated. This procedure step continues until Eq. (44) is satisfied. Because in each procedure step we have to consider all the neighbors of the shape varying step by step, the overall computation for electron flight step length may still be inefficient. Another method considers the geometric structure constructed by dividing the whole space into small cubes. Although the neighbor judging is easier, the total computation time is also significantly higher because of the need to count many small cubic blocks.

b. Calculation of path length

An electron flies in the specimen from the old scattering position $\mathbf{x}_0$ to the new position $\mathbf{x}$ over a distance s along the moving direction,

$$\mathbf{x} = \mathbf{x}_0 + \mathbf{v}s \,. \tag{45}$$

The flight path vector $\mathbf{v}s$ is treated as a ray in the judging procedure, where $\mathbf{v}$ is the unit vector of velocity direction. The valid T in $s = \sum_i T_i$ that represents the distances between intersecting points in Eq. (44) must be positive. $T \le 0$ can be excluded by the sorting procedure for obtaining the correct T-sequence.

The procedure for obtaining flight step length by Eq. (44) is as follows. First, a variable C is used to apply a do-loop to calculate

$$C = C + \sigma_i T_i, \qquad i = 1, 2, ..., m_c \tag{46}$$

where m_c is the number of intersecting points. If the condition $C \ge -\ln R$ is satisfied at $i = m$, this means that the electron flight terminal will be a fall in the m-th section. The do-loop should be stopped at m and the step length is then given by

$$s = \sum_{i=1}^{m-1} T_i + \left(-\ln R - \sum_{i=1}^{m-1} \sigma_i T_i \right) \Big/ \sigma_m \,; \tag{47}$$

otherwise, there is no i for the condition being satisfied. This means the step length is longer than $\sum_i T_i$; so some additional conditions should be used to decide s. There are two cases: (1) an electron is moving toward the vacuum, that is, $v_3 < 0$ or $z < 0$ and $v_3 = 0$ and $z = 0$. The electron then escapes from the specimen and we can simply take $s = \sum_{i=1}^{m_c} T_i$. Another subroutine is used to determine whether the electron has enough energy to overcome the surface barrier; (2) an electron is moving toward the basis, that is, $v_3 > 0$ or $z > 0$ and $v_3 = 0$ and $z > 0$. The electron is scattered in the basis, so the step length is

$$s = \sum_{i=1}^{m_c} T_i + \left(-\ln R - \sum_{i=1}^{m_c} \sigma_i T_i \right) \Big/ \sigma_0 \,, \tag{48}$$

where σ_0 denotes scattering cross section of the basis.

2.2.2 Finite element triangle mesh modeling

For a further study of the sample having arbitrary periphery, e.g. a rough surface, which is hard to be described analytically, a finite element triangle mesh, which is frequently used in computer graphics, has been introduced in the complex geometry modeling (Ding & Wang, unpublished; Wang, 2006; Li et al., 2008; Li, 2009). The principle of this method is to approximate a sample surface by using finite triangles. Obviously, more triangles are used more precise description of the sample surface is attainable. A schematic diagram for constructing complex sample geometry is shown in Fig. 7 (a)-(c). The space points are firstly selected to lie on the sample surface. By connecting the neighboring points in a certain order, as shown in Fig. 7 (b)-(c), a finite element triangle mesh for modeling of a sample surface with arbitrary geometry can be obtained. For example, in Fig. 7 (d), a finite element triangle mesh for a helix is shown.

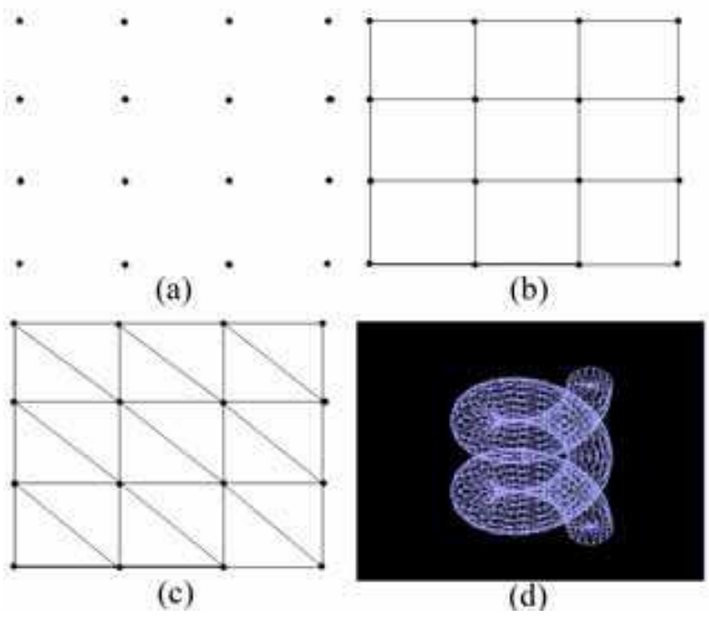

Fig. 7. Schematic diagram for constructing complex sample geometry. (a) Selection of the space points on sample surface. (b),(c) Connection of the neighboring point for obtaining the triangles. (d) The finite element triangle mesh for a helix.

In a MC simulation by using finite element triangle mesh modeling, it is hard to know whether an electron is located in the sample or not just by solving equations like in the CSG modeling. So, a tag should be added to the electron firstly to denote if it is in the sample or not. For example,

$$\xi = \begin{cases} 0, & \text{outside the sample;} \\ 1, & \text{in the sample.} \end{cases} \tag{49}$$

The tag would be changed when the electron trajectory passes through any triangle in the mesh. Judging intersection of the electron trajectory is just like that in CSG modeling. From present spatial location of an electron, a straight line which goes along the electron moving direction, is drawn. The line will encounter triangle(s) and be divided into several segments

by the intersection point, and each section has its tag to denote its position (in or out of the sample). Then a similar step like in CSG modeling can be used to calculate the path length.

a. Space subdivision method

Although the basic algorithm for path length calculation is built, an improvement is still necessary for the simulation because the judging intersection of a trajectory with the triangles is quite time consuming. Here the space subdivision method is developed to accelerate the calculation. The scheme is shown by Fig. 8. After dividing the space into a cubic lattice containing the finite element triangle mesh (Fig. 8(a)), triangle slices lie in some cuboids (Fig. 8(b)). The intersection judging can be performed to be limited to within a subcuboid instead the whole space. To prepare the intersection judging, the statistics of the triangles contained in each subcuboid should be figured out at first. Starting from the present position of an electron, the first subcuboid on its path of the trajectory to be traveled can be detemined, as well as C (Eq. (46)) in the first subcuboid. If $C \geq -\ln R$ is satisfied, the path length is decided by Eq. (47). Otherwise, by using the straight line drawing algorithm (Cleary & Wyvill, 1988), the next subcuboid in the path of the trajectory can be found (Fig. 8(c)), and the same routine as in the first subcuboid is applied. After this do-loop is performed for subcuboids one by one, the path length is finally obtained; otherwise, the electron goes out of the sample.

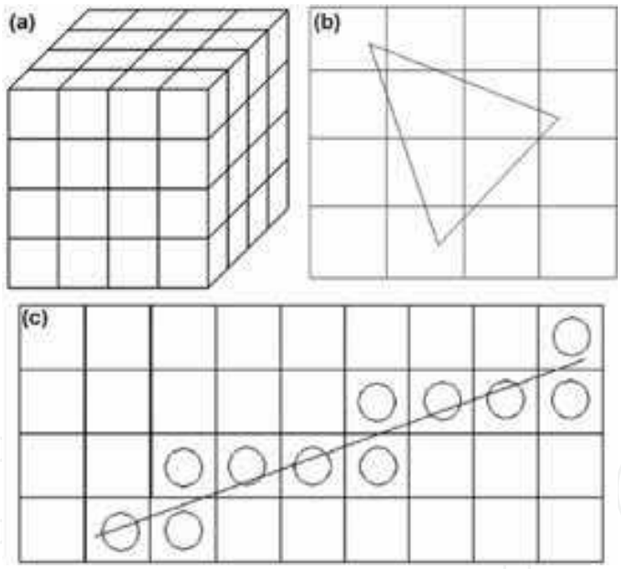

Fig. 8. Schematic diagram for space subdivision method. (a) Dividing space into cuboids. (b) Statistics of triangles lying in each cuboid. (c) Judging the subcuboids in which a trajectory is passed through.

b. Treatment of refraction

When an electron penetrates through a boundary interface, the refraction of electron moving direction should be considered. The refraction at a surface is treated as follows: First, the direction of an electron in the sample coordinate system of axes (x,y,z) is transformed to the new coordinate system of axes (x',y',z') with the z'-axis normal to a triangulated plane (Fig. 9).

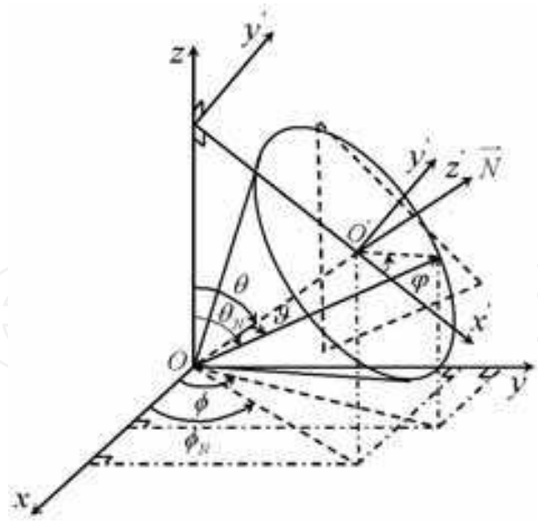

Fig. 9. The schematic diagram of coordinate system transformation for the directional vector $\vec{N}$ of an electron. The old frame of axes (x,y,z) is fixed at the sample, and the new frame of axes (x',y',z') is at a local triangulated plane with the z'-axis normal to the plane. Here, $\vec{N}$ stands for the normal vector of a local triangulated plane that the electron enters into.

The transform relation is,

$$\begin{pmatrix} v_{x'} \\ v_{y'} \\ v_{z'} \end{pmatrix} = \begin{pmatrix} \cos\theta_N \cos\phi_N & \cos\theta_N \sin\phi_N & -\sin\theta_N \\ -\sin\phi_N & \cos\phi_N & 0 \\ \sin\theta_N \cos\phi_N & \sin\theta_N \sin\phi_N & \cos\theta_N \end{pmatrix} \begin{pmatrix} u_x \\ u_y \\ u_z \end{pmatrix}, \tag{50}$$

where $(v_{x'}, v_{y'}, v_{z'}) = (\sin\vartheta\cos\varphi, \sin\vartheta\sin\varphi, \cos\vartheta)$ is the unit vector of velocity in the new frame of axes and $(u_x, u_y, u_z) = (\sin\theta\cos\phi, \sin\theta\sin\phi, \cos\theta)$ in the old frame of axes. θ_N and ϕ_N are the polar and azimuthal angles of the normal vector $\vec{N}$ of the local triangulated plane, respectively. Second, when an electron escapes from solid into the vacuum a quantum mechanical transmission coefficient (Cohen-Tannoudji et al., 1977), i.e. Eq. (42), is applied to the electron fate as being absorbed or emitted.

Third, the direction of electron will be changed according to the refraction law, $\sqrt{E_1}\sin\vartheta_1 = \sqrt{E_2}\sin\vartheta_2$, where E_1 and E_2 are the electron energies inside and outside the solid, respectively; ϑ_1 and ϑ_2 are the polar angles of the unit vector inside and outside the solid, respectively. Because the electron kinetic energy inside a material is referenced to the top of conduction band, the energy changes by the inner potential when an electron passes though a surface/vacuum interface, i.e. $E_2 = E_1 - U_0$, where U_0 is defined in Eq. (38). Thus, the unit vector is changed as, $(v'_{x'}, v'_{y'}, v'_{z'}) = \left(v_{x'}S, v_{y'}S, v_{z'}\sqrt{1 - S^2(1 - v_{z'}^2)}\right)$, where $S = \sqrt{E_2/E_1}$. When the polar angle ϑ_1 is larger than the critical angle, $\vartheta_C = \sin^{-1}\sqrt{1 - U_0/E_1}$, the electron may be reflected by the surface, $(v'_{x'}, v'_{y'}, v'_{z'}) = (v_{x'}, v_{y'}, -v_{z'})$. Fourth, an inverse transformation to the old frame of axes should be done after changing the direction by refraction,

$$\begin{pmatrix} u'_x \\ u'_y \\ u'_z \end{pmatrix} = \begin{pmatrix} \cos\theta_N \cos\phi_N & -\sin\phi_N & \sin\theta_N \cos\phi_N \\ \cos\theta_N \sin\phi_N & \cos\phi_N & \sin\theta_N \sin\phi_N \\ -\sin\theta_N & 0 & \cos\theta_N \end{pmatrix} \begin{pmatrix} v'_{x'} \\ v'_{y'} \\ v'_{z'} \end{pmatrix}. \quad (51)$$

3. Simulation of CD-SEM images for critical dimension nanometrology

In integrated circuit industry, new material and new device structures will probably allow MOS devices to remain competitive near-term years in spite of Moore's Law. Metrology of the electronic material and devices is crucial to the research and development of future semiconductor industry. Especially, the most fundamental one is that of dimension metrology, such as critical dimension (CD) and film thickness (Vogel, 2007). According to the International Technology Roadmap for Semiconductors (ITRS, 2007), the dimension of transistor gates has been decreased to about 30 nm with the accuracy lower than 1 nm by 2007. Thus, strict dimension control is an extremely urgent task in near-term years.

Many measurement methods are being developed to meet the case, such as, scatterometry, atomic force microscopy, transmission electron microscopy and SEM (Maeda et al., 2008). Among them, SEM is widely used as a standard tool for the linewidth measurement and CD metrology for its high resolution and high efficiency. A specialized length measuring instrument named critical dimension scanning electron microscope (CD-SEM) has thus been developed and widely used for the dimension metrology (Wang et al., 2007). The top-down mode in CD-SEM is mostly employed inline or offline for it is a nondestructive and great throughput examination.

However, there still remains a problem in accurate dimension metrology and linewidth measurement because of the edge effect in SE images. The edge effect can induce an important feature in SE line-scans, the bloom, which gives rise to the contrast that distinguishes the edge from the rest of the sample. The finite width of the bloom may lead to tens of nanometers of ambiguity in the edge position (Villarrubia et al., 2004; Tanaka et al., 2007). Moreover, the extent of the edge effect is the feature size dependent. When the line/feature size is decreased to several tens nanometers, the bias due to the edge effect would become more obvious. A lot of works including both experimental study (Bunday et al., 2007; Choi et al., 2006; Jones et al., 2003; Kawada et al., 2003; Maeda et al., 2008; Matsumoto et al., 2006; Morokuma et al., 2004; Novikov et al., 2007; Rice et al., 2006; Shishido et al., 2002; Tanaka et al., 2003; Tanaka et al., 2004; Tanaka et al., 2005; Tanaka et al., 2007; Tanaka et al., 2008a; Tanaka et al., 2008b; Wang et al., 2007; Yamane & Hirano, 2005) and theoretical investigation (Abe et al., 2007; Babin et al., 2008a; Babin et al., 2008b; Bunday & Allgair, 2006; Dersch et al., 2005; Frase & Hαβler-Grohne, 2005; Frase et al., 2007a; Frase et al., 2007b; Gorelikov et al., 2005; Villarrubia et al., 2004; Villarrubia et al., 2005a; Villarrubia et al., 2005b) with MC simulation methods have been done, aiming at accurate estimation of the CD values with CD-SEM. However, when the dimension decreases to tens nanometers most of the experiential methods, such as, the maximum derivative method, the regression to baseline method and the sigmoidal fit method, face different difficulties (ITRS, 2007; Villarrubia et al., 2005a). A reasonable algorithm is urgently needed for the linewidth metrology of nanometer systems. Several algorithms (Bunday & Allgair, 2006; Frase & Hαβler-Grohne, 2005; Frase et al., 2007a; Morokuma et al., 2004; Novikov et al., 2007; Shishido et al., 2002; Tanaka et al., 2003; Villarrubia et al., 2004; Villarrubia et al., 2005a; Villarrubia et al., 2005b) by MC methods for CD linewidth determination have been brought up to meet the limitation of the traditional experiential algorithms.

Recently, several new algorithms have been published. Novikov et al. (Novikov et al., 2007) have described a method for linear measurement in the nanometer range by taking into account the relationship between the specific probe positions and the SEM signal sharp kink points. The method is quite simple and suitable for large linewidth and sidewall angle; but, it would have large error when linewidth and/or sidewall angle are small because the kink points can not be distinguished clearly in these cases. Frase et al. have presented an exponential distribution operators method (Frase & Hαβler-Grohne, 2005; Frase et al., 2007a) with which the SEM intensity profile is modeled by a piecewise-defined continuous function that approximates to the measured intensity profile extracted from an image by means of a least-squares fit. The algorithm is tested by a series of MC simulations which fit well with the simulation results for large dimensions (>100 nm) and large sidewall angles (not close to vertical). However, the error will be large also for smaller dimensions and sidewall angles. Tanaka et al. have developed a multiple parameter profile characterization algorithm (Morokuma et al., 2004; Shishido et al., 2002; Tanaka et al., 2003) based on MC simulated and experimental results, which partitions the SEM image signal into the sidewall and footing based on the first deviation of the measured signal level. It applies to top-down SEM images and no throughput loss will be incurred; it is shown to have a 3-sigma accuracy of ±0.9° for sidewall angle deviating by more than 2°. The limit of the algorithm is the effective range of the sidewall angle estimation, and, the error will also increase when the linewidth is reduced. Villarrubia et al. have introduced a model-based library (MBL) method (Villarrubia et al., 2004; Villarrubia et al., 2005a; Villarrubia et al., 2005b) by which a library of the MC simulation results for various parameters spanning the process space of interest is constructed. Dmitry et al. have also used an off-line generated MC simulation library and fitted the measured intensity profiles of the critical shape metrology (Gorelikov et al., 2005). In principle, this library method would be the most accurate one for it can directly relate the measured signal profiles with the modeled geometry. However, it would need to put huge effort in order to obtain such a calculation library for lots of different experimental parameters, and it is difficult to differentiate cases with the similar shape of SE line-scan profiles.

Frase et al. have recently reviewed the fundamentals, special performance features and applications of existing SEM image contrast simulation packages based on MC methods (Frase et al., 2009). It is considered that the MBL method should be the most accurate algorithm for its sound physical foundation and one-to-one relationship between the image intensity profile and the geometry models (Villarrubia et al., 2005a). The model-based method by using a MC simulation has been proved to be an excellent approach to determine specimen geometric parameters by comparing the measured SEM image data directly with the model input data for calculation. For this purpose we have to deal with three elements involved in a simulation, i.e. the sophisticated physical model, the universal geometric structure model and efficient simulation algorithm. For SEM imaging simulation the physical modeling of SE signal generation in different materials plays a critical role. The influence of different MC models to the linwidth determination has been carefully carried out recently (Villarrubia & Ding, 2009). For a geometric structure modeling of a realistic trapezoidal line shape, many parameters should be taken into account, such as, width, height, foot/corner rounding, sidewall angle and roughness, etc. Apart from these, other influencing factors, such as electron beam condition (primary energy, probe size and incidence angle), material properties (composition and distribution), SE signal detection (detector properties and electric field) and others (charging effects, noise and etc.) should be

considered to meet the accurate linewidth control (Frase & Hαβler-Grohne, 2005). In order to build such a library an efficient simulation program should be constructed in order to save calculation time for a mass of practical conditions.

Among them, however, the influence of the side wall roughness, the line edge roughness (LER) or the line width roughness (LWR), to CDs has rarely been included in a theoretical calculation because of the complexity of constructing a reasonable rough surface model. The LER or the LWR can degrade resolution and linewidth accuracy (Yoshimura et al., 1993) and cause fluctuation of transistor performance (Asenov et al., 2003; Croon et al., 2002; Diaz et al., 2001; Ercken et al., 2002; Hamadeh et al., 2006; Kaya et al., 2001; Kim et al., 2004a; Kim et al., 2004b; Linton et al., 1999; Linton et al., 2002; Oldiges et al., 2000; Xiong & Bokor, 2002; Xiong & Bokor, 2004; Xiong et al., 2004; Yamaguchi et al., 2003; Yamaguchi et al., 2004). It becomes a critical issue when the CDs for semiconductor devices shrink into few tens nanometers (ITRS, 2007; Gwyn et al., 2003) because the roughness on the edge of the line does not scale with the linewidth (Asenov et al., 2003). Though many efforts have been done to estimate LER/LWR with top-view SEM images (Braun, 2005; Foucher et al., 2006) and especially by comparing with CD-AFM (Foucher et al., 2006), their dependence on different CD-SEM experimental conditions is still not quite clear because the roughness is a complex parameter to metrology. But, on the other side, in a MC simulation one can in principle construct a rough surface structure model with exact defined values of roughness parameters. The image contrast simulation enables us to establish a relation of SEM image contrast with structure model directly; such a relationship can be used for a quantitative estimation of the influence of roughness on the linewidth measurement. For this purpose we shall introduce a universal rough edge structure modeling into a MC simulation for the first time.

In this section, a MC simulation program for modeling of linewidth measurement has been developed to solve these problems (Ding & Shimizu, 1996; Ding & Li, 2005; Ding & Wang, unpublished; Li & Ding, 2005; Li et al., 2008; Mao et al., 2008; Shimizu & Ding, 1992; Yue et al., 2005). The main topic here is to apply the MC method to investigate in detail the influence of various factors to the contrast of SEM line-scan and image. The study gives a further insight into the new algorithm for CD metrology/linewidth determination. This MC simulation is mainly based on the up-to-date electron scattering model (Shimizu & Ding, 1992; Ding & Shimizu, 1996; Mao et al., 2008), a universal geometric structure model (Ding & Li, 2005; Ding & Wang, unpublished; Li & Ding, 2005; Li et al., 2008; Yue et al., 2005) and the message passing interface (MPI) program with accelerated algorithm (Ding & Wang, unpublished; Li et al., 2008), as mentioned in Sec. 2 and the following. A systematic calculation for different parameters has been done, advancing a step towards building a MBL library.

3.1 Simulation method and surface roughness model

Villarrubia and Ding (Villarrubia & Ding, 2009) have compared eight MC physical models based on phenomenological fitting measured parameters, a binary scattering model and a dielectric function approach. They concluded that, CD linewidths estimated by these models agree to each other within ±2.0 nm on silicon and ±2.6 nm on copper in 95% of comparisons with electron landing energy, beam width, and other parameters typical of those used in industrial CD measurements. In Ref. (Frase et al., 2009), Frase et al. also reviewed the physics of probe-sample interaction and modeling, and existing MC simulation programs. Both of them found that, the MC model based on the Mott's cross-section for elastic

scattering and a dielectric function approach for inelastic scattering would achieve the most agreeable result comparing with experiment. Furthermore, this MC model enables a more detailed treatment of the various physical processes involved, such as, the cascade SE generation.

In this respect, the MC model (Li et al., 2008) used here for SEM image simulation has been improved as shown in Sec. 2. Additionally, a rough surface geometry model is introduced to construct the sample surface, together with using of a ray-tracing technique (Li & Ding, 2005) in the calculation procedure of electron step length. Appropriate boundary correction (Yue et al., 2005) had also been considered in order to treat the reflection/refraction of low energy SEs when they pass through an interface separating different materials.

3.1.1 Electron scattering model

The MC simulation of electron scattering process bases on the tracing of incident electron trajectories made of joining of randomly sampled electron scattering events as well as that of generated SE (Ding & Shimizu, 1996; Shimizu & Ding, 1992). For the treatment of electron elastic scattering (also can be found in Section2), the Mott's cross section (Mott, 1929) with the Thomas-Fermi-Dirac atomic potential (Bonham & Strand, 1963) is employed. As for electron inelastic scattering, we use a dielectric function formalism which handles as well the SE production in an electron inelastic scattering event. The FPA has been used in this work to calculate energy loss function (Mao et al., 2008), without introducing SPA (Ding & Shimizu, 1996; Penn, 1987). The compiled experimental data on the optical constants (Palik, 1991) were used. Secondary electron excitation process is divided into two individual parts in the calculation (Mao et al., 2008), i.e. the single electron excitation and the excitation via plasmon decay in different areas of the momentum transfer- and energy loss-plane. This consideration has been proven to be more exact than the previous model (Ding & Shimizu, 1996) in deriving secondary electron energy distribution particularly for those materials that having a strong and sharp plasmon energy loss peak in its optical energy loss function, such as, Si and Al.

As pointed out by Villarrubia & Ding (Villarrubia & Ding, 2009), the physical model itself could introduce error more or less, in spite of using the most sounded physics. Here, in order to stand out the influence of other factors to the CDs, we would neglect the uncertain error due to the physical model here.

3.1.2 Sample structure construction

Modeling of 3D structures is the basic factor in contemporary CD metrology, thus, different kinds of modeling have been introduced (Frase et al., 2009). The reasonability for illustration of 3D specimen structures and the optimization of simulation are certainly the two most aspects for a 3D geometric structure model.

The geometric structure used in this simulation is mainly based on our primary works (Ding & Li, 2005; Ding & Wang, unpublished; Li & Ding, 2005; Li et al., 2008; Yue et al., 2005), as illustrated in Sec. 2. For describing a geometrical structure, two main approaches have been applied; one is the CSG (Ding & Li, 2005; Li & Ding, 2005; Yue et al., 2005) and the other uses a finite element triangle mesh to approximate the sample surface (Ding & Wang, unpublished; Li et al., 2008). Furthermore, for the surface roughness structure, the finite element triangle mesh model is very suitable to simulate the line edge roughness of the wafer gate. The surface roughness can be parameterized by the amplitude 3σ and the density described by the interval a of rough peaks.

A Gaussian function is a good approximation for characterization of gate length fluctuation or linewidth roughness (Bunday et al., 2004; Kim et al., 2004a; Xiong et al., 2004) and is usually used to model the rough effects. Therefore, here we represent the random surface roughness by introducing two parameters: the 3σ deviation of a Gaussian function describes the amplitude fluctuation of rough peaks, and, the mesh interval, a, describes the density of rough peaks. By varying the two parameters we can obtain a variety of rough surfaces or rough edges. Specific sampling of vertical coordinate above the plane, z, which satisfies the statistical distribution,

$$f(z) = \frac{1}{\sqrt{2\pi}\sigma} \exp\left(-z^2/2\sigma^2\right), \tag{52}$$

for each grid point is firstly made at a finite element square mesh whose lattice constant is a. Each square is then divided into two triangles so that the grid is in fact a triangulated mesh; by joining mesh points a 3D geometric structure of random peaks and valleys, each one is in a hexagon form that having six side surfaces, is constructed. Because now the surface is not as that defined by a simple condition $z = 0$ for a smooth plane, we have to deal with the local surface plane in order to determine electron incidence/emission location. The reason to use a triangulated mesh is due to its advantage on easy judging the intersection of a velocity vector with a local triangulated plane when considering an electron incidence into the surface or emission from the surface (Ding & Li, 2005). A smooth plane surface can be constructed similarly by simply setting the vanishing amplitude. For the side surface of a line, it's also easy to construct a rough surface firstly on a virtual plane $z = 0$ and then transform this plane with the mesh grid points into a declining side with the side wall angle α. Fig. 10 shows the schematic diagram of a rough surface construction. Fig. 11 is an example of mesh building of a rough line, where each surface is roughness modulated.

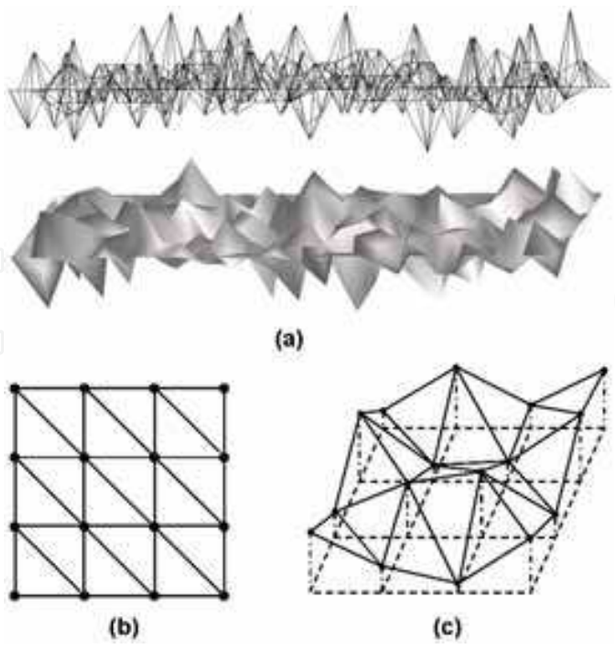

Fig. 10. (a) The schematic diagram of the roughness amplitude constructing by using triangulated meshes; (b) the triangulated mesh; (c) the local rough peaks constructed.

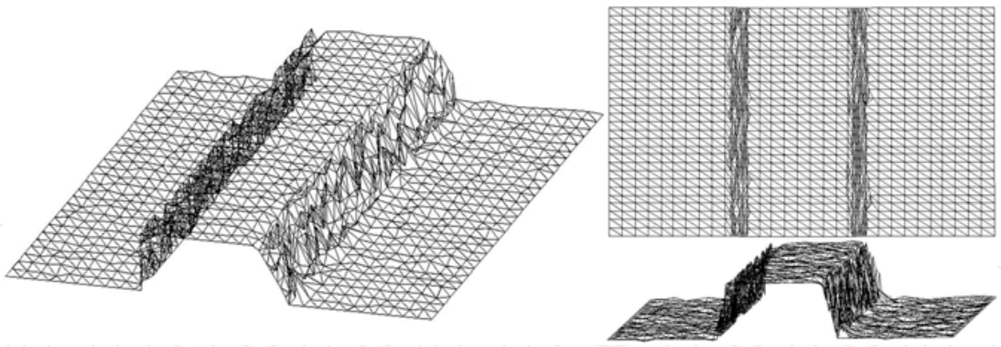

Fig. 11. Example rough surface structure of a trapezoidal line constructed with a triangulated mesh.

For the smooth structure, we can use two different constructive methods: first, the CSG modeling as well as a ray-tracing technique for SEM images for an inhomogeneous specimen with a complex geometric structure. Second, we can also construct the smooth geometry structure by using finite element triangle mesh while setting $\sigma = 0$.
Therefore, the geometric structure for a trapezoidal line with or without corner rounding, whose cross-sectional profile is shown in Fig. 12, is described by following parameters: the height H, the upside width W, the side wall angle α and the corner radiuses r_U, r_D. The surface roughness can be parameterized by the amplitude 3σ and the density described by the interval a of rough peaks. Using the parameter set, $(H, W, \alpha, r_U, r_D \sigma, a)$, the linewidth can be easily described by the top-CD, (such as, $W_T = W$), and the bottom-CD, (such as, $W_B = W + 2\tan\alpha$), as usual for the CD metrology of the gate lines.

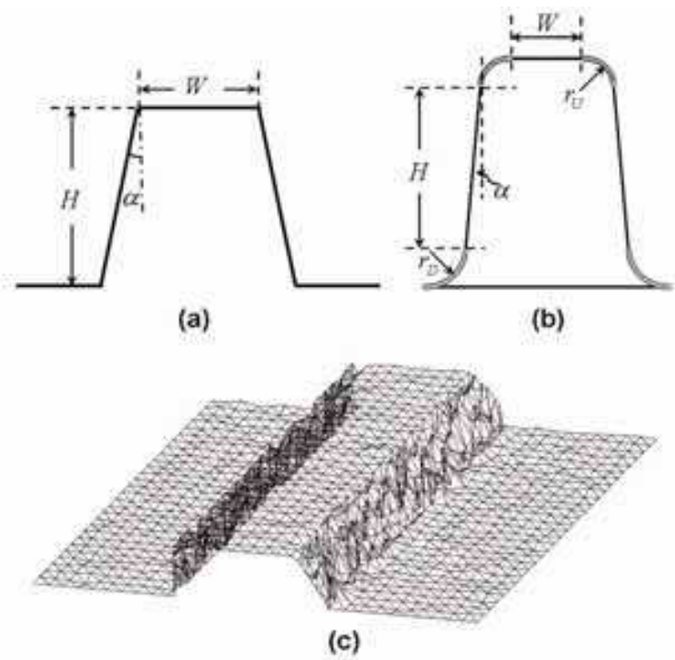

Fig. 12. The schematic diagram of specifying parameters of: (a) a trapezoidal line with smooth surface; (b) a trapezoidal line with corners and smooth surface; (c) a trapezoidal line with rough surface.

3.1.3 Computational conditions

The image pixels are set as 225×300 or 220×500 at an interval of 0.5-1.0 nm; for each pixel a number of 10^3 incident electron trajectories and several tens times of secondary electron trajectories are traced. To simplify the simulation the beam diameter is firstly assumed to be infinitely small; a more realistic image for finite probe size can be further obtained by a convolution procedure with a Gaussian probe width distribution. In the presented results we have not taken account of angular information of SE signals and also ignored any effect due to a detector and electric filed in vacuum chamber, i.e. all the emitted electrons from the surface whose kinetic energy are smaller than 50 eV are taken as SE signals. A parallel computer is used to perform the calculation with a MPI program. The high efficency of the program can be considered for the most complex case of surface roughness structures: The memory required is $O(N)$, i.e. proportional to the number of the rough surface peaks, N. The CPU time can be reduced from $O(N)$ to $O\left(N^{1/3}\right)$ by introducing the spatial subdividing technique. For example, only a few minutes are necessary for a linescan and several hours for an image when using about 100 CPUs on a parallel computer.

3.2 Model validation

To verify the current MC simulation model, we have compared the simulated SE yield, the SE energy spectra and more directly the SEM line-scan and images with experimental results. The SE yield and energy spectra are fairly important to the SEM image simulation for it implicates the interaction mechanism of electrons with a solid. In our previous studies reasonable values of secondary yield and satisfactory energy distribution curves (Mao et al., 2008) as well as backscattering energy spectra (Ding et al., 2001; Ding et al., 2004b) have been successfully obtained, which has proved the reasonability of this MC model. For Si considered here, by using the full-Penn algorithm instead of single-pole approximation for the energy loss and considering more accurate SE excitation process, a good agreement had been obtained for absolute SE yield (Joy, 1995) and the SE spectrum (Joy et al., 2004) with experimental ones (Fig. 13).

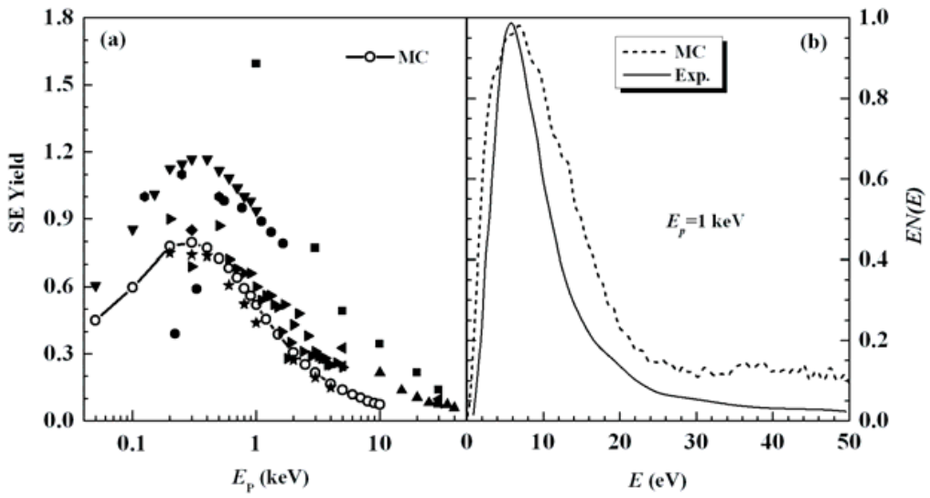

Fig. 13. Comparison on (a) the SE yield and (b) the SE energy spectra between experimental measurements and the calculations for Si. Experimental data are represented by solid symbols in (a) (Joy, 1995) and solid line in (b) (Joy et al., 2004).

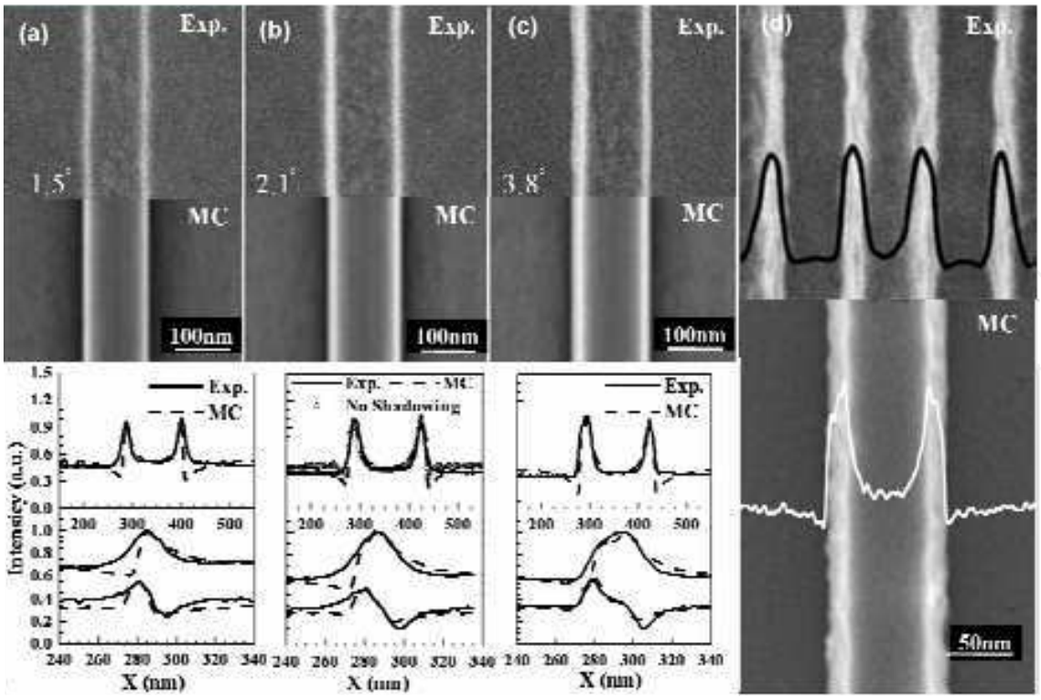

Fig. 14. A comparison on the SE line-scans and images between experimental results (Kawada et al., 2003; Shishido et al., 2002; Tanaka et al., 2003) and calculation. The input parameters in MC simulation are: (a) $H = 240$ nm, $W = 120$ nm, $\alpha = -1.5^\circ$; (b) $H = 240$ nm, $W = 120$ nm, $\alpha = 2.1^\circ$; (c) $H = 240$ nm, $W = 120$ nm, $\alpha = 3.8^\circ$ for left side and $\alpha = 2.1^\circ$ for right side; (d) $H = 150$ nm, $W = 65$ nm, $\alpha = 5^\circ$; $3\sigma = 6$ nm, $a = 10$ nm for rough sides; $3\sigma = 1.5$ nm, $a = 2$ nm for rough top and substrate surfaces. The beam diameter for convolution is 8 nm for (a), (b) and (c), and 3 nm for (d). The primary energy of the electron beam is 0.8 keV for (a), (b) and (c), and 1 keV for (d).

Fig. 14 presents directly a comparison on SEM line-scans and images for smooth geometry lines between the simulation results for different parameters (sidewall angle and roughness) with experiments (Kawada et al., 2003; Shishido et al., 2002; Tanaka et al., 2003). The consistence found is reasonably well in different cases. The minor difference is that the simulated intensity drops at the edges of the line by the shadowing effect but in an experimental image this effect is vanished because of the existence of small external electric field. Fig. 14(b) indicates that, whether this shadowing effect is included or excluded dose not influence the linewidth. We can further deal with line edge roughness (LER) or line width roughness (LWR) as mentioned in Ref. (Li et al., 2008). It can be seen that the present MC simulated line scanning profile of a rough edge agrees qualitatively well with the experimental observation by choosing suitable parameters, indicating that the rough surface model introduced here is quite reasonable. One can thus estimate the actual roughness values of the observed system by comparing the simulated images with the experimental ones. The gate line segment distribution obeys Gaussian function with a standard deviation of line edge fluctuation (Bunday et al., 2004; Kim et al., 2004a; Xiong et al., 2004). Fig. 15 shows that, by a statistics made for the above example calculation of line scanning profile for a 65 nm gate line, a predicted Gaussian distribution of the linewidth has been indeed obtained. This fact also demonstrates that the rough surface model introduced here is very

reasonable. Here, the gate length is decided by only considering the two blooms of the line without introducing any experiential arithmetic because the usual arithmetic is questionable at nanoscale (Villarrubia et al., 2005a). It can be seen that the most probable value of the linewidth is a little bit (~1 nm) smaller than the actual geometry, which should be due to the inherent SEM image contrast formation. Hence, we can investigate the influence of each factor individually. Such a study will lead to an insight into building an applicable algorithm, perhaps the MBL method, for measuring linewidth.

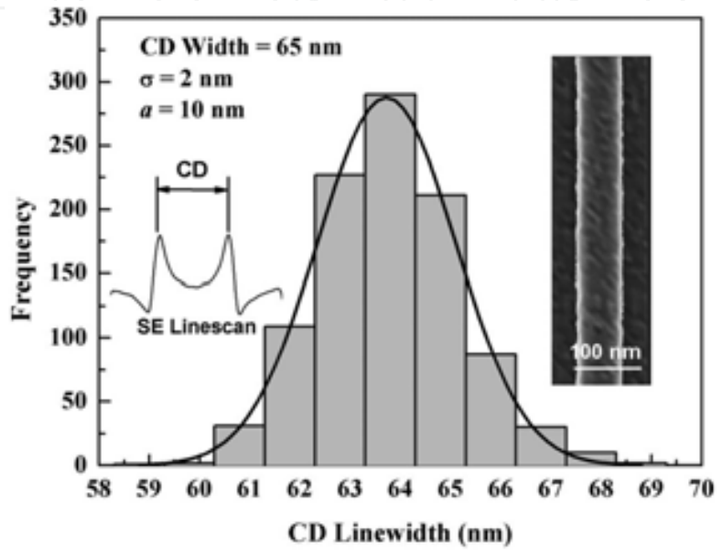

Fig. 15. The simulated gate line segment distribution of a rectangular Si line with the input geometry parameters: $H = 150$ nm, $W = 65$ nm, $\alpha = 0^{o}$, $3\sigma = 6$ nm and $a = 10$ nm. The primary energy of the electron beam is 1 keV.

3.3 Influences of structural parameters to CDs

The precision of CD-SEM requiring optimum operation conditions with respect to stability, achievable resolution, signal-to-noise ratio and choice of primary energy (Frase et al., 2009). To clarify these conditions, in the following, we present the simulated line-scans of silicon lines and discuss the effect of each parameter one by one; they are electron beam parameters (energy, probe size and incidence angle) and geometry parameters (width, height, foot/corner rounding, sidewall angle and roughness).

The beam parameters are important factors to linewidth measurement. Probe energy, size, shape, current, incident angle and so forth can affect SE intensity and SEM contrast though different ways. Electron beam at low energies, E_0 ~ 300-3000 eV, is usually used in practice for it offers some important advantages to CD metrology by the following reasons (Cazaux, 2005): First, the low energy electron beam penetrates only into a thin surface layer in the specimen, thus reducing radiation damage and increasing the surface sensitivity of the imaging process. Second, the sharpness of images governed by topographic contrast can be increased for the extent of the edge effect decrease when the beam energy is low (Joy & Joy, 1996). Third, the SE yield is higher at low energies and, hence, the better signal-to-noise ratio at a given beam current and dwell time per pixel. To illustrate the influence of the beam energy to CDs in detail, the line-scans of a Si gate line at different beam energies are given in Fig. 16. The contrast increases with the energy. However, a little change on line-scan shape

has been found due to the change of interaction volume with primary energy. The CDs are found nearly the same for different beam energies. Thus, the beam energy factor influences the contrast and line-scan shape but none to CD.

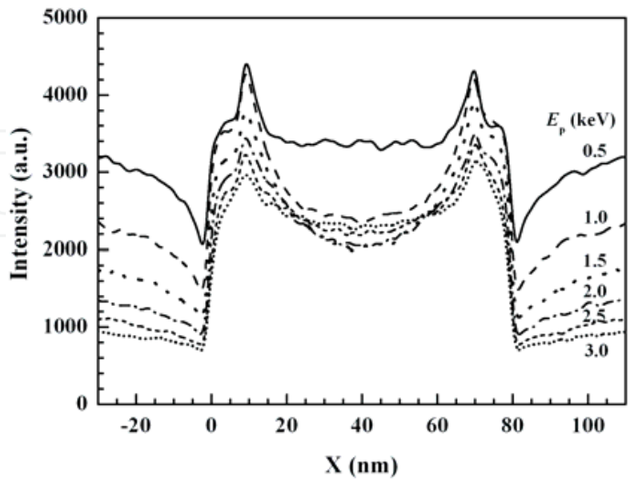

Fig. 16. The simulated SE line-scans of a Si line at different beam energies. The input parameters in MC simulation are: $H = 150$ nm, $W = 65$ nm, $\alpha = 3.8^\circ$, the beam size is 5 nm of FWHM.

The probe size and shape which describe the cross-sectional distribution of incident electrons can influence CDs dramatically. In SEM, the lateral resolution is also governed by the probe diameter (Bronsgeest et al., 2008; Cazaux, 2005), which broadens the real dimension of the edges of a line. Probe size and current are interrelated (Bronsgeest et al., 2008), thus, the resolution in practice is limited (e.g., about 3 nm in low energy region and less than 1 nm in much high energy region). To clarify the extent of influence of limited probe size to CDs, the line-scans of a Si gate line with different probe sizes are shown in Fig. 17.

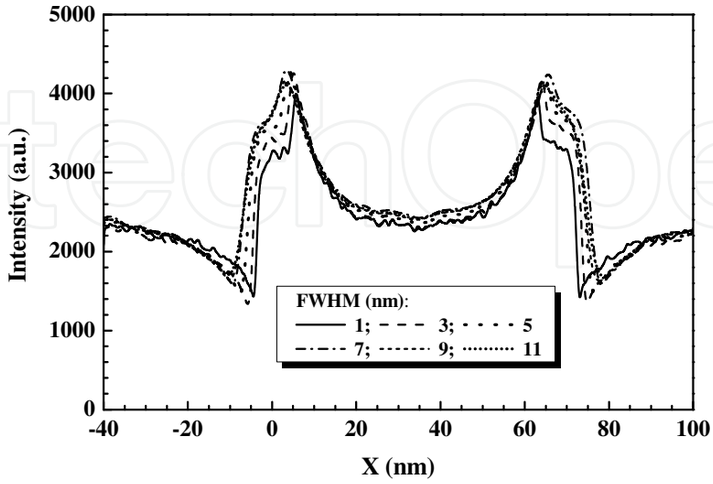

Fig. 17. The simulated CD-SEM line-scans of a single edge of a Si line with different beam sizes. The input parameters in MC simulation are: $H = 150$ nm, $W = 65$ nm, $\alpha = 3.8^\circ$. The primary energy of the electron beam is 1 keV.

The CDs increase gradually with the probe size. The bias of CDs caused by probe size can be estimated from this relation if the probe size is known. Here, the shape or the intensity profile of a probe is considered as a Gaussian distribution approximately for thermionic, Schottky and cold field emitters (Bronsgeest et al., 2008). However, it has been pointed that some critical beam shape dependencies that are not correctly account for by the simple Gaussian model (Tanaka et al., 2005), and that the effect of electron incident angle is not negligible; the electron distribution far from focus is not consistent with a Gaussian model at the impact position of electrons on a line by the effect of aberrations of the beam shape. The requirement of the accuracy and stability of measurement in CD-SEM needs a better beam shape model (Tanaka et al., 2006).

The feature of a modeled line can be characterized by several pattern parameters. By considering the relationship of the simulated SE line-scan/image of modeled line with the experimental one, the pattern-dependent errors of linwidths could be removed. We have studied systematically different kinds of these pattern parameters, such as, width, height, foot/corner rounding, sidewall angle and roughness, and have discussed the influences to linewidth measurement quantitatively. In order to consider the contributions of different parameters, the beam conditions are kept the same in different cases as, the incident energy is 1 keV and the beam size is 5 nm of FWHM.

As shown in Fig. 18, when the width of the line is larger than 20 nm the SE line-scans look quite similar. However, when the width is smaller than the effective attenuation length the signal intensity will increase because of the edge effect. When the sidewall angle is not equal to zero, the model linewidth increases with the height; the line-scan edge shape and the distance between two blooms or two valleys can change dramatically. However, the height of the line does not influence the linewidth directly (Fig. 19).

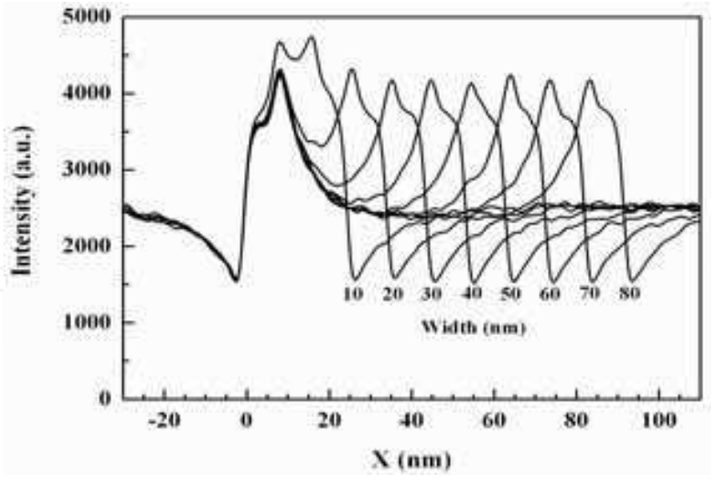

Fig. 18. The simulated CD-SEM line-scans for different widths of a Si line. The input parameters in MC simulation are: $H = 100$ nm, $\alpha = 5^{\circ}$. The primary energy of the electron beam is 1 keV, the beam size is 5 nm of FWHM.

The reason for the negligible effect of width and the height on linewidth can be explained as follows (Reimer, 1998): the SE emission intensity at an edge obeys inverse cosine law as, $1/\cos\theta$, where θ is a sidewall angle. Thus the CDs do not change with the width and height because the SE yield is the same on the edge surface where θ is a constant.

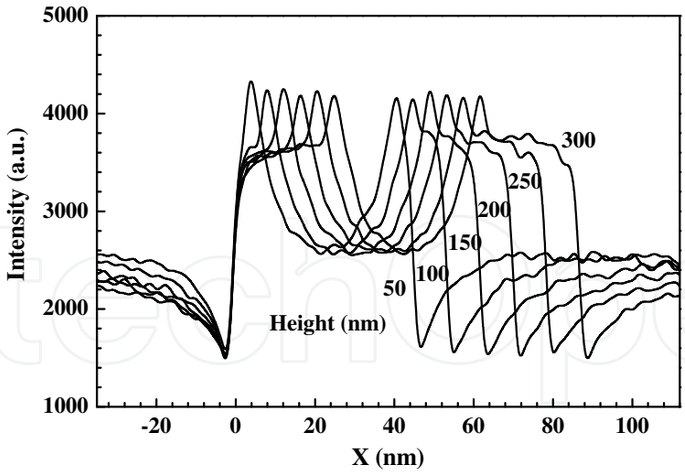

Fig. 19. The simulated CD-SEM line-scans of a single edge for different heights of a Si line. The input parameters in MC simulation are: $W = 40$ nm, $\alpha = 5^\circ$. The primary energy of the electron beam is 1 keV, the beam size is 5 nm of FWHM.

The line-scan shape at an edge is very sensitive to the sidewall angle. Thus, the sidewall angle is a critical factor to the linewidth measurement. To illustrate the dependence of linewidth on sidewall angle, the line-scans and also the bias between the simulation and model are shown in Fig. 20 where the sidewall angle is varied from 0° to 9°. The linewidth increases slightly with the sidewall angle increasing. The tendency is the same as the experimental results (Tanaka et al., 2003).

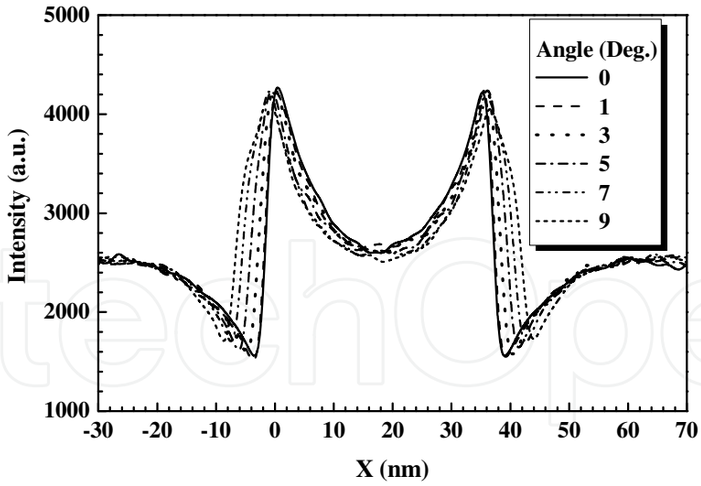

Fig. 20. The simulated CD-SEM line-scans for with different sidewall angles of a Si line. The sidewall angle index is defined in figure 9. The input parameters in MC simulation are: $H = 40$ nm, $W = 40$ nm. The primary energy of the electron beam is 1 keV, the beam size is 5 nm of FWHM.

More generally, the line-scan shape is also sensitive to other angular features, such as, the footing and the corner angle indexes. The rounding feature of a line is usually represented quantitatively by the sidewall angle, the footing and the corner indexes (as shown in Fig. 21)

in practice (Morokuma et al., 2004). These two indexes can be defined based on the first derivative of the measured signal level, that is, the distances between peaks and outer zeroes of the first derivative are calculated as the feature indexes. As can be found in Figs. 22 and 23, both of the footing index and corner index are increasing with the bottom and top radius. The difference between them is mainly because a part of influence of sidewall angle index has been included in the corner index. The sidewall angle index and the corner index have the similar effect on the form of line-scans.

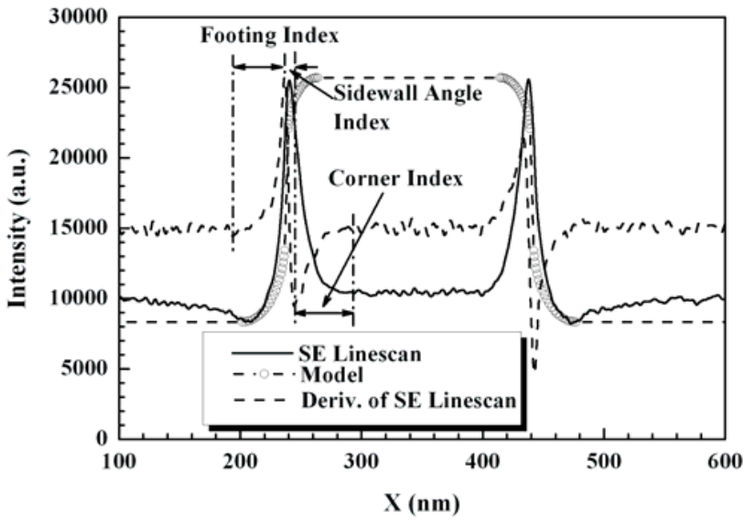

Fig. 21. The sketch for the definition of footing and the corner indexes of the linescan for a trapezoidal line with corner rounding as shown in Fig. 12(b).

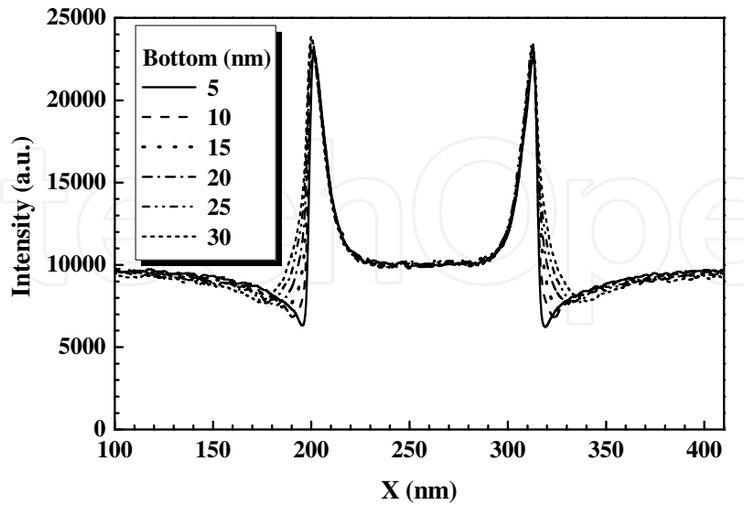

Fig. 22. The simulated CD-SEM line-scans of the lines with different bottom corner radius of a Si line. The input parameters in MC simulation are: $H = 100$ nm, $W = 40$ nm, $\alpha = 0^{\circ}$, $r_U = 10$ nm . The primary energy of the electron beam is 1 keV, the beam size is 5 nm of FWHM.

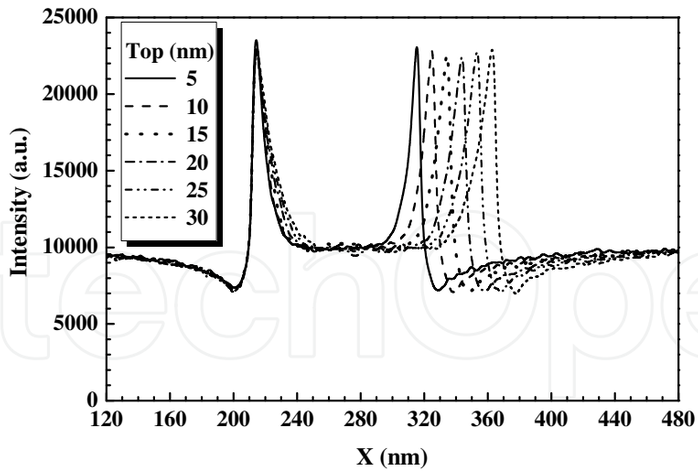

Fig. 23. The simulated CD-SEM line-scans of the lines for different top corner radius of a Si line. The input parameters in MC simulation are: $H = 100$ nm, $W = 40$ nm, $\alpha = 0^{\circ}$, $r_D = 15$ nm . The primary energy of the electron beam is 1 keV, the beam size is 5 nm of FWHM.

The LER and LWR have become a critical issue when the CDs for semiconductor devices shrink into a few tens of nanometers because it can degrade resolution and linewidth accuracy and cause fluctuation of transistor performance. A lot of experimental and theoretical researches have been done to confront this problem (Braun, 2005; Foucher et al., 2006).

In Figs. 24(a)-(e) and Figs. 25(a)-(e), the calculated CD-SEM images of 40 nm width lines are shown for different roughness amplitudes and densities, respectively. When the amplitude 3σ increases from zero to 9 nm the line edge roughness of SEM images becomes obviously and the bias of the linewidth is also increased. However, the line edge roughness changes only slightly when the density decreases from 1/2 to 1/9 nm^{-1}. The bias due to LER/LWR can be up to more than 10% for tens-nanometer linewidth. Indeed, it can become one of the main contributions to the bias of CDs in the future (ITRS, 2007).

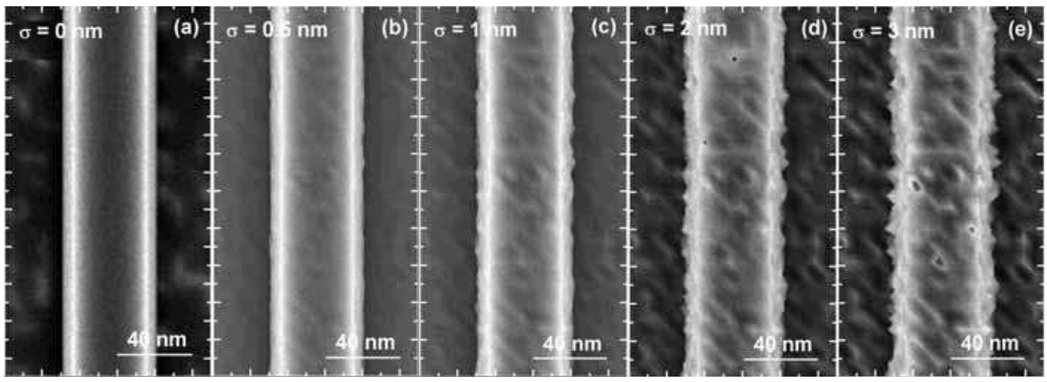

Fig. 24. The simulated CD-SEM images of the lines with different roughness amplitudes. The input parameters are: $H = 100$ nm, $W = 40$ nm, $\alpha = 3^{o}$ and $\alpha = 6$ nm. (a)-(e): the 3σ of roughness amplitude changes from 0 to 9 nm. The primary energy of the electron beam is 1 keV.

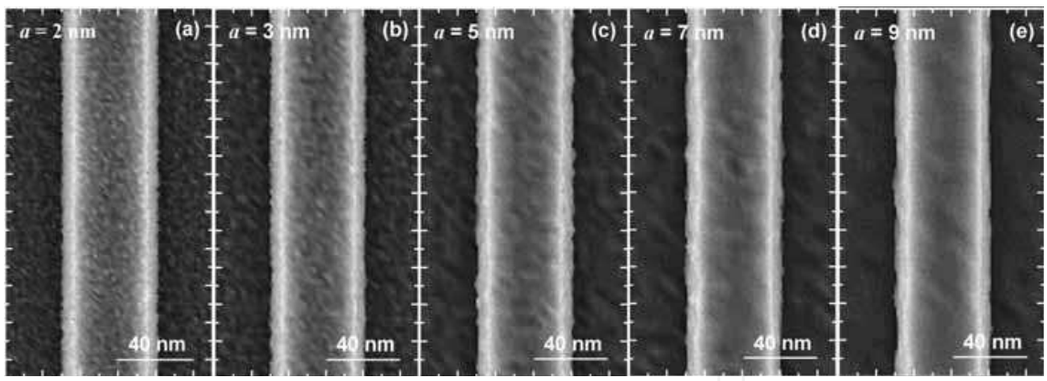

Fig. 25. The simulated CD-SEM images of the lines with different roughness densities. The input parameters are: $H = 100$ nm, $W = 40$ nm, $\alpha = 3^{o}$ and $3\sigma = 3$ nm. (a)-(e): the roughness interval changes from 2 to 9 nm. The primary energy of the electron beam is 1 keV.

The electrical charging phenomena play another major role in determination of CDs in CD-SEM for insulating specimens (such as, resist and SiO_2) studied in semiconductor industry. Charging effects can change SE yield, contrast or other properties by its influence on the electron transport process and the surface potential. It is a dynamic process in the imaging by SEM, which can cause a dynamic component of CD measurement error (Babin et al., 2008a; Babin et al., 2008b; Cazaux, 2006). A lot of theoretical works have pointed out the role of charging effects in SEM (Babin et al., 2008a; Babin et al., 2008b; Cazaux, 1999; Cazaux, 2004; Renoud et al., 2004; Rau et al., 2008) and it has been considered in several MC models (Babin et al., 2008a; Babin et al., 2008b; Frase et al., 2009). It is found that a contrast reversal when beam voltage was varied; thus the charging effect can further influence the accuracy of CDs. The quantitative study of the influence of charging effects on CDs is urgent for the future work.

There are also other factors that may influence the CDs, such as, electron beam incidence angle and focus, material properties, SE signal detection and others (noise and etc.) (Babin et al., 2008a). Indeed, these factors can be ignored in most cases. For example, normal incidence beam are most used in CD-SEM, the changes of incidence angle are just used in some special cases or intentionally (Morokuma et al., 2004; Tanaka et al., 2003). Also, material properties or SE signal detection would change the SE yields then the contrast of images accordingly. Noise in a real CD-SEM image could produce measurement errors that have both random and nonrandom components (Xiong et al., 2004). The sensitivity of a roughness measurement to noise depends on both the choice of edge detection algorithm and the quality of the focus. Villarrubia et al. (Villarrubia et al., 2005a) have pointed out that measurements are less sensitive to noise when a model-based algorithm is used. In fact, the effect of noise can be studied by adding appropriate random noise to the simulated line-scan or more simply by changing number of incident electrons for the simulation because the noise and the roughness are uncorrelated.

As discussed above, the beam size, geometry of feature related to the angle indexes (sidewall angle, footing and corner angles), roughness and charging effects are the dominating factors to the CDs. Therefore, the accurate algorithm should be constructed by considering these factors theoretically. Furthermore, the errors attributed to different factors should also be distinguished quantitatively for different influences may cause the similar

line-scan feature; for example, the sidewall angles and height may cause quite similar feature when appropriate parameters are selected as shown in Fig. 26. A MBL algorithm can be constructed but it needs great amount of calculation corresponding to all possible values of parameters. Because the relationship of CDs with different factors is smooth and monotonous, we may fit the line-scan curves to construct a library of the relation of CDs with different factors.

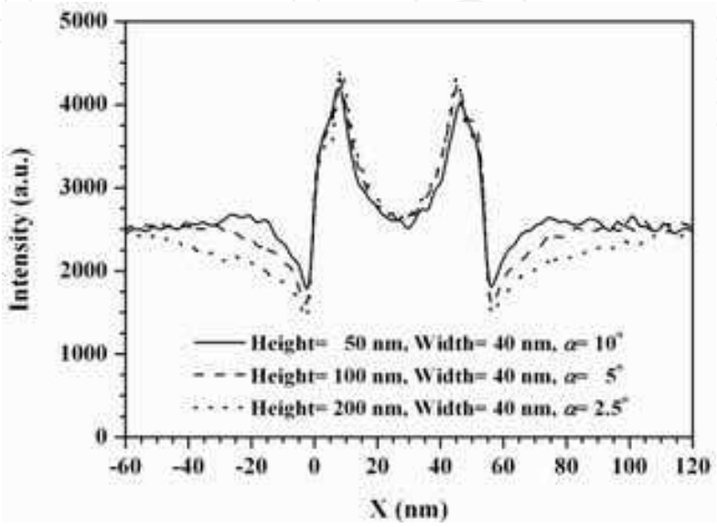

Fig. 26. A comparison of line-scans of lines with different side-wall angles and different heights. The primary energy of the electron beam is 1 keV, the beam size is 5 nm of FWHM.

4. Simulation study of scanning Auger electron images

As a useful surface analysis tool, SAM has been used for elemental mapping of material surface. But, the quantitative mapping is quite difficult because some artifact signals (Prutton et al., 1995) can be produced in a complex process of electron beam interaction with a sample in addition to its disadvantages in the low signal-to-noise ratio, low spatial resolution and low energy resolution.

To comprehend the problems, many efforts (Cowley & Liu, 1993; El Gomati et al., 1978; El Gomati et al., 1979; Hembree et al., 1991; Hembree & Venables, 1992; Ito et al., 1996; Janssen & Venables, 1978; Liu & Cowley, 1993; Liu et al., 1993; Tuppen & Davies, 1985) have been done theoretically by using a MC simulation method and experimentally since ten years ago. Experiments were aimed to improve the spatial resolution for surface step and small particles deposited on substrates under different beam conditions (Cowley & Liu, 1993; Hembree et al., 1991; Hembree & Venables, 1992; Ito et al., 1996; Janssen & Venables, 1978; Liu & Cowley, 1993; Liu et al., 1993). The edge effect observed on a rough edge, which is caused by primary electrons when passing through the side surface of a step/particle and then hitting the surrounding substrate surface to generate extra Auger signals of the substrate elements, and the backscattering effect, which is resulted by primary electrons that backscatter to the sample surface to generate extra AEs of the surface elements, are mainly discussed for systems of thin film step on substrates by simulations of Auger line scans using MC methods (El Gomati et al., 1978; El Gomati et al., 1979; Tuppen & Davies, 1985). Recently, attentions (Jablonski & Powell, 2005; Powell, 2004) have been paid to the effect of

backscattered electrons on the analysis area in SAM for improving the precision in quantitative analyses. It has been also reported (Wight & Powell, 2006) a use of the extended logistic function for fitting AE and SE line-scans in order to provide a measure of interface width. A quantitative description of surface roughness effects on Auger peak-line profiles for pure and alloyed specimens was done in an experimental way (Agterveld et al., 1999). However, the important mechanism of Auger signal contrast has not yet been discussed in detail. Furthermore, the interested specimens have been shifted from micrometer structure to nanometer structure (Childs et al., 1996) now with the instrumental improvement (Jacka, 2001; Prutton, 2000; Venables & Liu, 2005); it thus requires explanations for many effects appeared in the nano-systems.

In this respect the image simulation can help us to comprehend the contrast formation mechanism and, therefore, is expected to play an important role for predicating the artifact and improving precision of elemental mapping by SAM. For this purpose we employ in the present work a MC electron trajectory simulation method, which can accurately describe the scattering and transport processes of incident electrons and of signal electrons beneath the sample surface (Ding & Shimizu, 1996; Shimizu & ding, 1992). Our previous comparisons (Ding et al., 2001; Ding et al., 2004a; Ding et al., 2004b) made on the energy distribution and yields of BSEs and of SEs have resulted very well agreement between MC simulation results and experimental measurements and, thus, confirmed that this MC physical model of electron scattering is quite reasonable. Though MC simulation technique has been widely used in studies of SEM and X-ray microanalysis (Gauvin et al., 1995; Yan et al., 1998) for simple geometrical specimens or even more complex geometric structures (Liu, 2000; Ly et al., 1995; Postek et al., 2002) to obtain high quality point analysis, line-scans and two dimensional images, however, MC simulation of SAM images is still very limited partly due to the difficulty to model a multi-elemental system with complex geometric structures.

The topic in this section then aims to extend the MC simulation of SEM images for complex sample geometries (as in Sec. 3) to that of SAM images. The physical model of electron scattering and SE generation is mainly based on that of Ding & Shimizu (Ding & Shimizu, 1996), and here we need to consider additionally the AE generation process. The geometric structure model of specimen by Li & Ding (Ding & Li, 2005; Li & Ding, 2005), which combines the CSG modeling and a ray-tracing technique, is used to treat an inhomogeneous specimen with a complex geometric structure (as in Sec. 2); each basic object for structure constructing can be chemically vacancy, element, alloy or compound. The size of a sample considered can be very small, such as in the order of nm, which is comparable to or even less than the electron scattering mean free path. Hence, necessary correction to sampling of electron scattering step length due to the specimen boundary condition must be considered. These improvements make it a meaningful MC model for AE image simulation of complex structured specimen surface.

4.1 Simulation model

The present MC model of electron scattering is mainly based on our previous approach (Ding & Shimizu, 1996), i.e. with the uses of Mott's scattering cross-section (Mott, 1929) for electron elastic scattering and Penn's dielectric function approach (Penn, 1987) to electron inelastic scattering. The cascade secondary electron production is included. However, we also need to consider the ionization events for AE generation, for which the Casnati et al.'s cross-section (Casnati et al., 1982) for inner-shell ionization has been used. The main feature of this model is given in Sec. 2 and only the inner-shell ionization, the cascade SEs/AEs generation and the special boundary corrections are outlined below.

4.1.1 Inner-shell ionization

Several empirical expressions of inner-shell ionization cross-section are commonly used for MC simulation of individual ionization events; among them the Gryzinski's formula derived from a classical binary collision model (Grizinski, 1965a; Grizinski, 1965b; Grizinski, 1965c) had been more popularly used simply because of its simplicity in the expression and completeness for providing excitation function, total cross-section and stopping power equation that are necessary for a simulation based on continuous slowing down approximation. However, the Gryzinski's cross section does not satisfactorily describe the experimental data. By careful examining several frequently used cross-sections, it has been concluded (Powell, 1989; Seah & Gilmore, 1998) that the best formula of inner-most shells ionization cross-section is that of Casnati et al. (Casnati et al., 1982). Therefore, we adopt the following Casnati et al.'s cross-section in this work,

$$\sigma_U = \frac{a_0^2 F R^2 A B \ln U}{U E_U^2}. \tag{53}$$

This semi-empirical formula is the most suitable for describing the experiment data for $2 < U < 60$, where $U = E/E_U$ is the overvoltage ratio, R is the Rydberg energy and E_U is the binding energy of an inner-shell, A, B and F are the parameters related to E and E_U,

$$\begin{aligned} F &= \left(\frac{2+J}{2+T}\right)\left(\frac{1+T}{1+J}\right)^2 \times \left[\frac{(J+T)(2+T)(1+J)^2}{T(2+T)(1+J)^2 + J(2+J)}\right]^{3/2}; \quad A = \left(E_U/R\right)^d; \\ B &= 10.57 \exp\left[\left(-1.736/U\right) + \left(0.317/U^2\right)\right]; \quad J = E_U/m_e c^2; \\ d &= -0.0318 + \left(0.3160/U\right) - \left(0.1135/U^2\right); \quad T = E/m_e c^2 = UJ. \end{aligned} \tag{54}$$

Fig. 27. presents the M-shell ionization cross sections of Au by Gryzinski's and Casnati's formulas, respectively.

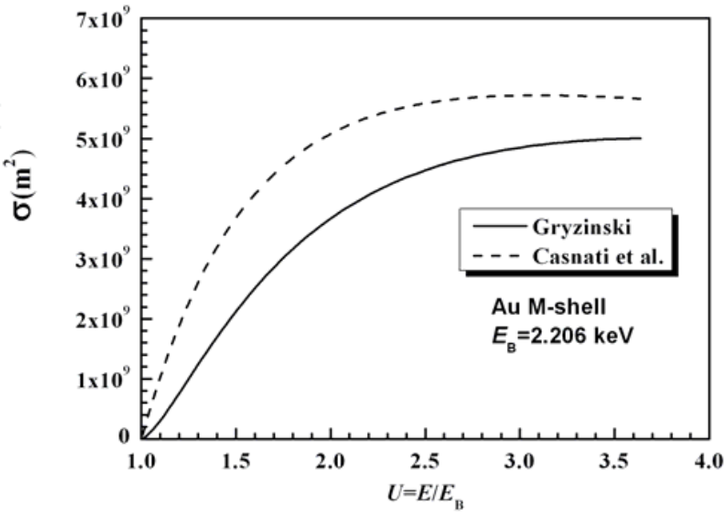

Fig. 27. The comparison of M-shell ionization cross sections of Au by Gryzinski's and Casnati's formula.

4.1.2 Cascade secondary electrons

In the present simulation model for discrete electron scattering events we have included SE generation because high energy SE may also slightly contribute to the inner-shell ionizations. Meanwhile the SE signals are essential to the simultaneous simulation of SEM image for comparison. We assume that each inelastic collision may produce a knock-on SE by transferring the loss energy ΔE, to an inner-shell electron or a valence-conduction electron. The generated SE may undergo the similar inelastic collisions to cause a cascade SE production inside the sample. The dielectric function model mentioned above has been introduced to describe the energy loss; this cascade process is traced in the simulation until all the SEs either escape from the surface or come to rest within the sample. Only those emitted SEs whose energy is less than 50 eV are counted as true SE signals, otherwise they are BSE signals. The detailed description of this simulation process has been discussed elsewhere (Ding & Shimizu, 1996; Li & Ding, 2005; Yue et al., 2005).

4.1.3 Auger electrons

Simulation of AE trajectories and the associated scattering events can be treated in the similar way as for the incident electrons and the generated SEs. The difference only takes place for the initial condition of a trajectory start.

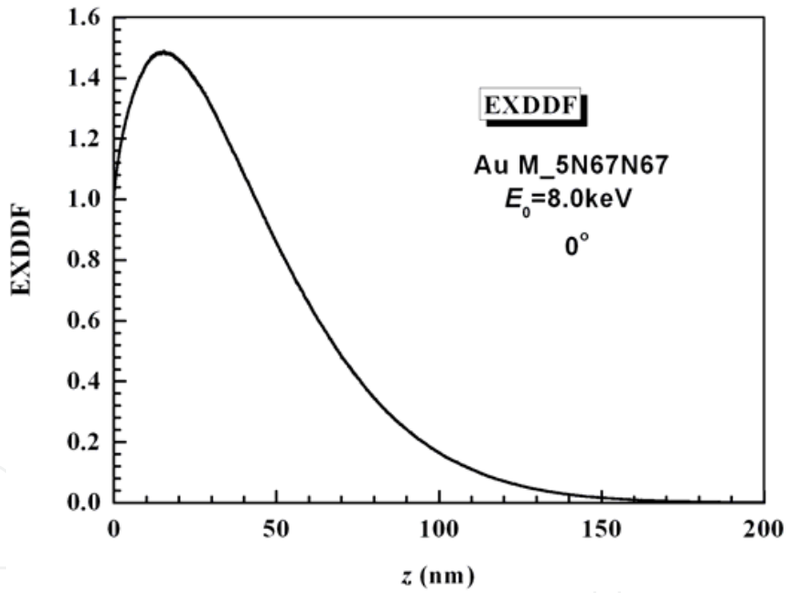

Fig. 28. The excitation depth distribution function (EXDDF) of $\mathrm{Au}(\mathrm{M_5N_{67}N_{67}})$ for 8 keV at normal incidence.

In a MC simulation once an inelastic collision occurs, that is sampled by a random number with the cross-section ratio between inelastic one to the total one, there is a certain probability to be the inner-shell ionization event. Another random number determines the type of inelastic scattering channel according to the cross-section ratio of the inner-shell ionization to the total inelastic cross-section obtained in the dielectric function approach. Casnati et al.'s cross-section is then used in this process for determining the ionization probability; however, the energy loss is still determined by the differential cross-section in

the dielectric function approach when the fate of the inelastic channel selection is determined as inner-shell ionization. Certainly, here we need to consider which element and/or which shell is responsible for the ionization with the related inner-shell ionization cross-sections.

The signal intensity of AEs is quite weak in comparing with that of BSEs and SEs because of its rare probability. However, for a SAM image simulation we need only concern with relative intensity of Auger signals. Then we adopt a weighting method to increase the effective Auger signal intensity: in an ionization event we enable a certain amount (taken as 50 here) of Auger electrons, instead of only one, to be generated with the same characteristic energy at the same place of ionization location but their isotropic emission direction is randomly sampled. The energies, coordinates and directions of movement of these generated AEs are stored in the memory of a computer. After tracking all the trajectories of the primary electrons, the simulation for AEs and SEs will then be performed. Only those AEs emitted from the sample surface into the vacuum without losing much their characteristic energy, i.e. $\Delta E < 1$ eV, will be registered as the concerned Auger signals. In Fig. 28, the excitation depth distribution function (EXDDF) of Au($M_5N_{67}N_{67}$) for 8 keV is given, which characterize the depth distribution of excited AE signals.

4.1.4 Boundary corrections

A general simulation of AE image has to deal with chemically inhomogeneous specimen. For such a specimen the electron scattering mean free path is position dependent because the total scattering cross-section varies with spatial region. Then the conventional sampling for the step length should be modified when an electron passes through an interface separating different material zones. Especially when the feature size of the structure considered is under the order of submicron and is comparable with the magnitude of scattering mean free path, the modification to the sampling of step length should be particularly important. A ray-tracing technique (Ding & Li, 2005; Li & Ding, 2005; Yue et al., 2005) in the calculation procedure of electron steps has been employed here, which is suitable for a sample made of discrete elemental zones. The sampling step is now described as in Sec. 2 in detail.

Because the electron kinetic energy inside a material is referenced to the inner potential, it changes with the inner potential when an electron passes through the boundary separating different materials, as illustrated in Sec. 2 (Kotera et al., 1992).

4.2 Results and discussion

MC simulations of line-scan profile and 2D image of AEs have been performed for several specimens. For calculation of a line-scan profile the trajectories of 10^5 primary electrons are simulated at each position of a line scanning across the specimen, and, for simulation of an image with 200×200 pixels the trajectories of 10^4 primary electrons are tracked at each pixel. To simplify the factors influencing the images simulation the beam diameter is firstly assumed to be infinitely small; a more realistic image for finite probe size can be further obtained by a convolution with a Gaussian electron beam profile. In the presented results we have not taken account of angular information of signal electrons, i.e. all the emitted electrons from the surface are taken as respective signals according to their kinetic energy. We also ignore any effect due to a detector and electric filed in vacuum chamber.

To verify the present MC simulation, the contrast investigation is firstly made by considering a particle/matrix system. Fig. 29(a) shows a quantitative comparison on the AE line-scans over Al particles on a Si substrate between the calculation and an experiment (Childs et al., 1996), and Fig. 29(b) shows a comparison for 2D SAM images of Al particles, treated as three semi-spheres of different diameters in calculation, placed on a Si substrate surface; the same condition as in the experiment (a 20 keV primary electron beam and the CMA analyzer) was considered in the calculation. By adjusting the parameters, i.e. particle diameter and beam diameter, in the simulation line-scan profile fit the experimental results very well with the estimated beam size of 20 nm. Furthermore, the contrast of the calculated Al(KLL)-AE image for a 20 nm beam spot size is also very close to that of the experimental image.

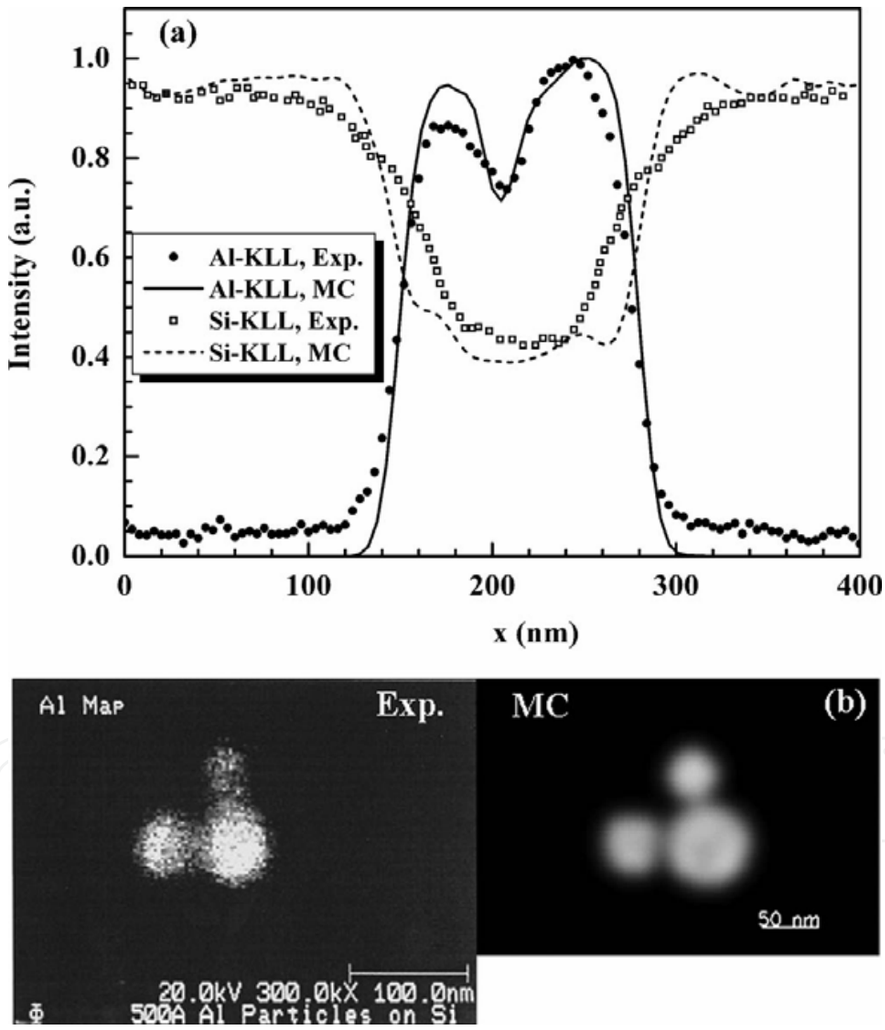

Fig. 29. Comparison on the Auger (a) line scans and (b) images of Al semi-spheres placed on a Si surface between the Monte Carlo simulation and an experiment (Childs et al., 1996). The primary electron beam of 20 keV is at normal incidence to the surface; the beam size is estimated to be 20 nm. The diameters of three semi-spheres are 56, 76 and 44 nm. The $\mathrm{Al(KLL)}$ - and $\mathrm{Si(KLL)}$ -Auger signals are measured with a CMA analyzer.

The simulations were then performed for different conditions by varying particle composition, size and location, the primary energy and the incident angle. For the contrast of such a system the topographic factor may also be a main source of contrast of an AE image. For quantitative surface chemical mapping, it is intended to reduce the artifacts by reducing topographical contrast and revealing otherwise hidden chemical contrast (Prutton et al., 1995). However, there are still no confirmed conclusions about the effect of each factor till now.

In Fig. 30 the calculated Auger line-scan profile is shown for an Au sphere located on or embedded in a Cu matrix. An obvious contrast change for both $\mathrm{Au}(\mathrm{M_5N_{67}N_{67}})$ and $\mathrm{Cu}(\mathrm{L_3M_{45}M_{45}})$ AE signals can be found when changing the depth of Au sphere as well as the sphere diameter. One can see that, for $\mathrm{Au}(\mathrm{M_5N_{67}N_{67}})$ Auger line-scans, the contrast due to topography retains obviously when a particle is placed on the surface or half embedded in the matrix. On the other hand, when an Au particle is entirely embedded in the matrix so that the topography factor is further weakened, the contrast varies quickly

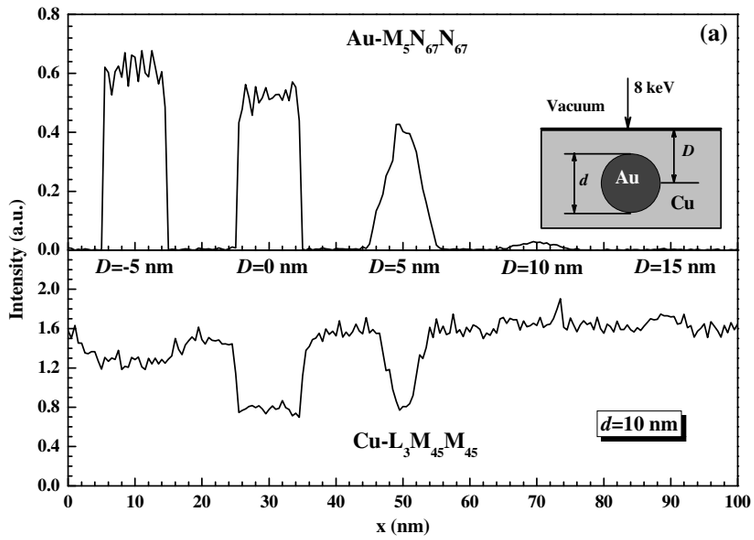

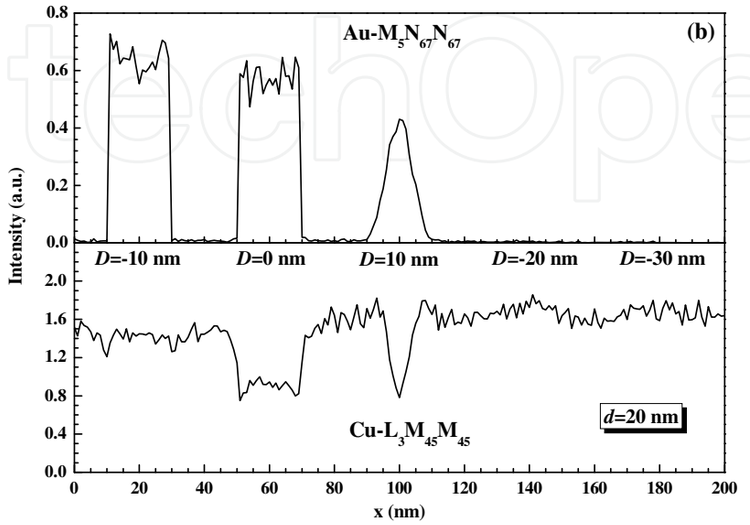

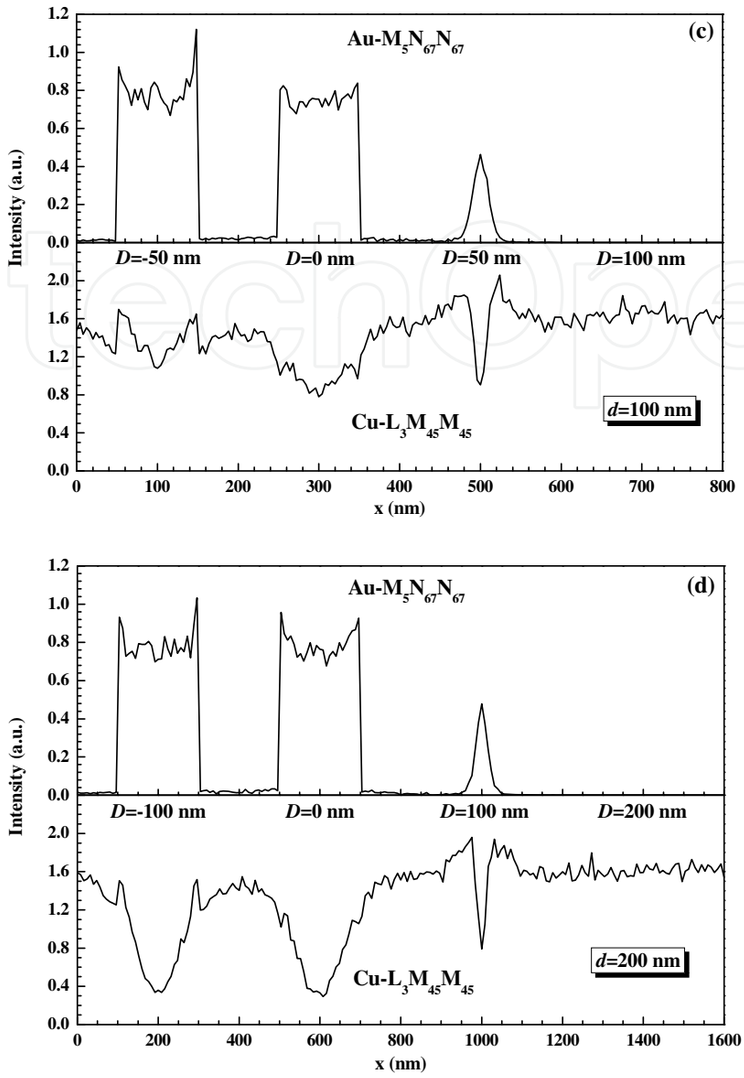

Fig. 30. Calculated $\mathrm{Au}(\mathrm{M_5N_{67}N_{67}})$- and $\mathrm{Cu}(\mathrm{L_3M_{45}M_{45}})$-Auger line-scans for an Au sphere located on a Cu surface or embedded in a Cu matrix. D is the depth of the particle (the negative value of D represents the case of a particle placed on the surface). d is the diameter of the particle: (a) 10 nm; (b) 20 nm; (c) 100 nm; (d) 200 nm. The primary electron beam of 8 keV is at normal incidence to the surface.

with the depth and wholly vanishes when the top of the particle reaches the signal effective depth, typically 0.3~3 nm. This is obviously due to the emission range limitation for AEs that excited by such a primary beam of 8 keV. Only those AEs generated from the outmost atomic layers of a solid surface can survive to be ejected and registered as AEs; this range estimated by IMFP depends on the AE energy only. The profile shape alters not only with the depth of a particle but also with the particle size. For large particles ($d = 200$ nm) there is an edge contrast quite similar to that observed in SEM. The reason for this sharp increase of Auger signals at an edge is that AEs generated can have greater chance of emission from the side surface when an electron beam impacting on the edge. Therefore, topographical factor plays also an important role in the SAM contrast of large features. For

$Cu(L_3M_{45}M_{45})$ Auger line-scans, the contrast is expected to be opposite to that of $Au(M_5N_{67}N_{67})$. This is almost true except in the case that a small particle (e.g. $d < 20$ nm at 8 keV) is placed on the surface (Fig. 30(a)): the dip of Cu-Auger electron current at the Au particle region is so weak that it is hard to observe the placed small Au particles from the variation of the substrate Auger signals. This is also a topographical effect for small features. For submicron Au particles (e.g. $d > 100$ nm at 8 keV), the usual edge enhancement effect (caused by higher-energy SEs that passing through the side surface of a particle and hitting the substrate to generated extra AE signals of the substrate (Ito et al., 1996)) and shadowing/shading effect (shadowing of the AEs on their emission path by a particle leads to a decrease of the substrate signals at the edge (Shimizu & Everhart, 1978)) become obvious in Cu-Auger line-scans as observed experimentally (Ito et al., 1996). These effects due to the excitation and emission process of AEs have been well expounded (El Gomati et al., 1988; Shimizu & Everhart, 1978; Tuppen & Davies, 1985; Umbach & Brunger, 1989; Wells, 1974).

To separate the topographical factor from the chemical factor in contrast a SAM image, Fig. 31 illustrates the contrast purely due to topographical factor for the case of Cu particles placed on a Cu substrate. The calculated contrast is then quite close to that of a secondary electron SEM image (Yue et al., 2005). This fact shows clearly that the topographical factor plays also an important role in SAM image contrast when the particle size is larger than the attention depth of AEs, leading to the edge effect. Rough surface, which could lead to more AE signal emission by enlarging the effective surface region, consequently, enhances the intensity of AE signals and produces the topographical contrast.

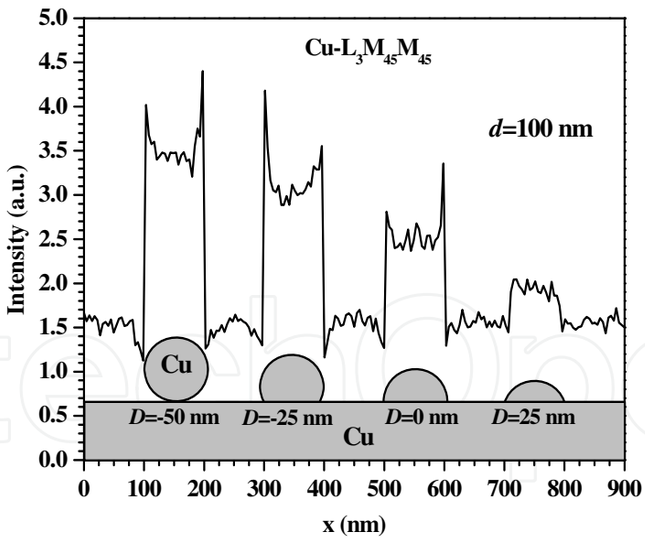

Fig. 31. Calculated $Cu(L_3M_{45}M_{45})$ -Auger line-scan for Cu spheres located on a Cu surface or embedded in a Cu matrix. The diameter of spheres is 100 nm and the separation between them is 200 nm. The primary electron beam of 8 keV is at normal incidence to the surface.

The chemical factor in SAM image contrast is mostly related to the dependence of excitation and emission processes of AEs on atomic number of materials. The contrast is basically caused by the Auger excitation probability of particular atoms within a small region of electron beam impact area; when the interaction volume of electron beam is larger than the

feature size of a structure the creation and transportation of AEs in a nearby spatial region which is chemically different could become an important factor to influence the contrast. Therefore, chemical and topographical factors are both dominant to the contrast.

The contrast properties presented above can be observed more intuitively by a 2D image. Fig. 32 shows the calculated results for Au particles of 100 and 200 nm diameters at different depths in a Cu matrix for a primary energy of 8 keV. $\mathrm{Au}(\mathrm{M_5N_{67}N_{67}})$ and $\mathrm{Cu}(\mathrm{L_3M_{45}M_{45}})$ AE images are both obtained. In Au-Auger electron images (Figs. 32(a) and (c)), the contrast obviously becomes weaker as the particle locates deeper inside the matrix, and, it even entirely vanishes when the depth reaches about the particle diameter. When the particle is located on the surface or half-embedded in the matrix, a very clear and similar contrast can be observed. In substrate Cu-Auger electron images (Figs. 32(b) and (d)), a corresponding contrast is observed. The edge enhancement effect and the shadowing/shading effect can also be clearly seen in the 2D image. It obviously shows that the contrast of Cu-Auger electron signals for a particle placed on the surface is higher than that half-embed in the matrix. This is due to the fact that the topography factor becomes more crucial so that the edge enhancement effect becomes more obviously when the particle placed on the surface.

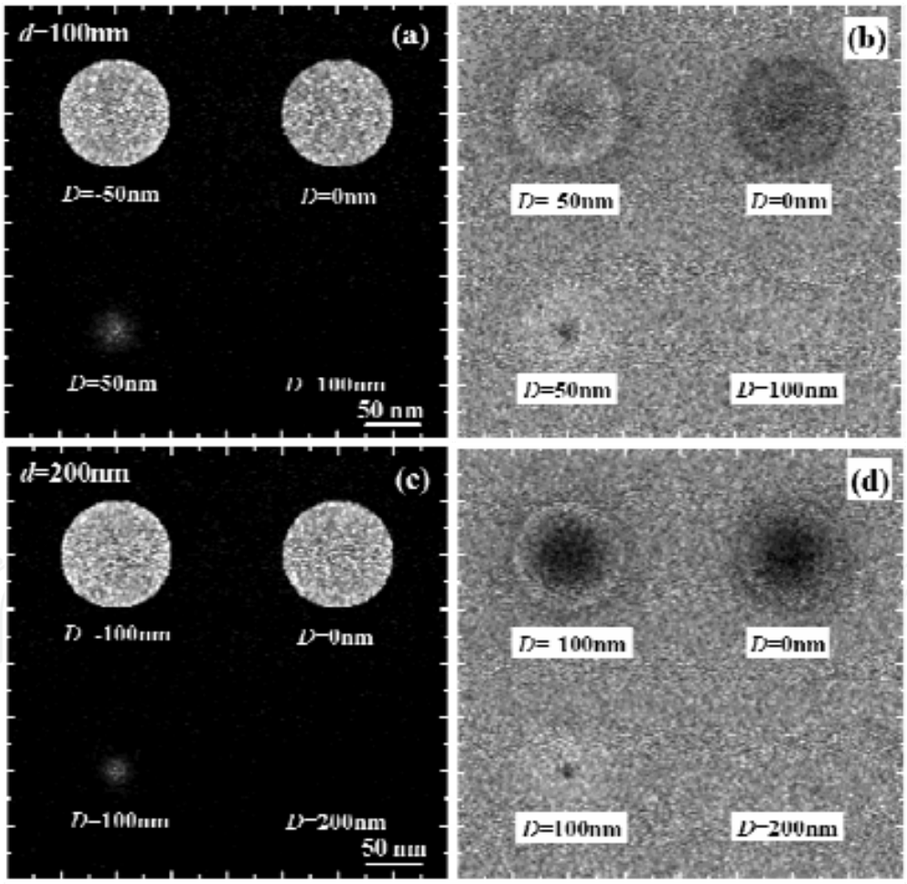

Fig. 32. Simulated SAM images for Au particles located at various depths in a Cu matrix: (a) $\mathrm{Au}(\mathrm{M_5N_{67}N_{67}})$, $d = 100$ nm; (b) $\mathrm{Cu}(\mathrm{L_3M_{45}M_{45}})$, $d = 100$ nm; (c) $\mathrm{Au}(\mathrm{M_5N_{67}N_{67}})$, $d = 200$ nm; (d) $\mathrm{Cu}(\mathrm{L_3M_{45}M_{45}})$, $d = 200$ nm. The primary electron beam of 8 keV is at normal incidence to the surface.

The contrast and the resolution of AE image are two main factors concerned by SAM. It has been shown that utilization of the low primary beam voltage of 3 kV has the advantage of reducing the edge effect in analyzing a 0.7 μm TiN particle on a steel (Forsyth & Bean, 1994; Olson et al., 1993) and an Au bar (0.6 μm high and 1.0 μm wide) on a Si substrate (Tuppen & Davies, 1985). While it has also been pointed out that (Ito et al., 1996) electrons with high energy will penetrate deep into the particle to reduce edge effect. The edge effect can dramatically degrade spatial resolution (El Gomati et al., 1988; Shimizu & Everhart, 1978; Tuppen & Davies, 1985) because AE from substrate can be detected even when the primary beam is impacted at the particle. At lower primary energies, it is more difficult for electrons to pass through the side surface of a particle and to hit the surrounding substrate surface for producing the edge effect. At higher primary energies, incident electrons can penetrate much deep into the particle to reduce the edge effect. Both of the extreme cases can improve the resolution of Auger images by reducing the edge effect.

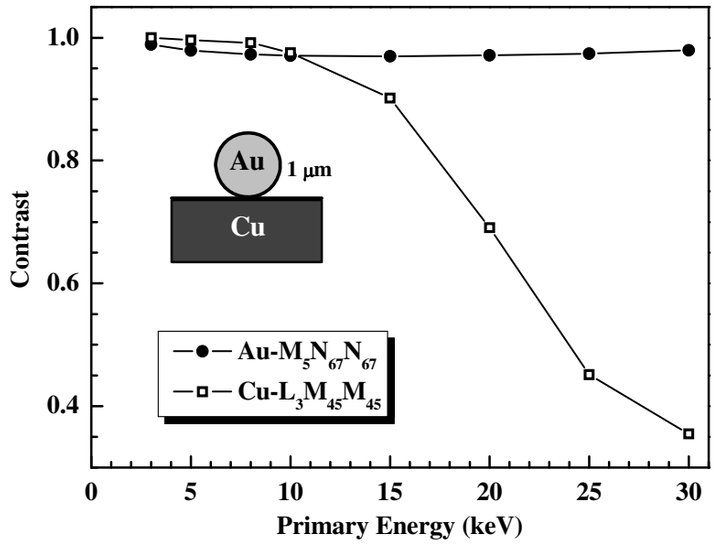

Fig. 33. Simulated $\mathrm{Au}(\mathrm{M_5N_{67}N_{67}})$ - and $\mathrm{Cu}(\mathrm{L_3M_{45}M_{45}})$ -Auger signal contrasts for an Au particle ($d = 1$ μm) placed on a Cu surface as a function of energy of a primary electron beam at normal incidence to the surface.

To investigate the accurate relationship between the contrast of AE image and primary electron energy, we have performed simulation of Auger line-scan of an Au sphere of the diameter of 1 μm placed on a Cu substrate surface at different primary energies and at a normal incidence condition (Fig. 33). The simulations of the line-scan profile have enabled the contrast to be estimated, which is defined as $C = (I_{\max} - I_{\min})/(I_{\max} + I_{\min})$, where I denotes the AE intensity. It can be seen that with the increase of the primary electron energy (3-30 keV), the Au-Auger electron contrast firstly decreases a little bit to a minimum at about 15 keV corresponding to overvoltage ratio of $U = 7 - 8$ and then increases. But the overall contrast in the energy range is nearly unit because the Au-Auger electrons can only be excited at the position of Au particle. However, the contrast for substrate Auger signals decreases consistently with increasing primary energy. This is due to the edge effect and backscattering effect that mentioned previously (El Gomati et al., 1988; Shimizu & Everhart, 1978; Tuppen & Davies, 1985). Both of these two effects can reduce the intensity difference

of the Cu-Auger electrons when a primary beam scans over a particle. The relations found here are useful to estimate the proper energy for the best contrast observation.

Fig. 34 shows the dependence of contrast on particle size. With increasing particle size the contrast of Au-$(M_5N_{67}N_{67})$ Auger image falls to be a constant but still nearly equals to unit, while the Cu-$(L_3M_{45}M_{45})$ contrast rises. This relation between contrast of Au signals and particle size can be easily understood from the mechanism of shading effect and the AE emission process. The contribution to the emitted Au-Auger signals by those electrons generated from deeper depth than IMFP can be neglected. Most of the emitted AEs are produced within a very short distance from the sample surface, typically 0.3~3 nm, which is enough small compared with the particle diameter concerned here. Therefore, the contrast of Au-Auger image does not change almost with particle size. For Cu-Auger electron image, the enhancement of the contrast with increase of particle size is mainly due to the reduction of substrate AE emission from the position underneath the particle. The topographical factor has dominated the Cu-Auger contrast: on the one hand, the edge effect is unconspicuous when the particle is very small (< 10 nm); on the other hand, for large particles (>400 nm) the contrast is a constant (~1 if the background signal is ignored) for the shading effect becomes obvious. In the middle range of the particle size (10~60 nm) where the contribution to the contrast by the edge effect exceeds that by the shading effect, a contrast reversion would appear. In the other words, for these particle sizes the detected intensity of substrate AEs when a primary beam is impacted at the center position of the particle can be even higher than that when a primary beam is impacted at the substrate surface. This effect is mainly due to that more substrate AEs can be exited by the edge effect, but less of these AEs emitted from the substrate would be shadowed by the particle.

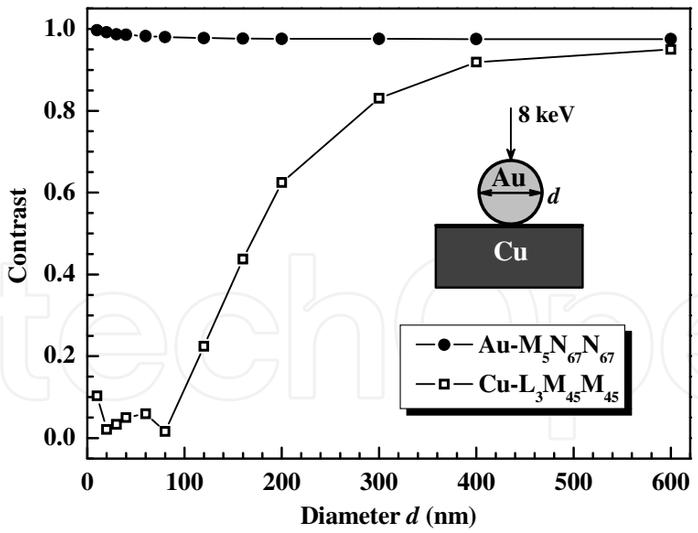

Fig. 34. Simulated Au$(M_5N_{67}N_{67})$- and Cu$(L_3M_{45}M_{45})$-Auger signal contrasts for an Au particle placed on a Cu surface as a function of particle size for a primary electron beam of 8 keV at normal incidence.

In order to investigate the contrast more comprehensively, we have also performed a calculation for the oblique incidence condition at an incident angle of 45°. The results for line-scans of an Au particle of diameter 100 nm located at different depths in a Cu matrix are

illustrated in Fig. 35. The following effects can be observed: Firstly, the Auger intensity peaks and valleys have a position shift. This is due to that the line-scan position does not correspond linearly to the true impact location at structures protruding from a plane surface when they are illuminated by an oblique electron beam. Secondly, the shapes of line-scan profiles are different for different depths because of an obstructing effect of Au particles. This difference in contrast may be helpful in judging the in-depth position of particles for such a system. Furthermore, the shading effect and the edge effect become more obvious in the forward side and the backward side, respectively. This is mainly because of that the oblique incidence condition can decrease the backscattering effect in the forward side facing electron beam but increase the effect in the backward side.

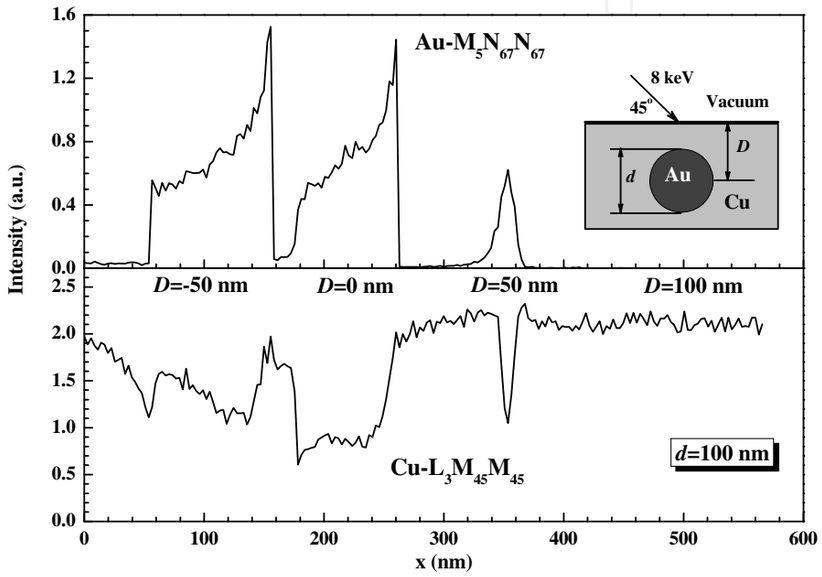

Fig. 35. Calculated $\mathrm{Au}(\mathrm{M_5N_{67}N_{67}})$ - and $\mathrm{Cu}(\mathrm{L_3M_{45}M_{45}})$ -Auger line scans for an Au particle ($d = 100$ nm) placed on a Cu surface and for a primary beam of 8 keV at an incident angle of 45°.

Besides the above effects, several other effects are studied for the systems under the special conditions. These effects are the contrast enhancement for different elemental particles that wholly embedded in a matrix, the artifact contrast due to nearby geometries containing different elements, and the variation of substrate AE intensity by the chemical composition of tiny particles. The mechanism for all of these effects can be explained by the electron transport and scattering processes under different special geometry configurations.

In Figs. 30 and 32, an enhancement of $\mathrm{Cu}(\mathrm{L_3M_{45}M_{45}})$ - AE signal in a line-scan or an image has been shown when an Au particle is wholly embedded in a Cu matrix. The effect is contrast to one's expectation and should be mainly due to the difference on the backscattering probability for the incident electrons between elements Au and Cu. If a nano-particle of heavier element is embedded in a matrix of lighter element, the intensity of the matrix Auger signals would increase because more BSEs from the embedded particle would transport to the nearby matrix region where they can excite more matrix AEs. This effect is useful for detection of particles underneath a surface by increasing the primary electron energy.

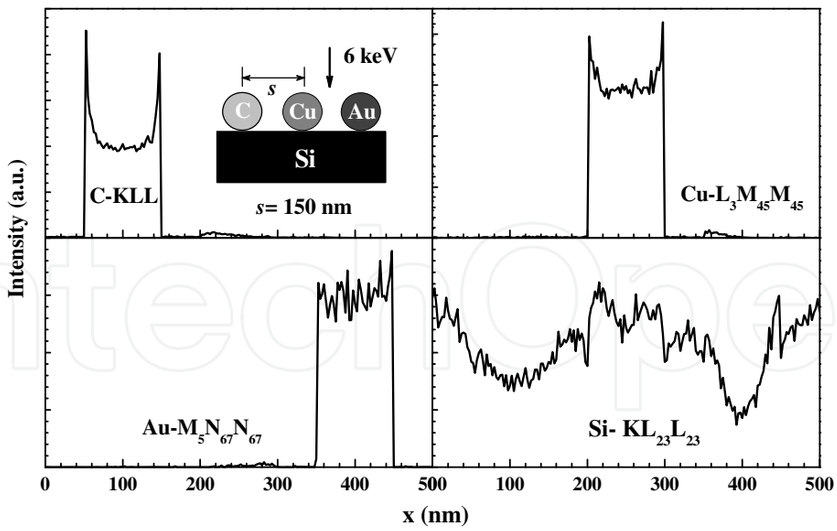

Fig. 36. Calculated line-scan of Auger electrons for a specimen made of C-, Cu- and Au-spheres placed on a Si surface and for a primary beam of 6 keV at normal incidence: (a) C(KLL); (b) Cu($L_3M_{45}M_{45}$); (c) Au($M_5N_{67}N_{67}$); (d) Si($KL_{23}L_{23}$) .The diameter of spheres is 100 nm and the separation between them is 150 nm.

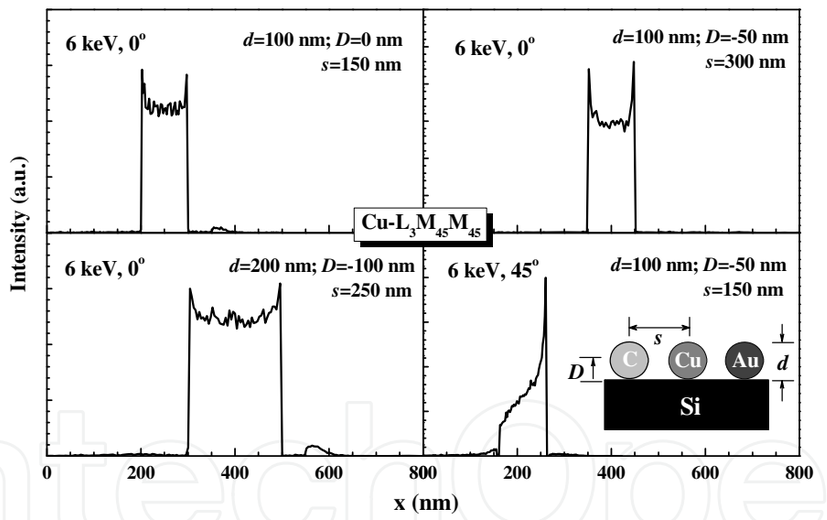

Fig. 37. Calculated Cu($L_3M_{45}M_{45}$)-Auger line-scans for a specimen made of C-, Cu- and Au-spheres placed on a Si surface or half-embedded in a Si matrix and for a primary beam of 6 keV. ***D*** is the depth of a particle (the negative value of ***D*** represents the case of a particle placed on the surface). ***d*** is the diameter of a particle and ***s*** is the separation between particles.

Fig. 36 illustrates line-scan profiles, for several different elemental particles closely placed on a surface of another elemental substrate, of corresponding elemental Auger signals. An important effect causing an artifact contrast of Auger images has been found, e.g. C(KLL) signals appear in the Cu-particle region and Cu($L_3M_{45}M_{45}$) signals in the Au-particle region. To explain the origin of artifact signal let us now, for example, consider Cu($L_3M_{45}M_{45}$) signals: when an electron beam scans over a heavy elemental Au-particle. Some of incident electrons can be emitted from Au-sphere after suffering multiple elastic scatterings to deflect

largely from their incident direction, and thus reentered into the nearby Cu particle; these scattered electrons can then have enough energy to produce Cu-Auger electrons inside the Cu particle, and those emitted Cu-Auger electrons are recorded as artifact signals at the scanning location of Au-particle. However, when an electron beam scans over a light elemental C-particle, less incident electrons can be scattered out of the particle with large scattering angle and, thus, produce negligible artifact signal at the scanning location of C-particle region. For substrate Si($KL_{23}L_{23}$) signal electrons, they are less produced in the region below Au-particle and many of them are hardly to be emitted from the region due to blocking of the particle. It can be seen that many factors may influence the artifact contrast, such as, the particle elements and respective Auger signal, the separation between particles, the particle size and depth, the incident energy and angle of incidence. Different conditions have thus been considered in simulation. Figs. 36(b) and 37(b) clearly show that the artifact contrast decreases dramatically when the separation between two particles change from 150 to 300 nm. Fig. 37(a) indicates that the artifact contrast still presents when the particle is half-embedded in the matrix. The artifact signal intensity increases with particle size in Fig. 37(c). For an oblique incidence, the artifact signal can be increased in the region of forward side but decreases in backward side, as shown in Fig. 37(d). Furthermore, it has been shown that the artifact C-Auger signals are more obvious at the position of Cu-particle but the artifact Cu-Auger signals are nearly vanished at the position of C-particle; the difference varies with the differences between atomic numbers of two relative elements of particles.

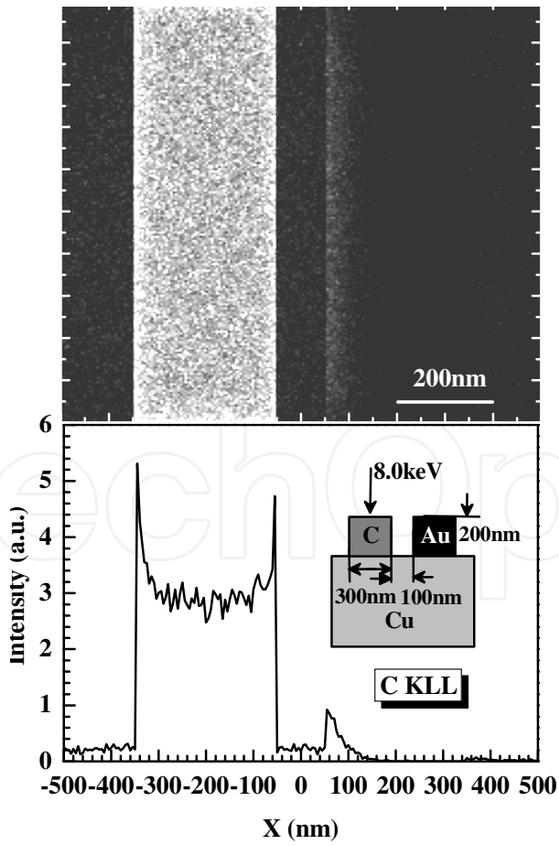

Fig. 38. Simulated C(KLL) -Auger line-scan and image for a specimen made of C- and Au-cuboids on a Si surface and for a primary beam of 8 keV at normal incidence.

Hence, as discussed above, the geometrical structure and elemental composition of specimen, the electron beam condition and Auger excitation shell are those factors to affect the artifact contrast of such a system. This artifact phenomenon is basically due to the backscattering of electrons. Obviously, it is much easier for electrons to escape from the sharp edges and to produce a stronger artifact contrast. Fig. 38 shows a simulated line-scan profile and a 2D image of C(KLL) signal for a system made of C- and Au-cuboids with small separation on a Si substrate. The result clearly shows that a sharp edge can strengthen the artifact contrast, especially for a nanometer structure.

In Fig. 36(d), another effect that the substrate Si-Auger electron intensity varies with the chemical composition of tiny particles has been predicted. The effect can be more obviously displayed in a 2D image as shown by Fig. 39. The contrast is due to many factors that may influence the transport property of signal electrons, such as, density, atomic number and thus stopping power and scattering cross-sections etc. Fig. 39 also shows the simulated SEM images of SEs and of BSEs in order to compare with the substrate SAM image. The signal intensity in a backscattered electron image increases only with atomic number through electron elastic scattering cross section while in a secondary electron image relates mainly to the stopping power of electron inelastic scattering. There is an additional difference between the substrate SAM- and SEM-signals: the substrate SAM signals are produced only inside the substrate and are blocked by the particles during their emission; therefore, the signal can only appear for small particles and it will vanish when the particle size is all greater than the attenuation length of substrate AEs, as shown by Fig. 40. Obviously, this calculation may help to understand the contrast formation mechanism of a SAM image of such nanometer structures.

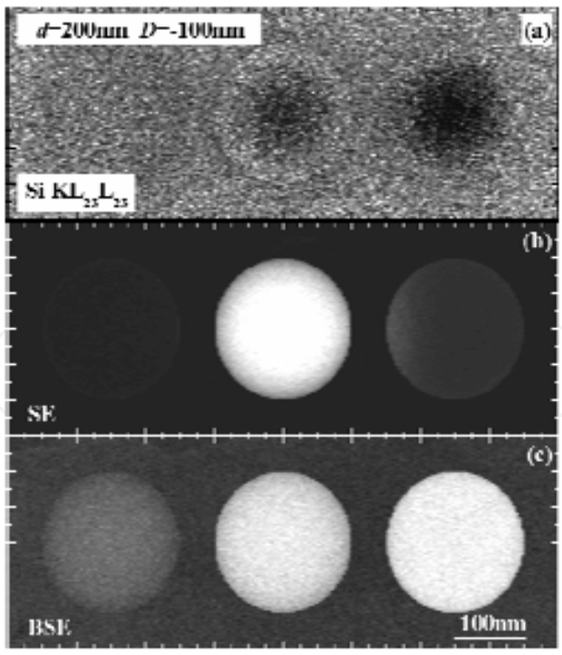

Fig. 39. Calculated SAM- and SEM-images for a specimen made of C-, Cu- and Au-spheres placed on a Si surface and for a primary beam of 6 keV at normal incidence. The diameter of the spheres is 200 nm and the separation between particles is 250 nm: (a) Si($KL_{23}L_{23}$) -Auger electrons; (b) secondary electrons; (c) backscattered electrons.

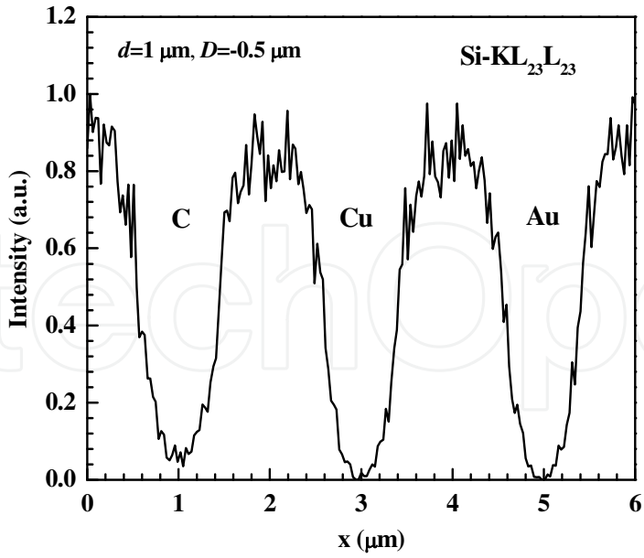

Fig. 40. Calculated line-scan of Si($KL_{23}L_{23}$)-Auger electrons for a specimen made of C-, Cu- and Au-spheres placed on a Si surface and for a primary beam of 6 keV at normal incidence. The diameter of the spheres is 1 μm and the separation between particles is 2 μm .

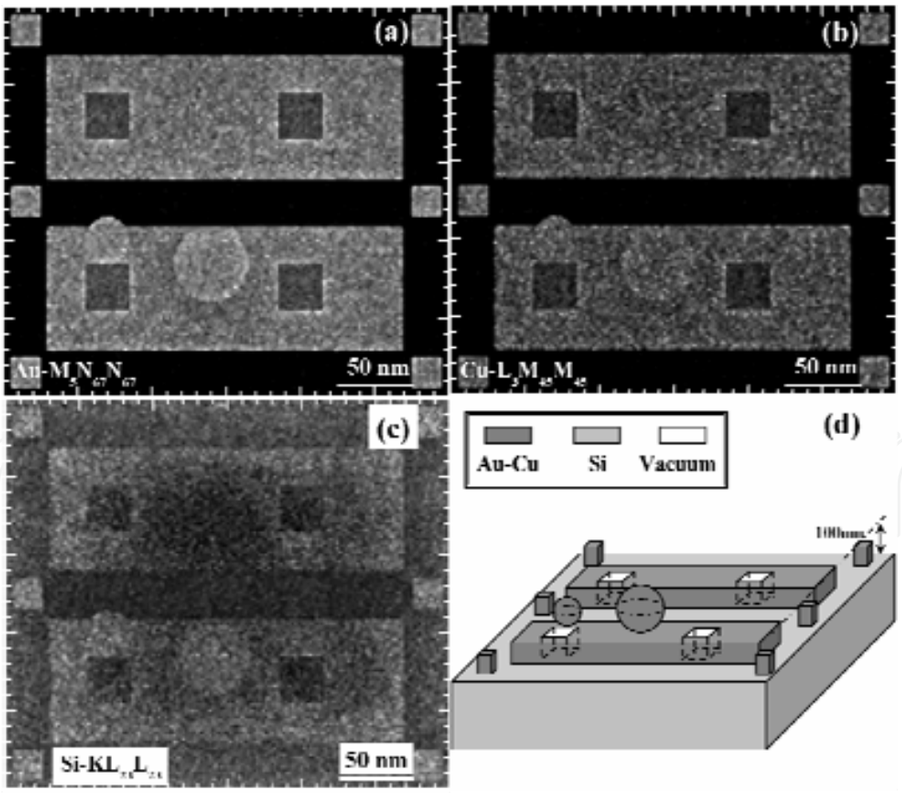

Fig. 41. Simulated Auger electron images for a complex structure of Au-Cu alloy ($Au_{0.8}Cu_{0.2}$) on a Si surface and for a primary beam of 6 keV at normal incidence: (a) Au($M_5N_{67}N_{67}$); (b) Cu($L_3M_{45}M_{45}$); (c) Si($KL_{23}L_{23}$); (d) sketch map.

In order to demonstrate the universality of the present simulation for complex structures with multi-elemental composition, the simulations of a multi-layer sample filled with Au-Cu alloy has also been performed; the calculated 2D SAM images are shown by Fig. 41. The Au- and Cu-Auger electron images illustrate the specified elemental distribution very well. More interesting is to find that the Si-Auger electron image has a brighter intensity at the position of the geometry features, which should mainly come from the obvious edge effect and backscattering effect for the nanometer system as mentioned above.

In summary, in this section we have proposed a MC simulation method of SAM images for a variety of inhomogeneous specimens made of elements, alloy or compounds with complex geometrical structure. Simulations for several model specimens have been carried out. A good agreement found between the simulation and experimental observation confirms the validity of the present simulation model. The contrast properties for several nanometer structures, typically the particles on a substrate, are discussed in detail by varying particle size and location, energy and incident angle of a primary beam. Several interesting results have been obtained: 1. The depth of particles can influence the contrast dramatically; topography and chemical composition are also the main factors affecting the contrast. 2. The relationships of the contrast of AE images with primary beam energy and particle size have been investigated. The contrast is mainly influenced by different effects, i.e., the edge effect and backscattering effect. 3. At oblique incidence condition the shape of structures observed in a SAM image may be distorted from the realistic one. 4. An enhancement of the substrate Auger signals is mainly due to the stronger backscattering effect of the embedded particle than that of the matrix. 5. The artifact contrast is shown and the backscattering effect of electrons is explained to be the main reason. 6. An effect has been predicted that the substrate Auger signal varies with chemical composition of small particles. 7. Simulation for a multi-layer sample filled with alloy has been performed to show the universality of the simulation method. These results have demonstrated that the present simulation model is universal and useful to explore the contrast mechanism of AE image. Further Monte Carlo studies are necessary in order to develop a correction procedure to remove artifact intensity for a quantitative SAM mapping of realistic surfaces.

5. Acknowledgement

This work was supported by the National Natural Science Foundation of China (Grant Nos. 11074232 and 10874160), “973” project (No. 2011CB932801) and “111” project.

6. References

Abe, H.; Hamaguchi, A. & Yamazaki, Y. (2007). Evaluation of CD-SEM measurement uncertainty using secondary electron simulation with charging effect. *Proc. SPIE*, 6518, 65180L-1-10

Agterveld, D.T.L. van; Palasantzas, G. & Hosson, J.Th.M. De (1999). Surface sensitivity effects with local probe scanning Auger–scanning electron microscopy. *Appl. Phys. Lett.*, 75, 1080-1082

Asenov, A.; Kaya, S. & Brown, A.R. (2003). Intrinsic parameter fluctuations in decananometer MOSFETs introduced by gate line edge roughness. *IEEE Trans. Elect. Dev.*, 50, 1254-1259

Ashley, J.C. (1988). Interaction of low-energy electrons with condensed matter: Stopping powers and inelastic mean free paths from optical data. *J Elect. Spectrosc. Rela. Phenom.*, 46, 199–214

Ashley, J.C. (1991). Energy loss probabilities for electron, positrons, and protons in condensed matter. *J Appl. Phys.*, 69, 674–678

Babin, S; Borisov, S; Miyano, Y; Abe, H; Kadowaki, M; Hamaguchi, A & Yamazaki, Y (2008a). Experiment and simulation of charging effects in SEM. *Proc. SPIE*, 6922, 692219-1-7

Babin, S; Borisov, S; Ivanchikov, A. & Ruzavin, I. (2008b). Calibration of CD-SEM: moving from relative to absolute measurements. *Proc. SPIE*, 6922, 69222M-1-8

Berger, M.J. (1963). Monte Carlo calculation of the penetration and diffusion of fast charged particles, in: *Methods in Computational Physics. vol. 1*, Alder, B.; Fernbach, S. & Rotenberg M. (Eds.), 135-215, Academic Press, New York

Bonham, R.A. & Strand, T.G. (1963). Analytical expression for potential of neutral Thomas-Fermi-Dirac atom and for the corresponding atomic scattering factors for x-rays and electrons. *J Chem. Phys.*, 39, 2200-2204

Brandt, W. & Reinheimer, J. (1970). Theory of semiconductor response to charged particles. *Phys. Rev. B*, 2, 3104–3112

Braun A.E. (2005). *Line Edge Roughness is Here to Stay* (Semiconductor International), Reed Elsevier, New York

Bronsgeest, M.S.; Barth, J.E.; Swanson, L.W. & Kruit, P. (2008). Probe current, probe size, and the practical brightness for probe forming systems. *J Vac. Sci. Technol. B*, 26, 949-955

Bunday, B.D.; Bishop, M.; McCormack, D.; Villarrubia, J.S.; Vladar, A.E.; Dixon, R.; Vorburger, T. & Orji, N.G. (2004). Determination of optimal parameters for CD-SEM measurement of line-edge roughness. *Proc. SPIE*, 5375, 515-533

Bunday, B. & Allgair, J. (2006). Small feature accuracy challenge for CD-SEM metrology physical model solution. *Proc. SPIE*, 6152, 61520S-1-16

Bunday, B.; Allgair, J.; Solecky, E.; Archie, C.; Orji, N.G.; Beach, J.; Adan, O.; Peltinov, R.; Bar-zvi, M. & Swyers, J. (2007). The coming of age of tilt CD-SEM. *Proc. SPIE*, 6518, 65181S-1-16

Bunyan P.J. & Schonfelder J.L. (1965). Polarization by mercury of 100 to 2000 eV electrons. *Proc. Phys. Soc.*, 85, 455-462

Cailler, M. & Ganachaud, J.P. (1990). Secondary electron emission from solids II. Theoretical description, In: *Fundamental Electron and Ion Beam Interactions with Solids for Microscopy, Microanalysis and Microlithography*, Schou, J.; Kruit, P. & Newbury, D.E. (Eds.), 81–110, Scanning Microscopy Supplement 4, Scanning Microscopy International, Chicago

Casnati, E.; Tatari, A. & Baraldi, C. (1982). An empirical approach to K-shell ionisation cross section by electrons. *J Phys. B: At. Mol. Phys.*, 15, 155-168

Cazaux, J. (1999). Some considerations on the secondary electron emission, δ, from e- irradiated insulators. *J Appl. Phys.*, 85, 1137-1147

Cazaux, J. (2004). Scenario for time evolution of insulator charging under various focused electron irradiations. *J Appl. Phys.*, 95, 731-742

Cazaux, J. (2005). Recent developments and new strategies in scanning electron microscopy. *J Microsc.*, 217, 16-35

Cazaux, J. (2006). e-Induced secondary electron emission yield of insulators and charging effects. *Nucl. Instru. Meth. Phys. Res. B*, 244, 307-322

Choi, Y.; Kim, S. & Han, O. (2006). The CD measuring repeatability enhancement by intensity gradient. *Proc. SPIE*, 6283, 62832F-1-8

Childs, K.D.; Narum, D.; LaVanier, L.A.; Lindley, P. M.; Schueler, B.W.; Mulholland, G. & Diebold, A.C. (1996). Comparison of submicron particle analysis by Auger electron spectroscopy, time-of-flight secondary ion mass spectrometry, and secondary electron microscopy with energy dispersive x-ray spectroscopy. *J Vac. Sci. Technol. A*, 14, 2392-2404

Chung, M.S. & Everhart, T.E. (1977). Role of plasmon decay in secondary electron emission in the nearly-free-electron metals. Application to aluminum. *Phys. Rev. B*, 15, 4699–4715

Cleary, J.G. & Wyvill, G. (1988). Analysis of an algorithm for fast ray tracing using uniform space subdivision. *The Visual Computer*, 4, 65-83

Cohen-Tannoudji, C.; Diu, B. & Laloe, F. (1977). *Quantum Mechanics*, Hermann, Paris

Cowley, J. M. & Liu, J. (1993). Contrast and resolution in REM, SEM and SAM. *Surf. Sci.*, 298, 456-467

Croon, J.A.; Storms, G.; Winkelmeier, S.; Pollentier, I.; Ercken, M.; Decoutere, S.; Sansen, W. & Maes, H.E. (2002). Line edge roughness: characterization, modeling and impact on device behavior, *Proceedings of IEDM Technical Digest*, pp. 307-310, Leuven Belgium

Dersch, U.; Korn, A.; Engelmann, C.; Frase, C.G.; Hαβler-Grohne, W.; Bosse, H.; Letzkus, F. & Butschke, J. (2005). Impact of EUV mask pattern profile shape on CD measured by CD-SEM. *Proc. SPIE*, 5752, 632-645

Desalvo, A.; Parisini, A. & Rosa, R. (1984). Monte Carlo simulation of elastic and inelastic scattering of electrons in thin films: I. Valence electron losses. *J Phys. D.*, 17, 2455–2471

Desalvo, A. & Rosa, R. (1987). Monte Carlo simulation of elastic and inelastic scattering of electrons in thin films: II. Core electron losses. *J Phys. D*, 20, 790–795

Diaz, C.H.; Tao, H.J.; Ku, Y.C.; Yen, A. & Young, K. (2001). An experimentally validated analytical model for gate line-edge roughness (LER) effects on technology scaling. *IEEE Elect. Dev. Lett.*, 22, 287-289

Ding, Z.J. & Shimizu, R. (1988a). Monte Carlo study of backscattering and secondary electron generation. *Surf. Sci.*, 197, 539–554

Ding, Z.J.; Shimizu, R.; Sekine, T. & Sakai, Y. (1988b). Theoretical and experimental studies of N(E) spectra in Auger electron spectroscopy. *Appl. Surf. Sci.*, 33/34, 99–106

Ding, Z.J. & Shimizu, R. (1989a). Theoretical study of the ultimate resolution of SEM. *J Microsc.*, 154, 193–207

Ding, Z.J. & Shimizu, R. (1989b). Inelastic collision of kV electrons in solids. *Surf. Sci.*, 222, 313–331

Ding, Z.J. (1990). *PhD Thesis*, Osaka University

Ding, Z.J. & Wu, Z.Q. (1993). A comparison of Monte Carlo simulation of electron scattering and x-ray production in solids. *J Phys. D*, 26, 507–516

Ding, Z.J.; Shimizu, R. & Goto, K. (1994). Background formation in the low energy region in Auger electron spectroscopy. *J Appl. Phys.*, 76, 1187–1195

Ding, Z.J. & Shimizu, R. (1996). A Monte Carlo modeling of electron interaction with solids including cascade secondary electron production. *Scanning*, 18, 92-113

Ding, Z.J.; Tang, X.D. & Shimizu, R. (2001). Monte Carlo study of secondary electron emission. *J Appl. Phys.*, 89, 718-726

Ding, Z.J. & Shimizu. R. (2003). Electron Backscattering and Channelling, In: *Surface Analysis by Auger and X-ray Photoelectron Spectroscopy*, Briggs, D. & Grant J.T. (Eds.), 587-618, IM Publications and SurfaceSpectra Limited, ISBN 1-901019-04-7, Manchester and Chichester

Ding, Z.J.; Li, H.M.; Tang, X.D. & Shimizu, R. (2004a). Monte Carlo simulation of absolute secondary electron yield of Cu. *Appl. Phys. A*, 78, 585-587

Ding, Z.J.; Li, H.M.; Goto, K.; Jiang, Y.Z. & Shimizu, R. (2004b). Energy spectra of backscattered electrons in Auger electron spectroscopy: Comparison of Monte Carlo simulation with experiment. *J Appl. Phys.*, 96, 4598-4606

Ding, Z.J. & Li, H.M. (2005). Application of Monte Carlo simulation to SEM image contrast of complex structures. *Surf. Interface Anal.*, 37, 912-918.

Ding, Z.J. & Wang, H.Y. unpublished.

Drouin, D.; Hovington, P. & Gauvin, R. (1997). CASINO: A new Monte Carlo code in C language for electron beam interactions—part II: Tabulated values of the Mott cross section. *Scanning*, 19, 20-28

Egerton, R.F. (1986). *Electron Energy Loss Spectroscopy in the Electron Microscope*, Plenum Press, New York

El Gomati, M.M. & Prutton, M. (1978). Monte Carlo calculations of the spatial resolution in a scanning auger electron microscope. *Surf. Sci.*, 72, 485-494

El Gomati, M.M.; Janssen, A.P.; Prutton, M. & Venables, J.A. (1979). The interpretation of the spatial resolution of the scanning Auger electron microscope: A theory/experiment comparison. *Surf. Sci.*, 85, 309-316

El Gomati, M.M.; Prutton, M.; Lamb, B. & Tuppen, C.G. (1988). Edge effects and image contrast in scanning Auger microscopy: A theory/experiment comparison. *Surf. Interface Anal.*, 11, 251-265

Ercken, M.; Storms, G.; Delvaux, C.; Vandenbroeck, N.; Leunissien, P. & Pollentier, I. (2002). Line Edge Roughness and Its Increasing Importance, *Proceedings ARCH Interface*

Fetter, A.L. & Walecka, J.D. (1971). *Quantum Theory of Many-Particle Systems*, McGraw-Hill, New York

Fink, M. & Yates, A.C. (1970). Theoretical electron scattering amplitudes and spin polarizations. Selected targets, electron energies 100 to 1500 eV. *Atomic Data*, 1, 385-456

Fink, M. & Ingram, J. (1972). Theoretical electron scattering amplitudes and spin polarizations. Electron energies 100 to 1500 eV. II. Be, N, O, Al, Cl, V, Co, Cu, As, Nb, Ag, Sn, Sb, I, and Ta targets. *Atomic Data*, 4, 129-207

Forsyth, N.M. & Bean, S. (1994). Low-energy field emission Auger electron spectroscopy. *Surf. Interface Anal.* 22, 338-341

Foucher, J.; Fabre, A.L. & Gautier, P. (2006). CD-AFM vs CD-SEM for resist LER and LWR measurements. *Proc. SPIE*, 6152, 61520V-1-8

Frase, C.G. & Hαβler-Grohne, W. (2005). Use of Monte Carlo models in the development and validation of CD operators. *Surf. Interface Anal.*, 37, 942-950

Frase, C.G.; Hαβler-Grohne, W..; Dai, G.; Bosse, H.; Novikov, Yu A. & Rakov, A.V. (2007a). SEM linewidth measurements of anisotropically etched silicon structures smaller than 0.1 μm. *Meas. Sci. Technol.*, 18, 439-447

Frase, C.G.; Buhr, E. & Dirscherl, K. (2007b). CD characterization of nanostructures in SEM metrology. *Meas. Sci. Technol.*, 18, 510-519

Frase, C.G.; Gnieser, D. & Bosse, H. (2009). Model-based SEM for dimensional metrology tasks in semiconductor and mask industry. *J Phys. D: Appl. Phys.*, 42, 183001

Ganachaud, J.P. & Cailler, M. (1979a). A Monte-Carlo calculation of the secondary electron emission of normal metals: I. The model. *Surf. Sci.*, 83, 498-518

Ganachaud, J.P. & Cailler, M. (1979b). A Monte-Carlo calculation of the secondary electron emission of normal metals: II. Results for aluminium. *Surf. Sci.*, 83, 519-530

Gauvin, R.; Hovington, P. & Drouin, D. (1995). Quantification of spherical inclusions in the scanning electron microscope using Monte Carlo simulations. *Scanning* 17, 202-219

Gregory, D. & Fink, M. (1974). Theoretical electron scattering amplitudes and spin polarizations. Electron energies 100 to 1500 eV. III. Li, Na, Mg, P, K, Ca, Sc, Mn, Ga, Br, Sr, Mo, Rh, Cd, Ba, W, and Os targets. *Atomic Data Nucl. Data Tables*, 14, 39-87

Gorelikov, D.V.; Remillard, J.; Sullioan, N.T. & Davidson, M. (2005). Model-based CD–SEM metrology at low and ultralow landing energies: implementation and results for advanced IC manufacturing. *Surf. Interface Anal.*, 37, 959-965

Grizinski, M. (1965a). Two-particle collisions. I. General relations for collisions in the laboratory system. *Phys. Rev.*, 138, A305-A321

Grizinski, M. (1965b). Two-particle collisions. II. Coulomb collisions in the laboratory system of coordinates. *Phys. Rev.*, 138, A322-A335

Grizinski, M. (1965c). Classical theory of atomic collisions. I. Theory of inelastic collisions. *Phys. Rev.*, 138, A336-A358

Gwyn, C.W. & Silverman, P.J. (2003). *Photomask Japan*, Yokohama, Japan

Hagemann, H.J.; Gudat, W. & Kunz, C. (1975). Optical constants from the far infrared to the x-ray region: Mg, Al, Cu, Ag, Au, Bi, C, and Al_2O_3. *J Opt. Soc. Am.*, 65, 742-744

Hamadeh, E.; Gunther, N.G.; Niemann, D. & Rahman, M. (2006). Gate line edge roughness amplitude and frequency variation effects on intra die MOS device characteristics. *Solid-State Elect.*, 50, 1156-1163

Hembree, G.G.; Drucker, J.S.; Luo, F.C.H.; Krishnamurthy, M. & Venables, J.A. (1991). Auger electron spectroscopy and microscopy with probe-size limited resolution. *Appl. Phys. Lett.*, 58, 1890-1892

Hembree, G.G. & Venables, J.A. (1992). Nanometer-resolution scanning Auger electron microscopy. *Ultramicros.*, 47, 109-120

Hovington, P.; Drouin, D. & Gauvin, R. (1997a). CASINO: A new Monte Carlo code in C language for electron beam interaction -part I: Description of the program. *Scanning*, 19, 1-14

Hovington, P.; Drouin, D.; Gauvin, R.; Joy, D.C. & Evans, N. (1997b). CASINO: A new Monte Carlo code in C language for electron beam interactions-part III: Stopping power at low energies. *Scanning*, 19, 29-35

Howell, P.G.T. (1996). A computer program to illustrate macro topography on electron backscattering. *Scanning*, 18, 428-432

Ichimura, S. (1980). *PhD Thesis*, Osaka University

Ichimura, S. and Shimizu, R. (1981). Backscattering correction for quantitative Auger analysis. *Sur.f Sci.*, 112, 386–408

International Technology Roadmap for Semiconductors (ITRS), Metrology 2007

Ito, H.; Ito, M.; Magatani, Y. & Soeda, F. (1996). Submicron particle analysis by the Auger microprobe (FE-SAM). *Appl. Surf. Sci.*, 100-101, 152-155

Jablonski, A. & Powell, C.J. (2005). Monte Carlo simulations of electron transport in solids: applications to electron backscattering from surfaces. *Appl. Surf. Sci.*, 242, 220-235

Jacka, M. (2001). Scanning Auger microscopy: Recent progress in data analysis and instrumentation. *J Elect. Spectros. Rela. Phenom.*, 114-116, 277-282

James, F. (1980). Monte Carlo theory and practice. *Rep. Prog. Phys.*, 43, 1145-1189

Janssen, A.P. & Venables, J.A. (1978). The effect of backscattered electrons on the resolution of scanning Auger microscopy. *Surf. Sci.*, 77, 351-364

Jensen, K.O. & Walker, A.B. (1993). Monte Carlo simulation of the transport of fast electrons and positrons in solids. *Surf. Sci.*, 292, 83-97

Jones, R.; Byers, J. & Conley, W. (2003). Top down versus cross sectional SEM metrology and its impact on lithography simulation calibration. *Proc. SPIE*, 5038, 663-673

Joy, D.C. (1985). Resolution in low voltage scanning electron microscopy. *J Microsc.*, 140, 283–292

Joy, D.C. (1987). A model for calculating secondary and backscattered electron yields. *J Microsc.*, 147, 51-64

Joy, D.C. (1995). A database on electron-solid interactions. *Scanning*, 17, 270-275

Joy, D.C. & Joy, C.S. (1996). Low voltage scanning electron microscopy. *Micron*, 27, 247-263

Joy, D.C.; Prasad, M.S. & Meyer, H. M. (2004). Experimental secondary electron spectra under SEM conditions. *J Microsc.*, 215, 77-85

Kalos, M.H. & Whitlock P.A. (1986). *Monte Carlo Methods. vol. 1*, Wiley, New York

Kawada, H.; Morokuwa, H.; Takami, S. & Nozoe, M. (2003). CD-SEM for 65-nm process node. *Hitachi Rev.*, 52, 140-146

Kaya, S.; Brown, A.R.; Asenov, A.; Magot, D. & Linton, T. (2001). Analysis of statistical fluctuations due to line edge roughness in sub-0.1 μm MOSFETs, *Proceedings of SISPAD*, pp. 78-81, Athens, Greece

Kim, S.D.; Wada, H. & Woo, J.C.S. (2004a). TCAD-based statistical analysis and modeling of gate line-edge roughness effect on nanoscale MOS transistor performance and scaling. *IEEE Trans. Semicond. Manuf.*, 17, 192-200

Kim, H.W.; Lee, J.Y.; Shin, J.; Woo, S.G.; Cho, H.K. & Moon, J.T. (2004b). Experimental investigation of the impact of LWR on sub-100-nm device performance. *IEEE Trans. Elect. Dev.*, 51, 1984-1987

Knuth, D.E. (1998). *The Art of Computer Programming, Vol. 3: Sorting and Searching*, Addison-Wesley, Boston, Massachusetts

Koshikawa, T. & Shimizu, R. (1973). Secondary electron and backscattering measurements for polycrystalline copper with a spherical retarding-field analyser. *J Phys. D.*, 6, 1369–1380

Kotera, M. (1989). A Monte Carlo simulation of primary and secondary electron trajectories in a specimen. *J Appl. Phys.*, 65, 3991–3998

Kotera, M.; Kishida, T. & Suga, H. (1990). Monte Carlo simulation of secondary electrons in solids and its application for scanning electron microscopy, In: *Fundamental Electron and Ion Beam Interactions with Solids for Microscopy, Microanalysis and Microlithography*, Schou, J.; Kruit, P. & Newbury, D.E. (Eds.), 111–126, Scanning Microscopy Supplement 4, Scanning Microscopy International, Chicago

Kotera, M.; Yamaguchi, S.; Fujiwara, T. & Suga, H. (1992). Theoretical evaluation of compositional contrast of scanning electron microscope images. *Jpn. J Appl. Phys.*, 31, 4531-4536

Li, H.M. & Ding, Z.J. (2005). Monte Carlo simulation of secondary electron and backscattered electron images in scanning electron microscopy for specimen with complex geometric structure. *Scanning*, 27, 254-267

Li, Y.G.; Mao, S.F., Xiao, S.M. & Ding, Z.J. (2008). Monte Carlo simulation study of SEM images of rough surfaces. *J Appl. Phys.*, 104, 064901

Li, Y.G.; Ding, Z.J. & Zhang, Z.M. (2009). Monte Carlo simulation study of scanning Auger electron images. *J Appl. Phys.*, 106, 024316

Li, Y.G. (2009). *PhD Thesis*, University of Science and Technology of China

Lindhard, J. (1954). On the properties of a gas of charged particles. *K. Dan. Vidensk. Selsk. Mat.-Fys. Medd.*, 28, No. 8, 1-57

Linton, T.; Giles, M. & Packan, P. (1999). The impact of line edge roughness on 100 nm device performance, *Proceedings of Silicon Nanoelectronics Workshop*, pp. 28-29, Tokyo, Japan

Linton, T.; Chandhok, M.; Rice, B.J. & Schrom, G. (2002). Determination of the line edge roughness specification for 34 nm devices, *Proceedings of IEDM Technical Digest*, pp. 303 – 306, Leuven Belgium

Liu, J. & Cowley, J.M. (1993). Scanning reflection electron microscopy and associated techniques for surface studies. *Ultramicros.*, 48, 381-416

Liu, J.; Hembree, G.G.; Spinnler, G.E. & Venables, J.A. (1993). Nanometer-resolution surface analysis with Auger electrons. *Ultramicros.*, 52, 369-376

Liu, J. (2000). Contrast of highly dispersed metal nanoparticles in high-resolution secondary electron and backscattered electron images of supported metal catalysts. *Microsc. Microanal.*, 6, 388-399

Lowney, J.R. (1995). Use of Monte Carlo modeling for interpreting scanning electron microscope linewidth measurements. *Scanning*, 17, 281-286

Lowney, J.R. (1996). Monte Carlo simulation of scanning electron microscope signals for lithographic metrology. *Scanning*, 18, 301-306

Luo, S.C.; Zhang, Y.S. & Wu, Z.Q. (1987). A Monte Carlo calculation of secondary electrons emitted from Au, Ag and Cu. *J Microsc.*, 148, 289–295

Luo, S.C. & Joy, D.C. (1990). Monte Carlo calculation of secondary electron emission, In: *Fundamental Electron and Ion Beam Interactions with Solids for Microscopy, Microanalysis and Microlithography*, Schou, J.; Kruit, P. & Newbury, D.E. (Eds.), 127–146, Scanning Microscopy Supplement 4, Scanning Microscopy International, Chicago

Ly, T.D.; Howitt, D.G.; Farrens, M.K. & Harker, A.B. (1995). Monte Carlo calculations for specimens with microstructures. *Scanning*, 17, 220-226

Maeda, T.; Tanaka, M.; Isawa, M.; Watanabe, K.; Hasegawa, N.; Sekiguchi, K.; Rooyackers, R.; Collaert, N. & Vandeweyer, T. (2008). MuGFET observation and CD measurement by using CD-SEM. *Proc. SPIE*, 6922, 69222P-1-9

Maksimov, E.G.; Mazin, I.I.; Rashkeev, S.N. & Uspenski, Y.A. (1988). First-principles calculations of the optical properties of metals. *J Phys. F.*, 18, 833–849

Mao, S.F.; Li, Y.G.; Zeng, R.G. & Ding, Z.J. (2008). Electron inelastic scattering and secondary electron emission calculated without the single-pole approximation. *J Appl. Phys.*, 104, 114907

Matsukawa, T. & Shimizu, R. (1974). A new type of edge effect in high resolution scanning electron microscopy. *Jpn. J Appl. Phys.*, 13, 583–586

Matsumoto, J.; Ogiso, Y.; Sekine, M.; Iwai, T. & Whittey, J. (2006). A new algorithm for SEM critical dimension measurements for differentiating between lines and spaces in dense line/space patterns without tone dependence. *Proc. SPIE*, 6349, 634941-1-6

Mayol, R. & Salvat, F. (1997). Total and transport cross sections for elastic scattering of electrons by atoms. *Atomic Data Nucl. Data Tables*, 65, 55-154

Metropolis, N. (1987). The beginning of the Monte Carlo method. *Los Alamos Science Special Issue*, 125-130

Moller, C. (1931). über den Stoss zweier Teilchen unter Berücksichtigung der Retardation der Kräfte. *Z. Phys.*, 70, 786–795

Morokuma, H.; Miyamoto, A.; Tanaka, M.; Kazui, M. & Takane, A. (2004). New technique to reconstruct effective 3D profile from tilt images of CD-SEM. *Proc. SPIE*, 5375, 727-734

Mott, N.F. (1929). The scattering of fast electrons by atomic nuclei. *Proc. Roy. Soc. London A*, 124, 425-442

Mott, N.F. & Massey, H.S.W. (1965). *The Theory of Atomic Collisions*, Oxford University Press, Oxford, UK

Murata, K.; Kyser, D.F. & Ting, C.H. (1981). Monte Carlo simulation of fast secondary electron production in electron beam resists. *J Appl. Phys.*, 52, 4396–4405

Murata, K.; Kawata, H. & Nagami, K. (1987). Electron scattering in low voltage scanning electron microscope targets, In: *Physical Aspects of Microscopic Characterization of Materials*, Kirschner, J.; Murata, K. & Venables, J.A. (Eds.), 83–91, Scanning Microscopy Supplement 1, Scanning Microscopy International, Chicago

Newbury, D.E.; Myklebust, R.L. & Steel, E.B. (1990). Monte Carlo electron trajectory simulation of x-ray emission from films supported on substrates, In: *Microbeam Analysis–1990*. Michael, J.R. and Ingram, P. (Eds.), 127–130, San Fransico Press, San Fransico

Nizzoli, F. (1978). A model calculation of the dielectric function in trigonal Se and Te with local-field corrections included. *J Phys. C.*, 11, 673–683

Novikov, Yu.A.; Ozerin, Yu.V.; Rakov, A.V. & Todua, P.A. (2007). Method for linear measurements in the nanometre range. *Meas. Sci. Technol.*, 18, 367-374

Oldiges, P.; Lin, Q.; Petrillo, K.; Sanchez, M.; Ieong, M. & Hargrove, M. (2000). Modeling line edge roughness effect in sub 100 nm gate length devices, *Proceedings of SISPAD*, pp. 131-134, Seattle, WA, USA

Olson, R.R.; Vanier, L.A. & Narum, D.H. (1993). Backscattering limitations to spatial resolution in the Auger microprobe. *Appl. Surf. Sci.*, 70-71, 266-272

Palik, E.D. (Ed.) (1985). *Handbook of Optical Constants of Solids*, Academic Press, New York

Palik, E.D. (Ed.) (1991). *Handbook of Optical Constants of Solids II*, Academic Press, New York

Penn, D.R. (1987). Electron mean-free-path calculations using a model dielectric function. *Phys. Rev. B*, 35, 482–486

Pines, D. (1964). *Elementary Excitations in Solids*, Benjamin, New York

Postek, M.T.; Vladar, A.E.; Lowney, J.R. & Keery, W.J. (2002). Two-dimensional simulation and modeling in scanning electron microscope imaging and metrology research. *Scanning*, 24, 179-185

Powell, C.J. (1985). Calculation of electron mean free paths from experimental optical data. *Surf. Interface Anal.*, 7, 263–274

Powell, C.J. (1989). Cross sections for inelastic electron scattering in solids. *Ultramicros.*, 28, 24-31

Powell, C.J. (2004). Effect of backscattered electrons on the analysis area in scanning Auger microscopy. *Appl. Surf. Sci.*, 230, 327-333

Prutton, M.; Barkshire, I.R. & Crone, M (1995). Quantitative surface chemical mapping with Auger and backscattered electron signals. *Ultramicros.*, 59, 47-62

Prutton, M. (2000). From LEED to MULSAM. *Surf. Interface Anal.*, 29, 561-571

Radzimski, Z.J. & Russ, J.C. (1995). Image simulation using Monte Carlo methods: Electron beam and detector characteristics. *Scanning*, 17, 276-280

Rao-Sahib T.S. & Wittry D.B. (1974). X-ray continuum from thick elemental targets for 10-50 keV electrons. *J Appl. Phys.*, 45, 5060-5068

Rather, H. (1980). *Excitation of Plasmon and Interband Transitions by Electrons*, Springer-Verlag, New York

Rau, E.I.; Fakhfakh, S.; Andrianov, M.V.; Evstafeva, E.N.; Jbara, O.; Rondot, S. & Mouze, D. (2008). Second crossover energy of insulating materials using stationary electron beam under normal incidence. *Nucl. Instru. Meth. Phys. Res. B*, 266, 719-729

Reimer, L. & Krefting, E.R. (1976). The effect of scattering models on the results of Monte Carlo simulations, In: *Use of Monte Carlo in Electron Probe Microanalysis and Scanning Electron Microscopy*, Heinrich, K.F.J.; Newbury, D.E. & Yakowitz, H. (Eds.), 45–60, NBS Special Publication 460, US Government Printing Office, Washington, D.C.

Reimer, L. (1998). *Scanning Electron Microscopy-Physics of Image Formation and Microanalysis, Volume 45 of Spring Series in Optical Sciences, 2nd edition*. Springer, Berlin

Renoud, R.; Mady, F. Attard, C.; Bigarre, J. & Ganachaud, J.P. (2004). Secondary electron emission of an insulating target induced by a well-focused electron beam -Monte Carlo simulation study. *Phys. Stat. Sol. (a)*, 201, 2119-2133

Rice, B.J.; Cao, H.; Grumski, M. & Roberts, J. (2006). The limits of CD metrology. *Microele. Eng.*, 83, 1023-1029

Ritchie, R.H.; Garber, F.W.; Nakai, M.Y. & Birkhoff, R.D. (1969). Low energy electron mean free paths in solids, In: *Advances in Radiation Biology*, *Vol. 3*, Augenstein, L.G.; Mason, R. & Zelle, M. (Eds.), 1–28, Academic Press, New York

Rubinstein, R.Y. (1981). *Simulation and the Monte Carlo Method,* Wiley, New York

Salvat, F.; Fernández-Varea, J. M. & Sempau, J. (2006). PENELOPE-2006: A Code System for Monte Carlo Simulation of Electron and Photon Transport, *Workshop Proceedings*, Barcelona, Spain

Seah, M.P. & Gilmore, I.S. (1998). Quantitative AES VII. The ionization cross-section in AES. *Surf. Interface Anal.*, 26, 815-824

Seeger, A.; Fretzagias, C. & Taylo, R. (2003). Software acceleration techniques for the simulation of scanning electron microscope images. *Scanning*, 25, 264-273

Shiles, E.; Sasaki, T.; Inokuti, M. & Smith, D.Y. (1980). Self-consistency and sum-rule tests in the Kramers-Kronig analysis of optical data: Applications to aluminum. *Phys. Rev. B*, 22, 1612-1628

Shimizu, R. & Everhart, T.E. (1978). Edge effect in high−resolution scanning Auger−electron microscopy. *Appl. Phys. Lett.*, 33, 549-551

Shimizu, R. & Ichimura, S. (1981). *Quantitative Analysis by Auger Electron Spectroscopy*, Toyota Foundation Research Rep., Tokyo, Japan

Shimizu, R. & Ding, Z.J. (1992). Monte Carlo modeling of electron-solid interactions. *Rep. Prog. Phys.*, 55, 487-531

Shishido, C.; Takagi, Y.; Tanaka, M.; Komuro, O.; Morokuma, H. & Sasada, K. (2002). Characterizing cross-sectional profile variations by using multiple parameters extracted from top-down SEM images. *Proc. SPIE*, 4689, 653-660

Singhal, S.P. (1975). Dielectric matrix for aluminum. *Phys. Rev. B*, 12, 564–574

Sramek, S.J. & Cohen, M.L. (1972). Frequency- and wave-vector-dependent dielectric function for Ge, GaAs, and ZnSe. *Phys. Rev. B*, 6, 3800–3804

Streitwolf, H.W. (1959). Zur Theorie der Sekundärelektronenemission von Metallen der Anregungsprozess. *Ann. Phys. R.*, 3, 183–196

Sturm, K. (1982). Electron energy loss in simple metals and semiconductors. *Adv. Phys.*, 31, 1–64

Tanaka, M.; Shishido, C.; Takagi, Y.; Morokuma, H.; Komuro, O. & Mori, H. (2003). Cross-sectional gate feature identification using top-down SEM images. *Proc. SPIE*, 5038, 624-635

Tanaka, M.; Shishido, C.; Takagi, Y. & Morokuma, H. (2004). MPPC technique for gate etch process monitoring using CD-SEM images and its validity verification. *Proc. SPIE*, 5375, 1144-1155

Tanaka, M.; Villarubia, J.S. & Vladar, E. (2005). Influence of focus variation on linewidth measurements. *Proc. SPIE*, 5752, 144-155

Tanaka, M.; Shishido, C. & Kawada, H. (2006). Influence of electron incident angle distribution on CD-SEM linewidth measurements. *Proc. SPIE*, 6152, 61523Z-1-11

Tanaka, M.; Shishido, C.; Nagatomo, W. & Watanabe, K. (2007). CD-bias evaluation and reduction in CD-SEM linewidth measurements. *Proc. SPIE*, 6518, 651848-1-10

Tanaka, M.; Shishido, C.; Nagatomo, W. & Watanabe, K. (2008a). Application of model-based library approach to Si_3N_4 hardmask measurements. *Proc. SPIE*, 6922, 69222L-1-11

Tanaka, M.; Meessen, J.; Shishido, C. & Watanabe, K. (2008b). CD bias reduction in CD-SEM linewidth measurements for advanced lithography. *Proc. SPIE*, 6922, 69221T-1-11

Tanuma, S.; Powell, C.J. & Pen, D.R. (1988). Calculation of electron IMFPs for 31 materials. *Surf. Interface Anal.*, 11, 577-589

Tanuma, S.; Powell, C.J. & Pen, D.R. (2005). Calculations of stopping powers of 100 eV to 30 keV electrons in 10 elemental solids. *Surf. Interface Anal.*, 37, 978-988

Tokesi, K.; Nemethy, A.; Kover, L.; Varga, D. & Mukoyama, T. (1996). Modeling of electron scattering in thin manganese films on silicon by Monte Carlo methods. *J Appl. Phys.*, 79, 3763-3769

Tuppen, C.G. & Davies, G.J. (1985). High spatial resolution Auger linescans across heterogeneous chemical edges by Monte Carlo calculation. *Surf. Interface Anal.*, 7, 235-240

Umbach, A. & Brünger, W.H. (1989). Spatial resolution tests of scanning Auger microscopy under different topographical conditions. *Surf. Interface Anal.*, 14, 401-413

Venables, J.A. & Liu, J. (2005). High spatial resolution studies of surfaces and small particles using electron beam techniques. *J Elect. Spectros. Rela. Phenom.*, 143, 205-218

Villarrubia, J.S.; Vladar, A.E.; Bunday, B.D. & Bishop, M. (2004). Dimensional metrology of resist lines using a SEM model-based library approach. *Proc. SPIE*, 5375, 199-209

Villarrubia, J.S.; Vladar, A.E. & Postek, M.T. (2005a). Simulation study of repeatability and bias in the critical dimension scanning electron microscope. *J Microlithogr. Microfabr. Microsyst.*, 4, 033002

Villarrubia, J.S.; Vladar, A.E. & Postek, M.T. (2005b). Scanning electron microscope dimensional metrology using a model-based library. *Surf. Interface Anal.*, 37, 951-958

Villarrubia, J.S. & Ding, Z.J. (2009). Sensitivity of model-based SEM dimensional measurements to model assumptions. *Proc. SPIE*, 7272, 72720R-1-15.; *J Micro/Nanolith. MEMS MOEMS*, 8, 033003

Vogel, E.M. (2007). Technology and metrology of new electronic materials and devices. *Nature Nanotech.*, 2, 25-32

Walker, D.W. (1971). Relativistic effects in low energy electron scattering from atoms. *Adv. Phys.*, 20, 257-323

Walter, J.P. & Cohen, M.L. (1972). Frequency- and wave-vector-dependent dielectric function for silicon. *Phys Rev B*, 5, 3101–3110

Wang, H.Y. (2006). *Bachelor Thesis*, University of Science and Technology of China

Wang, Z.G.; Khuen, S.K.; Fukaya, R.; Kadowaki, Y.; Arai, N.; Ezumi, M. & Satoh, H. (2007). Long-term critical dimension measurement performance for a new mask CD-SEM, S-9380M. *Proc. SPIE*, 6730, 67304T-1-9

Wells, O. (1974) *Scanning Electron Microscopy*, McGraw-Hill, New York

Wight, S.A. & Powell, C.J. (2006). Evaluation of the shapes of Auger- and secondary-electron line scans across interfaces with the logistic function. *J Vac. Sci. Technol. A*, 24, 1024-1210

Xiong, S. & Bokor, J. (2002). Study of gate line edge roughness effects in 50 nm bulk MOSFET devices. *Proc. SPIE*, 4689, 733-741

Xiong, S. & Bokor, J. (2004). A simulation study of gate line edge roughness effects on doping profiles of shortchannel MOSFET devices. *IEEE Trans. Elect. Dev.*, 51, 228-232

Xiong, S.; Bokor, J.; Xiang, Q.; Dudley, I.; Rao, P. & Wang, H.H. (2004). Is gate line edge roughness a first-order issue in affecting the performance of eddp sub-micro bulk MOSFET devices?. *IEEE Trans. Semicond. Manuf.*, 17, 357-361

Yamaguchi, A.; Tsuchiya, R.; Fukuda, H.; Komuro, O.; Kawada, H. & Iizumi, T. (2003). Characterization of line-edge roughness in resist patterns and estimations of its effect on device performance. *Proc. SPIE*, 5038, 689-698

Yamaguchi, A.; Ichinose, K.; Shimamoto, S.; Fukuda, H.; Tsuchiya, R.; Ohnishi, K.; Kawada, H. & Iizumi, T. (2004). Metrology of LER: influence of line-edge roughness (LER) on transistor performance. *Proc. SPIE*, 5375, 468-476

Yamane, T. & Hirano, T. (2005). Sidewall effect of photomask by scanning electron microscope and optical critical dimension metrology. *J Microlithogr. Microfabr. Microsyst.*, 4, 033003

Yamazaki, Y. (1977). *PhD Thesis*, Osaka University

Yan, H.; El Gomati, M.M.; Prutton, M.; Wilkinson, D.K.; Chu, D.P. & Dowsett, M.G. (1998). Mc3D: A three-dimensional Monte Carlo system simulating image contrast in surface analytical scanning electron microscopy I - Object-oriented software design and tests. *Scanning*, 20, 465-484

Yoshimura, T.; Shiraishi, H.; Yamamoto, J. & Okazaki, S. (1993). Correlation of nano edge roughness in resist patterns with base polymers. *Jpn. J Appl. Phys*, 32, 6065-6070

Yue, Y.T.; Li, H.M. & Ding, Z.J. (2005). Monte Carlo simulation of secondary electron and backscattered electron images for a nanoparticle-matrix system. *J Phys. D: Appl. Phys.*, 38, 1966-1977

Applications of Monte Carlo Method in Science and Engineering
Edited by Prof. Shaul Mordechai

ISBN 978-953-307-691-1
Hard cover, 950 pages
Publisher InTech
Published online 28, February, 2011
Published in print edition February, 2011

In this book, Applications of Monte Carlo Method in Science and Engineering, we further expose the broad range of applications of Monte Carlo simulation in the fields of Quantum Physics, Statistical Physics, Reliability, Medical Physics, Polycrystalline Materials, Ising Model, Chemistry, Agriculture, Food Processing, X-ray Imaging, Electron Dynamics in Doped Semiconductors, Metallurgy, Remote Sensing and much more diverse topics. The book chapters included in this volume clearly reflect the current scientific importance of Monte Carlo techniques in various fields of research.

INTECH
open science | open minds

InTech Europe
University Campus STeP Ri
Slavka Krautzeka 83/A
51000 Rijeka, Croatia
Phone: +385 (51) 770 447
Fax: +385 (51) 686 166
www.intechopen.com

InTech China
Unit 405, Office Block, Hotel Equatorial Shanghai
No.65, Yan An Road (West), Shanghai, 200040, China
中国上海市延安西路65号上海国际贵都大饭店办公楼405单元
Phone: +86-21-62489820
Fax: +86-21-62489821

IntechOpen